

UNIVERSITY OF  
COPENHAGEN



A PHYSICIST'S APPROACH TO MACHINE LEARNING  
Understanding The Basic Bricks

CHRISTIAN MICHELSSEN  
Master's Thesis (Cand. Scient.)  
January 3<sup>rd</sup>, 2020

Supervised by  
Troels Petersen



UNIVERSITY OF COPENHAGEN

Copyright © 2019  
Christian Michelsen

[HTTPS://GITHUB.COM/CHRISTIANMICHelsen](https://github.com/CHRISTIANMICHelsen)

This thesis was inspired by the works of Edward R. Tufte using the Tufte-L<sup>A</sup>T<sub>E</sub>X package.

*First printing, December 2019*

## *Abstract*

Here will be a decent abstract at some point<sup>TM</sup>.



# *Contents*

<i>Abstract</i>	iii
<i>Table of Contents</i>	v
<i>Foreword</i>	ix
1 <i>Introduction</i>	1
<i>Part I</i>	3
2 <i>Machine Learning Theory</i>	5
2.1 <i>Statistical Learning Theory</i> . . . . .	5
2.2 <i>Supervised Learning</i> . . . . .	6
2.3 <i>Generalization Bound</i> . . . . .	7
2.3.1 <i>Generalization Bound for infinite hypotheses</i> . . . . .	9
2.4 <i>Avoiding overfitting</i> . . . . .	10
2.4.1 <i>Model Regularization</i> . . . . .	10
2.4.2 <i>Cross Validation</i> . . . . .	12
2.4.3 <i>Early Stopping</i> . . . . .	13
2.5 <i>Loss functions</i> . . . . .	14
2.5.1 <i>Evaluation Function</i> . . . . .	16
2.6 <i>Decision Trees</i> . . . . .	16
2.6.1 <i>Ensembles of Decision Trees</i> . . . . .	17
2.7 <i>Hyperparameter Optimization</i> . . . . .	19
2.7.1 <i>Grid Search</i> . . . . .	20
2.7.2 <i>Random Search</i> . . . . .	20
2.7.3 <i>Bayesian Optimization</i> . . . . .	21
2.8 <i>Feature Importance</i> . . . . .	22

3	<i>Danish Housing Prices</i>	27
	3.1 <i>Data Preparation and Exploratory Data Analysis</i> . . . . .	28
	3.1.1 <i>Correlations</i> . . . . .	30
	3.1.2 <i>Validity of input variables</i> . . . . .	31
	3.1.3 <i>Cuts</i> . . . . .	33
	3.2 <i>Feature Augmentation</i> . . . . .	33
	3.2.1 <i>Time-Dependent Price Index</i> . . . . .	34
	3.3 <i>Evaluation Function</i> . . . . .	35
	3.4 <i>Initial Hyperparameter Optimization</i> . . . . .	36
	3.5 <i>Hyperparameter Optimization</i> . . . . .	38
	3.6 <i>Results</i> . . . . .	40
	3.7 <i>Model Inspection</i> . . . . .	43
	3.8 <i>Multiple Models</i> . . . . .	45
	3.9 <i>Discussion</i> . . . . .	47
	<i>Part II</i>	51
4	<i>Particle Physics and LEP</i>	53
	4.1 <i>The Standard Model</i> . . . . .	53
	4.2 <i>Quark Hadronization</i> . . . . .	54
	4.3 <i>The ALEPH Detector and LEP</i> . . . . .	56
	4.4 <i>Jet clustering</i> . . . . .	58
	4.5 <i>The variables</i> . . . . .	58
5	<i>Quark Gluon Analysis</i>	63
	5.1 <i>Data Preprocessing</i> . . . . .	63
	5.2 <i>Exploratory Data Analysis</i> . . . . .	64
	5.2.1 <i>Dimensionality Reduction</i> . . . . .	66
	5.2.2 <i>Correlations</i> . . . . .	67
	5.3 <i>Loss and Evaluation Function</i> . . . . .	67
	5.4 <i>b</i> -Tagging Analysis . . . . .	68
	5.4.1 <i>b</i> -Tagging Hyperparameter Optimization . . . . .	68
	5.4.2 <i>b</i> -Tagging Results . . . . .	70
	5.4.3 <i>b</i> -Tagging Model Inspection . . . . .	71
	5.5 <i>b</i> -Tagging Efficiency . . . . .	72
	5.6 <i>g</i> -Tagging Analysis . . . . .	74
	5.6.1 <i>Permutation Invariance</i> . . . . .	75
	5.6.2 <i>Truncated Uniform PDF</i> . . . . .	75
	5.6.3 <i>g</i> -Tagging Hyperparameter Optimization . . . . .	76

5.6.4	<i>PermNet</i>	77
5.6.5	<i>1D Comparison of LGB and PermNet</i>	78
5.6.6	<i>g-Tagging Results</i>	78
5.7	<i>g-Tagging Efficiency</i>	81
5.8	<i>Generalized Angularities in 3-jet events</i>	82
5.9	<i>Gluon splitting</i>	84
5.9.1	<i>Variables</i>	84
5.9.2	<i>Efficiencies</i>	86
5.9.3	<i>Closure Test</i>	87
5.9.4	<i>4-jet results</i>	89
5.10	<i>Quark-Gluon Discussion</i>	90
<i>Part III</i>		93
6	<i>Discussion and Outlook</i>	93
7	<i>Conclusion</i>	95
7.1	<i>Tufte-LATEX Website</i>	95
7.2	<i>Tufte-LATEX Mailing Lists</i>	95
7.3	<i>Getting Help</i>	95
A	<i>Housing Prices Appendix</i>	97
B	<i>Quarks vs. Gluons Appendix</i>	125
<i>List of Figures</i>		156
<i>List of Tables</i>		158
<i>Bibliography</i>		159





## *Part I*

Part I of this thesis covers the introductory theory of machine learning in [chapter 2](#) along with some extra technical aspects of it. In [chapter 3](#) machine learning is applied to estimate Danish housing prices as precisely and accurately as possible.



## *Part II*

Part II of this thesis deals with particle physics and the discriminatory power of machine learning for quark-gluon identification and subsequent analysis. In [chapter 4](#) the theory of the Standard Model is introduced together with a description of the ALEPH detector. This is applied in [chapter 5](#) where the types of jets and events in each collision is analysed using machine learning to improve the understanding of how gluon jets look and behave.



# 4. Particle Physics and LEP

*“Not only is the Universe stranger than we think, it is stranger than we can think.”*

---

— Werner Heisenberg

The aim of this chapter is to introduce the reader to the level of particle physics required for understanding the following chapter, in particular introducing the Standard Model in section 4.1, the theory behind quark hadronization in section 4.2, and the ALEPH detector at LEP in section 4.3. The goal is not to make a deep and thorough introduction to the field as this is not needed for the following analysis along with the fact that the author is no particle physicist himself.

## 4.1 The Standard Model

The Standard Model (SM) [50, 82, 100] of particle physics is the currently best known description of the elementary particles and thus describes the fundamental building blocks of our Universe. An overview of the particles explained by the Standard Model is shown in the typical tabular form seen in Figure 4.1. In general, particles comes in two categories: *bosons* and *fermions*.

The fermions, the left part of the figure, are particles with half-integer spin that obey Fermi-Dirac statistics and are further subdivided into *quarks* (upper left in figure) and *leptons* (lower left). The quarks interact with all of the four known forces<sup>1</sup>, including the strong force. In contrary the leptons do not interact with the strong force. Quarks are never observed freely but are always combined into *hadrons* due to *color confinement* which is further explained in section 4.2. An example of this are protons which consists of two up-quarks and a down-quark. Leptons exist as either the charged leptons<sup>2</sup> or as neutral leptons, the so-called neutrinos<sup>3</sup>. The fermions come in three generations with increasing mass.

The bosons, the right part of the figure, are the force-carrying particles (with integer spin and which obey Bose-Einstein statistics) where the gluon  $g$  mediates the strong nuclear force (color charge), the photon  $\gamma$  mediates the electromagnetic force (charge), and the two  $W^\pm$  and the Z bosons the weak nuclear force (weak isospin). The Higgs boson  $H$ , experimentally discovered in 2012 [39, 40], does not mediate any forces but interacts with all massive particles and explains why particles have mass.

<sup>1</sup> Gravity, electromagnetism, and the strong and weak force.

<sup>2</sup> The electron  $e$ , the muon  $\mu$ , and the tau  $\tau$ .

<sup>3</sup> The electron neutrino  $\nu_e$ , the muon neutrino  $\nu_\mu$ , and the tau neutrino  $\nu_\tau$ .

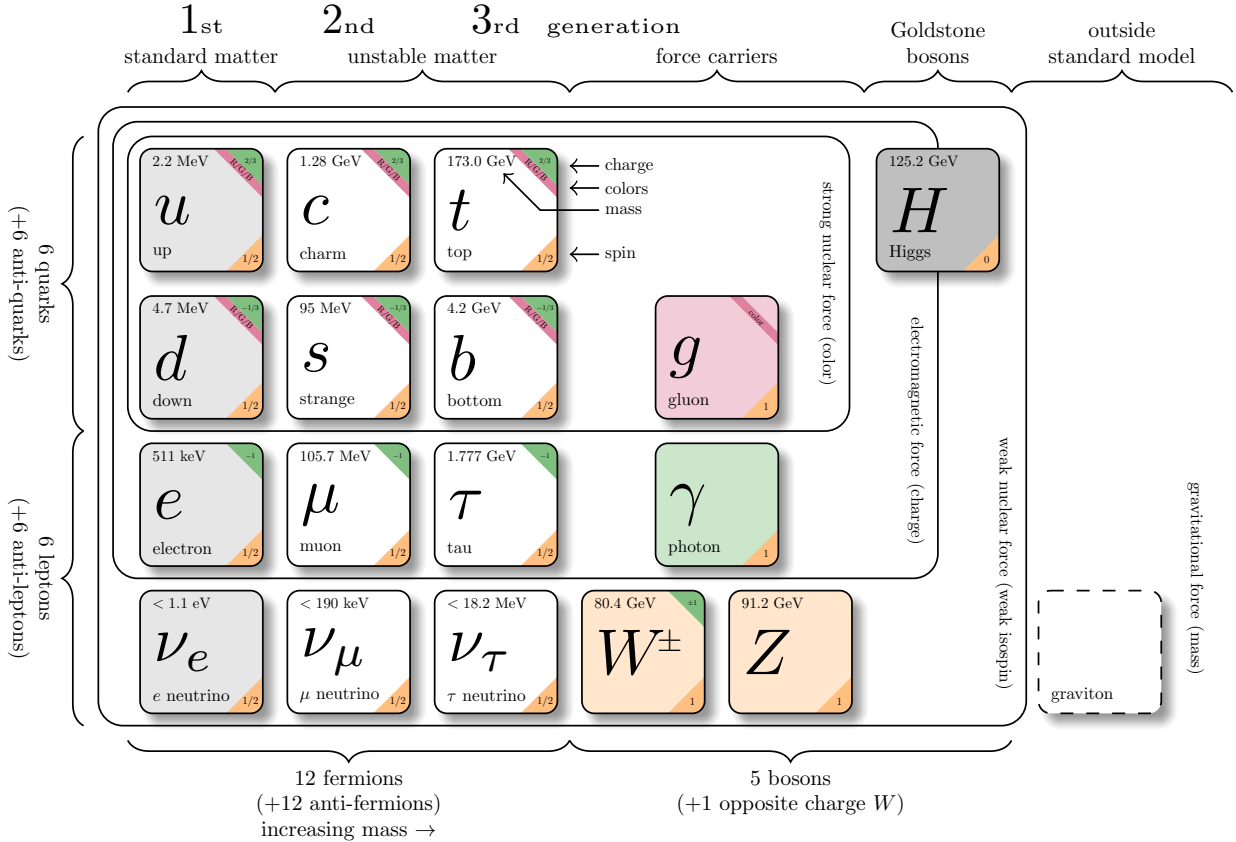


Figure 4.1: The Standard Model. Inspired by Purcell [77] using the template by Burgard [31] with manually updated masses according to Particle Data Group et al. [73].

<sup>4</sup> The photon, the  $Z$ , and the Higgs.

All particles have antiparticles which are particles with opposite charge but the same mass. Some particles are their own antiparticles<sup>4</sup>, such as the  $Z$ . At the Large Electron Positron collider (LEP), see section 4.3, electrons  $e^-$  and their antiparticles positrons  $e^+$  were collided at an energy of around 91 GeV. This particular energy was chosen since this is at the resonance peak of the  $Z$ . Its mass distribution follows a Cauchy distribution (also known as Breit-Wigner) with mean<sup>5</sup>  $m_Z = (91.1876 \pm 0.0021)$  GeV and a full width of  $\Gamma_Z = (2.4952 \pm 0.0023)$  GeV: LEP was as such a  $Z$ -factory. The  $Z$ , however, is only very short-lived with a half-life of  $1/\Gamma_Z \sim 2.6 \times 10^{-25}$  s. The decay mode for this unstable  $Z$  particle is primarily to hadrons ( $(69.91 \pm 0.06)\%$ ) where the ratio (R) for  $b$ -quarks is  $R_b = (Z \rightarrow b\bar{b}) = (15.12 \pm 0.05)\%$  and  $R_g = (Z \rightarrow ggg) < (1.10 \pm 0.05)\%$  for gluons [73]. The fact that the  $Z$  is neutral and its own anti-particle means that it generally decays to a particle-anti-particle pair (due to charge-conservation). Antiparticles are written with a bar on top, e.g. the  $\bar{b}$ -quark is the antiparticle of the  $b$ -quark.

## 4.2 Quark Hadronization

The electron-positron  $e^+e^-$  annihilations at LEP are complicated events that require advanced high-energy particle physics theory to be properly understood. Most of the aspects of the process is well-described by now, however, especially the hadronization process is still an area

<sup>5</sup> Calculated in natural units where  $c = \hbar = 1$  which will also be used throughout this thesis.

of active research. To better get an overview of the different stages of the  $e^+e^-$  annihilations, see the Feynman diagram in Figure 4.2.

Reading from left to right, the electron and the positron annihilates to a  $Z$ . This interaction is well-described by quantum electrodynamics (QED), a theory that has been around for more than 60 years by now. As mentioned in the previous section, the  $Z$  has several decays modes, yet most of these are background processes of no interest in this project and the focus for now will be the decay mode  $Z \rightarrow q\bar{q}$  ( $Z$  to quark-anti-quark) as seen in the Feynman diagram. The particles produced by the  $Z$ -decay are called primary *partons*. Since this process involves quarks, and thus color charge, QED is no longer an adequate theory: quantum chromodynamics (QCD) is needed [16]. The  $q\bar{q}$  pairs in this example acts as (color) dipoles from which a gluon can radiate. It can be shown with QCD that the gluon can only be radiated inside the cone that the  $q\bar{q}$  pairs spans [24]. As mentioned in the introduction, quarks cannot exist freely (due to *confinement*) and we therefore cannot observe the individual partons in a  $q\bar{q}g$  event produced in the Feynman diagram. Confinement is basically the QCD principle saying that quarks are always confined or bound inside hadrons. The initial partons (carrying color charge) are converted to (color-neutral) hadrons by non-perturbative QCD processes in what is called *hadronization*, and these hadrons can be measured.

The hadronization process is not yet fully modelled and currently two competing models for predicting the hadronization pattern exists: the Lund string model and the cluster model. In this project only the former of the models will be used. The Lund string model [15] is the theoretical framework underlying the widely used Monte Carlo event generator PYTHIA [85]. The string model is based on the observation that (color) field lines between quarks seem to compress into a tube-like region mediated by gluons, see the top part of Figure 4.3. The field can be described by a linearly rising potential  $V(r) = \kappa r$  at large distances<sup>6</sup>, where  $r$  is the distance and  $\kappa$  is the strength of the potential [30]. This field is similar to the (constant) force of a string:  $V(r) = \kappa r \Rightarrow F(r) = -\kappa$  where  $\kappa$  is the to be regarded as the spring tension. As quarks move apart, the potential energy stored in the “string” increases until it is large enough to “snap” and convert its potential energy into mass. This mass energy is released with the production of a new  $q\bar{q}$  pair as this energetically favorable, see the rest of Figure 4.3.

An example of the hadronization process, or the transition from initial partons to final hadrons is sketched in Figure 4.4. Here the production of two kaons  $K^-$  and  $K^+$ , and two pions  $\pi^-$  and  $\pi^0$  are shown. Since particles are created by “splits” in the “string”, and the fact that there is energy-momentum conservation, they all have to share the total energy stored in the string. This is described by the fragmentation function:

$$f(z) \propto \frac{(1-z)^a}{z} \exp\left(-\frac{bm^2}{z}\right), \quad (4.1)$$

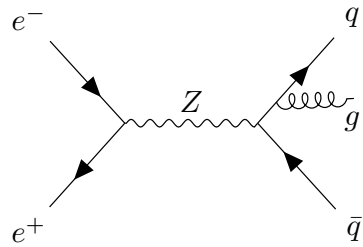


Figure 4.2: Feynman diagram showing the  $e^+e^- \rightarrow Z^0$  production at LEP. The  $Z$  has several decay modes where the  $Z \rightarrow q\bar{q}g$  is shown here.

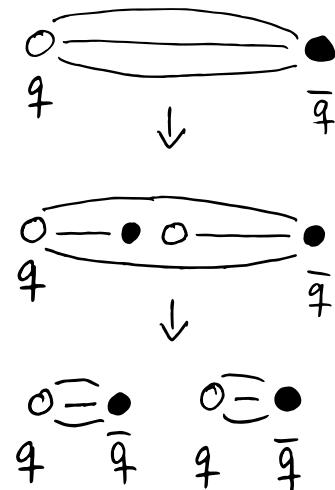
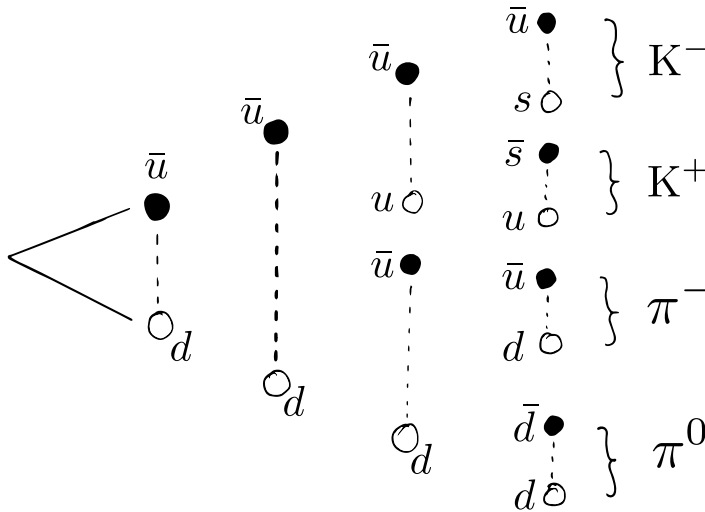


Figure 4.3: Illustration of the quarks splitting as explained by the Lund string model. For large charge separation the (color) field lines seem to be compressed to a tube-like region, where the strong interactions are mediated by the massless gluons (that couple to the color charge of quarks). When the two quarks are separated enough, the potential energy is released by the production of a new  $q\bar{q}$  pair.

<sup>6</sup> At small distances a Coulomb term has to be included, however, this term is assumed to be negligible by the Lund string model.

where  $0 \leq z \leq 1$  is the remaining momentum that the new hadron takes,  $a$  and  $b$  are constants, and  $m$  is the mass<sup>7</sup> [24]. When the system runs out of available momentum, it will stop producing new hadrons and the fragmentation function thus explains the distribution of final state particles. The Lund string model can be extended from only  $q\bar{q}$  events to  $q\bar{q}g$  events where it predicts cones spanning the angular regions  $qg$  and  $\bar{q}g$  should receive enhanced particle production compared to the  $q\bar{q}$  region. This prediction by the Lund string model is also measured in  $e^+e^-$  collisions [30].



<sup>7</sup> Where  $m \rightarrow m_\perp$  for particles with transverse momentum.

Figure 4.4: Illustration of the hadronization process by which  $\bar{u}$ - and  $d$ -quarks decay into four different mesons. The theoretical strings are shown as dashed lines and particles as circles, where filled circles are antiparticles.

The initial partons produced as  $Z$  decay therefore decay to final state hadrons<sup>8</sup> which create a whole “shower” in the direction of the initial parton: this is called a *parton shower* and it is this parton shower observed as particles, a *jet*, that is measured in the detector. The reverse computation from tracks measured in the detector is done with the use of *jet clustering* algorithms. The detector and the clustering algorithms are described in the following section.

### 4.3 The ALEPH Detector and LEP

The Large Electron Positron collider (LEP) was a particle collider at CERN in Switzerland operating from 1989 to 2000. It collided counter-rotating bunches of electrons and positrons in a giant ring with a circumference of more than 26 km. The first phase, LEP1, ran from 1989 to 1995 at the  $Z$  resonance 91 GeV and the second phase, LEP2, continued afterwards closer to 200 GeV for  $W^+W^-$  pair production [16], however, it is only the data collected at the energy around  $\sqrt{s} = 91.3$  GeV called the  $Z$  peak data that is used throughout the rest of this project. There were four independent detectors at the LEP experiment, one of them ALEPH<sup>9</sup>.

The apparatus for LEP physics (ALEPH) was a particle detector at LEP with a wide coverage, almost  $4\pi$ , consisting of cylindrical sub-detectors, see Figure 4.5, with the coordinate system shown in the upper left corner<sup>10</sup>. The polar angle  $\theta$  is illustrated in Figure 4.6

<sup>8</sup> To either mesons which consist of two quarks (color-anti-color) or baryons (r-g-b) which consist of three quarks.

<sup>9</sup> Together with DELPHI, L3, and OPAL.

<sup>10</sup> The  $z$ -axis pointing along the beam direction, the  $y$ -axis pointing upwards, and the  $x$ -axis pointing towards the center of LEP.

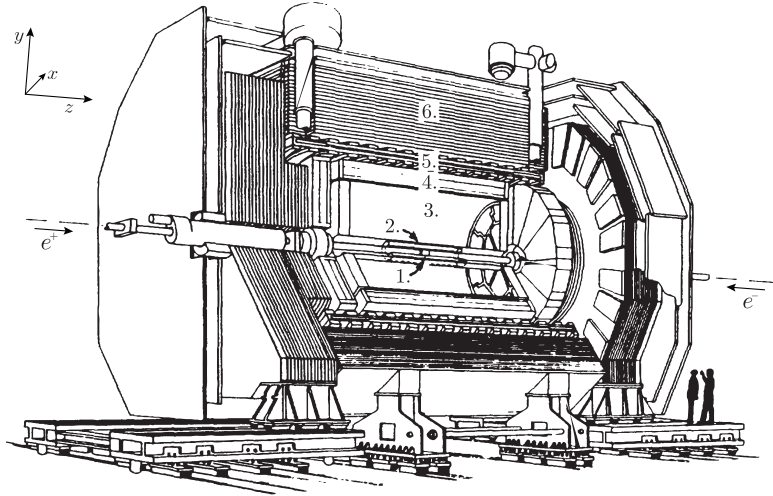


Figure 4.5: The ALEPH detector at LEP. 1) Vertex detector (VDET). 2) Drift chamber (ITC). 3) Time projection chamber (TPC). 4) Electromagnetic calorimeter (ECAL). 5) Superconducting magnet coil. 6) Hadron calorimeter (HCAL). Adapted from Buskulic et al. [32].

together with the transverse (longitudinal) momentum  $p_{\perp}$  ( $p_L$ ) and the azimuthal angle  $\phi$  in Figure 4.7. The ALEPH detector was designed to measure the energy deposited in calorimeters by charged and neutral particles, measure the momenta of charged particles, measure the distance of travel of short-lived particles, and to identify the three lepton flavors (electron, muon, tau) [32]. As can be seen in Figure 4.5, ALEPH consisted of five subdetectors (the vertex detector (VDET), the drift chamber (ITC), and the time projection chamber (TPC)) and two calorimeters (the electromagnetic (ECAL) and the hadronic calorimeters (HCAL)).

The three innermost detectors allow for precise tracking of the charged particles produced in the parton shower and the two outer calorimeters of precise energy measurements for both charged and neutral particles going through the detector.

A hadronic event from a parton shower may leave a score of charged tracks resulting in hundreds of hits in the detectors (VDET, ITC, and TPC) which are fitted<sup>11</sup> with Kalman filters [60] to obtain global track fits, of which bad charged tracks are discarded for further analysis. The tracks are helical due to the presence of a 1.5 T magnetic field which curves the charged particles according to their transverse momentum,  $p_{\perp}$ .

The energy resolution  $\sigma$  of the calorimeters, or the *calorimeter performance*, is expected to increase with  $\sqrt{E}$ . In fact, it was found at ALEPH that the energy dependence of the resolution follows the parametrization [32]:

$$\sigma(E) = \left( (0.59 \pm 0.03) \cdot \sqrt{E/\text{GeV}} + (0.6 \pm 0.3) \right) \text{GeV}. \quad (4.2)$$

Even though  $\sigma(E)$  increases with  $E$ , the relative resolutions improves with higher energies. Since one never measures Nature directly, the results one obtains in a measurement are thus products of both model and experimental uncertainties folded together. To unfold the measurements to obtain experiment-independent results, the uncertainties are important to understand. Of course there are dozens of

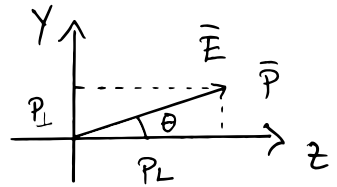


Figure 4.6: The polar angle  $\theta$  defined in the  $zy$  coordinate system

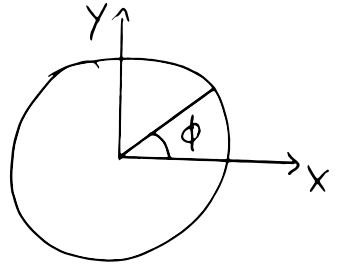


Figure 4.7: The azimuthal angle  $\phi$  defined in the  $xy$  coordinate system.

<sup>11</sup> the process of fitting tracks is called *track reconstruction* in high energy particle physics.

other uncertainties in an advanced experiment like ALEPH, however, the energy dependence is the primary focus in this project.

#### 4.4 Jet clustering

Since the initial partons created as decay products from the  $Z$  are unstable themselves, what is measured in the detector is a whole shower of hadrons seen as charged tracks in the detectors and energy deposits in the calorimeters. However, say that the  $Z$  decayed to a  $b\bar{b}$  event. In this case the two  $b$ 's would be back-to-back and the final hadrons would be observed approximately in the same direction as the  $b$ 's were created. The interest of the experiment is not to measure the final hadrons, but rather to infer information about the initial quarks and gluons. This is done via the reverse-engineering process called *jet clustering*. Over the years many clustering algorithms have been developed, however, most of these are younger than LEP. In the ALEPH experiment the JADE algorithm was used [20]. JADE is a sequential recombination algorithm where final state particles are initially described as individual so-called pseudo-jets which are then recursively merged to larger jets according to their inter-jet distance  $d_{ij}^2$ . The distance measure for JADE is:

$$d_{ij}^2 = \frac{2E_i E_j (1 - \cos \theta_{ij})}{E_{\text{vis}}^2}, \quad (4.3)$$

where  $E_{\text{vis}}$  is the visible energy<sup>12</sup> and  $\theta_{ij}$  is the angle between jet  $i$  and  $j$ . The JADE algorithm computes  $d_{ij}^2$  for all combinations of jets and merges the two jets with the lowest  $d_{ij}^2$ , continuing like that recursively until  $\min(d_{ij}^2) > d_{\text{cut}}^2$  for some predefined value of  $d_{\text{cut}}^2$ . In the dataset at hand, only the final jets were available and not the jet constituents, unfortunately.

<sup>12</sup> The total sum of energies in the event.

#### 4.5 The variables

The overall goal of the project is to be able to discriminate quarks and gluons using only vertex variables. The reason for the last condition is that the goal is to better understand the shape distributions of gluons in which there is still significant differences between Monte Carlo (MC) simulations and Data. Therefore only vertex variables will be used to avoid any biases introduced by using shape-related variables to detect differences in shape-distributions. The vertex variables are a subset of all variables which include the three variables `projet`, `bqvjet`, and `ptlrel`. These three particular variables have each shown discriminatory power in separating  $b$ -quarks from light quarks and gluons.

`projet`: PROBABILITY OF SIGNIFICANT LIFETIME. For each track in the jet an impact parameter  $\delta$  is computed. This parameter is the minimum distance between the estimated  $Z$  decay point

and the track itself and its sign depends on whether or not the point of closest approach is in front of or behind the  $Z$  decay point (relative to the momentum). From  $\delta$  the significance  $\mathcal{S}$  – which is  $\delta/\sigma_\delta$  – is computed and is thus a measure of the certainty of a measured track being from primary vertex. High values of  $\mathcal{S}$  is typically an indicator of  $b$  jets, since long-lived particles typically decay in front of the  $Z$  relative to the jet direction, while  $uds$ -jets generally have small significance and might as well have negative values of  $\mathcal{S}$ . An illustration of the difference in significance between  $uds$ -jets and  $b$ -jets can be seen in Figure 4.8.

From  $\mathcal{S}$  the track probability  $\mathcal{P}_{\text{track}}$  of a track originating at the decay point of the  $Z$  can be computed, which can further be aggregated across all tracks within a jet to form the jet probability  $\mathcal{P}_{\text{jet}}$  which `projet` is a function of [46]. Whether or not  $\mathcal{P}_{\text{jet}}$  is strictly a probability can be discussed but it is related to the probability of all tracks within a jet to originate from long-lived particles, which itself is a good indicator of being a  $b$ - (or  $c$ -) jet. This variable further has the advantage of being independent of any vertex algorithm.

`bqvjet`:  **$b$ -QUARK VERTEX OF JET.** For any jet with well measured<sup>13</sup> charged tracks, a fit with a (hypothetical) secondary vertex is performed. The difference in  $\chi^2$  between the null hypothesis that all good tracks originate from the same primary vertex and the alternative hypothesis that a secondary vertex exists in addition to the primary one is calculated. For the long-lived massive  $b$  and  $c$  quarks this typically results in large differences in  $\chi^2$  compared to  $uds$ - and gluon jets which have much lower  $\Delta\chi^2$ -values [16]. The `bqvjet` is related to the  $\Delta\chi^2$ -value from the secondary vertex algorithm. This value is dependent of the vertex algorithm, but still explores other areas of phase space than `projet`, however, they are still very correlated. The linear correlations<sup>14</sup>  $\rho_{q_i}$  between `projet` and `bqvjet` for  $q_i$  jets are  $\rho_b = 0.80, \rho_c = 0.65, \rho_{uds} = 0.23, \rho_g = 0.29$ .

`ptlrel`: **RELATIVE LEPTON MOMENTUM.** If any leptons (in the case of  $e^\pm$  or  $\mu^\pm$ ) are measured in the jet by the detector, this is a good sign of the jet originating from a  $b$ -quark as  $\sim 11\% (e) + \sim 11\% (\mu)$  decay semi-leptonically [13]<sup>15</sup>. The high mass of the  $b$  quark leads to high  $p_\perp$  for the leptons relative to the jet axis which is exactly measured by `ptlrel`.

The fact that the heavy  $b$ -quarks have much longer lifetimes than the lighter  $uds$ -quarks stems from their much lower coupling magni-

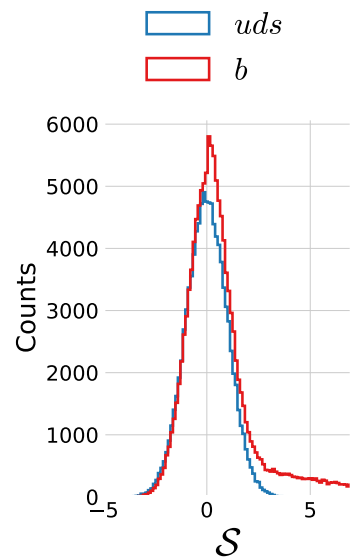


Figure 4.8: Distribution showing the difference in significance  $\mathcal{S}$  between  $uds$ -jets and  $b$ -jets. Based on own, simulated data to illustrate this difference.

<sup>13</sup> Meaning that there are at least four TPC hits and the fit has a reduced  $\chi^2$  of less than four [16].

<sup>14</sup> Based on MC truth.

<sup>15</sup>  $\mathcal{B}(B^- \rightarrow l\nu X) = (10.5 \pm 0.3)\%$ ,  $l = \{e, \mu\}$  [13].

tudes written as the CKM matrix  $\mathbf{V}$  [73]:

$$\mathbf{V} = \begin{pmatrix} d & s & b \\ u & \begin{pmatrix} 0.97446 & 0.22452 & 0.00365 \\ 0.22438 & 0.97359 & 0.04214 \\ 0.00896 & 0.04133 & 0.99911 \end{pmatrix} \\ c \\ t \end{pmatrix}. \quad (4.4)$$

The matrix element  $|V_{ij}|^2$  is proportional to the transition-probability of quark  $i$  transitioning to quark  $j$ . From the CKM matrix it can be seen that  $u$  and  $d$  quarks couple strongly together, likewise with  $c$ - $s$  and  $b$ - $t$  quark pairs. When a  $Z$  decays into a  $b$ -quark, this quark couples strongly with the top quark, however, due to the high mass of the top quark compared to the  $b$ -quark, the  $b$ -quark cannot decay into a  $t$ -quark but must (almost always) decay to a  $c$ , however, still with low probability,  $V_{bc} \ll 1$ . This, together with the fact that  $V_{bu} \ll V_{bc}$  explains the long life-time of  $b$  quarks,  $\tau_b \sim 1.3 \times 10^{-12}$  s [80]. This is also why the three variables above are very common variables for  $b$ -tagging algorithms. That  $c$ -quarks also have relative long life-times,  $\tau_c \sim 1.1 \times 10^{-12}$  s [80], are not due to the CKM elements, as for  $b$ -quarks, but rather due to the  $c$ -decay being governed by the weak force through virtual  $W^*$  bosons, a force that is much weaker than the strong force (hence the name). The low phase space in a  $c$ -quark decay makes the  $c$ -quark longer-lived. This also happens for  $b$ -quarks which further explains why  $c$ -quarks share many similarities with  $b$ -quarks but also resembles light-quarks (which are very long-lived.).

The rest of the non-vertex variables are:

`ejet` : The energy of the jet  $E_{\text{jet}}$

`costheta` : The cosine of the  $\theta$  angle defined in Figure 4.6.

`phijet` : The angle  $\phi$  of defined in Figure 4.7:  $\phi$ .

`sphjet` : The sphericity tensor  $\mathbf{S}$  is defined as:

$$S^{(\alpha\beta)} = \frac{\sum_{i=1}^N p_i^{(\alpha)} p_i^{(\beta)}}{\sum_{i=1}^N |p_i|^2} \quad \alpha, \beta \in \{x, y, z\}, \quad (4.5)$$

and the sphericity is determined as  $S = \frac{3}{2}(\lambda_2 + \lambda_3)$  where  $\lambda_1 \geq \lambda_2 \geq \lambda_3$ ,  $\lambda_1 + \lambda_2 + \lambda_3 = 1$  are the three eigenvalues of the sphericity tensor. The sphericity  $0 \leq S \leq 1$  is a measure of the angular distribution of the tracks and clusters in a jet. When  $S = 0$  the jets form a perfect sphere, compared to  $S = 1$  for a perfect line. The `sphjet` variable is the sphericity of the jet when calculated in its boosted rest frame, also known as *boosted sphericity*.

`pt2jet` : The sum of the square of transverse momentum w.r.t. the jet axis:  
 $\sum_i p_{\perp,i}^2$ .

`muljet` : The rescaled multiplicity of the jet.

For further details about the variables, see Armstrong [16].

The variables explained above are all used in the following analysis where the machine learning model is trained on only the vertex variables to probe differences in the shape-variables. The goal of this is to better understand the gluon hadronization process to minimize differences in MC simulations and ultimately get a better understanding of the rules governed by Nature.



# 5. Quark Gluon Analysis

*“Research is what I am doing I don’t know know what I’m doing.”*

---

— Wernher von Braun

THE ANALYSIS of the quarks and gluons that were introduced in the previous chapter is described here. The overall goal is to be able to discriminate between quark and gluon jets to better be able to describe the gluon jets. The gluon jet distributions are measured in 3-jet events and how they split in 4-jet events. This chapter is organized as follows. In [section 5.1](#) the data are presented and the initial cuts are described and the variables are visualized in [section 5.2](#). The choices of loss and evaluation function are discussed in [section 5.3](#). In [section 5.4](#) the first of the two overall models developed in this chapter is presented, the *b*-tagging model. The efficiency of this model is measured in [section 5.5](#). The second model, the *g*-tagging model is used for classification of entire events, compared to the *b*-tagging model which classifies individual jets, and is introduced in [section 5.6](#) and its efficiency is measured in [section 5.7](#). The jet distributions in 3-jet events are analyzed in [section 5.8](#) and their the gluon splitting in 4-jet events in [section 5.9](#). Finally the quark gluon project is discussed in [section 5.10](#).

## 5.1 Data Preprocessing

The data files were acquired from Prof. Peter Hansen (NBI) who worked on the ALEPH experiment. The Data consists of 43 data files from between 1991 and 1995 totalling 3.5 GB (Data). Along with this comes 125 files based on Monte Carlo (MC) simulations (8.4 GB) and additional 42 MC-files with only *b*-quark events (MC<sub>b</sub>) (2.1 GB). The data files which are in the form of *Ntuples*, ROOT’s data format [[29](#)], are converted to HDF5-files by using the Python package `uproot` [[7](#)]. While iterating over the Ntuples, some basic cuts are applied before exporting the data to HDF5-format. The first one being that the (center of mass) energy  $E$  in the event has to be within  $90.8 \text{ GeV} \leq E \leq 91.6 \text{ GeV}$  to only use the  $Z$  peak data. The second one being that the sum of the momenta  $p_{\text{sum}}$  in each event is  $32 \text{ GeV} \leq p_{\text{sum}}$  to remove  $Z \rightarrow \tau^+ \tau^-$  events. To ensure a primary vertex, at least two good tracks are required where a good track is

defined as having at least 7 TPC hits and 1 silicon hit or more. Finally it is required that the cosine of the thrust axis polar angle, which is the angle between the thrust axis and the beam, is less than or equal to 0.8 to avoid any low angle events since the detector performance worsens significantly in that region. These cuts were standard requirements for the ALEPH experiment.

One last cut which was experimented with was the threshold value for *jet matching*. The jet matching is the process of matching the jet with one of the final state quarks. The jet is said to be matched if the dot product between the final quark momentum and the jet momentum is more than then threshold value. Higher thresholds means cleaner jets but at the expense of less statistics. A jet matching threshold of 0.90 was found to be a good compromise between purity and quantity where 97.8% of all 2-jet events are matched and 96.7% of all other jets were matched<sup>1</sup>.

The data structure is quite differently structured in the Ntuples compared to normal structured data in the form of tidy data [101]. The data is organized such that one iterates over each event where the variables are variable-length depending on the number of jets in the events; this is also known as *jagged arrays*. The data is un-jagged<sup>2</sup> before exporting to HDF5-format and only the needed variables are kept. This reduces the total output file to a 2.9 GB HDF5-file including both Data, MC, and MCb.

The number of events for each number of jets can be seen in Table 5.1 for the Data and in Figure 5.2 for the MC and MCb.

## 5.2 Exploratory Data Analysis

Since the machine learning models are only trained on the three vertex variables `projet`, `bqvjet`, and `ptljet` – see chapter 4 for a deeper introduction to these variables – these variables will be the primary focus of this section. Given the fact that MC-simulated data exists, the truth of each simulated event is also known. This allows us visualize the difference between the different types of quarks. In the MC simulation each event are generated such that the type of quark, or *flavor*, is known and assigned the variable `flevt`. The mapping from flavor to `flevt` is:

Flavor:	<i>bb</i>	<i>cc</i>	<i>ss</i>	<i>dd</i>	<i>uu</i>
<code>flevt</code> :	5	4	3	2	1

In addition to knowing the correct flavor, we define that an event is *q-matched* if one, and only one, of the jets are assigned to one of the (final) quarks, if one, and only one, of the jets are assigned to the other (final) quark, and if no other jets are matched to any of the (final) quarks. We then define what constitutes a *b*-jet: if it has `flevt` = 5, the entire event is *q*-matched, and the jet is matched to one of the quarks. Similarly we define *c*-jets only with the change that `flevt` = 4, and *uds*-jets<sup>3</sup> with `flevt` ∈ {1, 2, 3}. A gluon

<sup>1</sup> Compare this to 98.5 % and 97.8 % for a threshold of 0.85 or 95.9 % and 93.9 % for a threshold of 0.95.

<sup>2</sup> Such that e.g. a 3-jet event will figure as three rows in the dataset.

<i>n</i>	# jets	# events
2	2 359 738	1 179 869
3	3 619 290	1 206 430
4	854 336	213 584
5	52 775	10 555
6	510	85
Total	6 886 649	2 610 523

Table 5.1: The dimensions of the dataset for the actual Data for *n*-jet events. The numbers in the jet columns are the number of events multiplied with the number of jets; e.g.  $85 \cdot 6 = 510$ .

<i>n</i>	# jets	# events
2	7 293 594	3 646 797
3	10 780 890	3 593 630
4	2 241 908	560 477
5	103 820	20 764
6	588	98
Total	20 420 800	7 821 766

Table 5.2: The dimensions for the MC and MCb datasets for *n*-jet events.

<sup>3</sup> Will also be called a *l*-jet.

jet is defined to be a jet in a (any-flavor)  $q$ -matched event where the jet itself is not assigned to any of the (final) quarks. Strictly speaking, this means that the gluon jet is not 100% certain of being a gluon. We cannot know this, as not all of the input parameters in the MC simulation are known, only the final clustered jets. Due to the  $q$ -match criterion this also means that some jets are assigned the label “non- $q$ -matched” which is regarded as background. The distribution of different types of jets can be seen in Table 5.3 and shown as relative numbers in Table B.1.

$n$	$b$	$c$	$uds/l$	$g$	non- $q$ -matched
2	2 713 454	944 380	2 125 900	0	1 509 860
3	2 433 878	964 212	2 129 218	3 365 969	1 887 613
4	326 264	156 332	336 548	1 012 198	410 566
5	10 332	5 960	12 668	54 525	20 335
6	42	26	52	320	148
Total	5 483 970	2 070 910	4 433 012	4 604 386	3 828 522

Table 5.3: Number of different types of jets for MC and MCb for  $n$ -jet events. See also Table B.1 for relative numbers.

With the criteria defined above for what constitutes a specific type of jet the 1D-distributions for the three vertex variables are plotted in Figure 5.1. For all three subplots the histograms are shown with logarithmic  $y$ -axes, all  $b$ -jets in blue,  $c$ -jets in red,  $g$ -jets in green, and all of the jets (no matter their type) are shown in orange. The distributions for 2-jet events are shown in fully opaque color, 3-jet events in dashed lines, and 4-jet events in lighter colors. In the left subplot the `projet` variable is plotted where it can be seen that high values of `projet` tend to indicate  $b$ -jets. In the middle subplot `bqvjet` is plotted which shares many similarities with the `projet` variables, including that high values indicate  $b$ -jets. In the right subplot the `ptljet` is plotted. This variable has many zeros in it which correlates with mostly with gluons<sup>4</sup> and large values are mostly due to  $b$ -jets. In general it is clear to see how the differences in distribution between the 2-, 3-, and 4-jet events are minor, with the one exception of 2-jet events which does not contain any gluons at all.

<sup>4</sup> Around 98% of all  $g$ -jets are zeros for the variable `ptljet` compared to  $\sim 82\%$  for  $c$ -jets and  $\sim 70\%$  for  $b$ -jets.

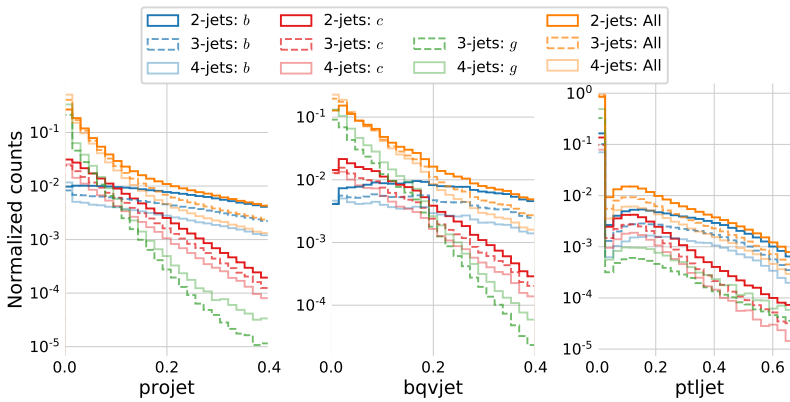


Figure 5.1: Normalized histograms of the three vertex variables: `projet`, `bqvjet`, and `ptljet`. In blue colors the variables are shown for **true  $b$ -jets**, in red for **true  $c$ -jets**, in green for **true  $g$ -jets**, and in orange for **all of the jets** (including non  $q$ -matched). In fully opaque color are shown the distributions for 2-jet events, in dashed (and lighter color) 3-jet events, and in semi-transparent 4-jet events. Notice the logarithmic  $y$ -axis, that there are no  $g$ -jets for 2-jet events (as expected), and that all of the distributions are very similar no matter how many jets.

### 5.2.1 Dimensionality Reduction

Even though there are only three vertex variables, it is difficult to properly get an intuition about how easily separated the different types of jets are. Since there are millions of points a single 3D scatter plot quickly becomes overcrowded if one plots all jets. We apply dimensionality reduction from the three dimensions down to two dimensions by using the UMAP algorithm [70]. Within recent years the field of dimensionality reduction algorithms has grown a lot from just the typical (linear) principal component analysis to also include nonlinear algorithms. The t-SNE algorithm [95] deserves an honorable mention since this algorithm revolutionized the usage of (non-linear) dimensionality reduction algorithms in e.g. bioinformatics [92, 99] yet its mathematical foundation has strongly been improved with the newer, faster UMAP algorithm [70] which usage is also expanding [21, 22, 42].

The aim of UMAP, short for Uniform Manifold Approximation and Projection, is to correctly identify and preserve the structure, or topology, of the high-dimensional feature space in a lower-dimensional output space. It does so by trying to stitch together local manifolds in the high-dimensional feature space such that the difference between the high- and low-dimensional representations is minimized according to the cross-entropy such that both global structure and local structure is preserved [70]. Compared to t-SNE the approach in UMAP has a topological background compared to the more heuristic approach taken by t-SNE. Note that the UMAP algorithm is not provided any information about which jets are which types or any other truth information.

The UMAP algorithm has several hyperparameters, where two of the most important ones are the number of neighbors `n_neighbors` which controls the priority between correctly preserving the global versus the local structure, and the `min_dist` which defines how tightly together UMAP is allowed to cluster the points in the low-dimensional representation. To properly choose the best combination of `n_neighbors` and `min_dist` a grid search with `n_neighbors`  $\in \{10, 50, 100, 250\}$  and `min_dist`  $\in \{0, 0.2, 0.5\}$  is performed. This is shown for 4-jet events in Figure B.1.

The best combination of `n_neighbors` and `min_dist` is subjective at best, but I judged that `n_neighbors = 250` and `min_dist = 0.2` gave the best compromise between preserving local and global structure. The results of running UMAP on 4-jet events can be seen in Figure 5.2. Here the millions of points are plotted using Datashader [8] to avoid overplotting and colored according to the jet type. From the figure it is seen how there are some clear *b*-jet clusters, however, most of the data seem to be a mix of *g*-and *uds*-jets. The plots with the same UMAP parameters for 3-jet and 2-jet events are seen in Figure 5.3 and 5.4.

These figures suggest that it should be possible to discriminate the *b*-jets from the other jets somewhat, however, no clear separation is

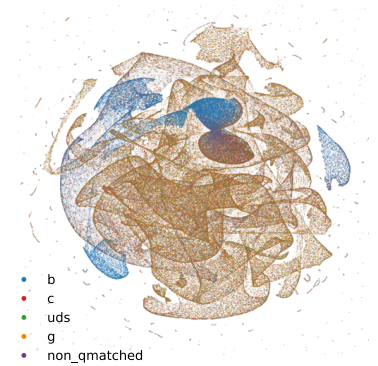


Figure 5.2: Visualization of the vertex variables in 4-jet events for the different categories: **true *b*-jets** in blue, **true *c*-jets** in red, **true *uds*-jets** in green, **true *g*-jets** in orange, and **non *q*-matched** events in purple. The clustering is performed with the UMAP algorithm which outputs a 2D-projection. This projection is then visualized using the Datashader which takes care of point size, avoids over and underplotting, and color intensity.

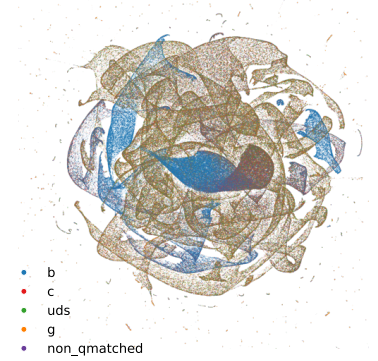


Figure 5.3: UMAP visualization of vertex variables for 3-jet events.

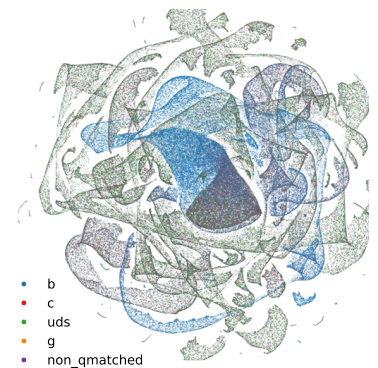


Figure 5.4: UMAP visualization of vertex variables for 2-jet events.

expected. The t-SNE algorithm was also tested but showed inferior performance compared to UMAP, see Figure B.2 for an example of this.

### 5.2.2 Correlations

The correlation between the vertex variables can be seen in Figure 5.5, where the upper diagonal shows the linear correlation  $\rho$  and the lower diagonal shows the nonlinear correlation  $\text{MIC}_e$  introduced in subsection 3.1.1. Here it can be seen that `projet` and `bqvjet` are the two variables that correlate the most whereas the other variables correlate a lot less. Had they all correlated a lot, it would be more difficult to extract any meaningful insights from the system as it would contain less information.

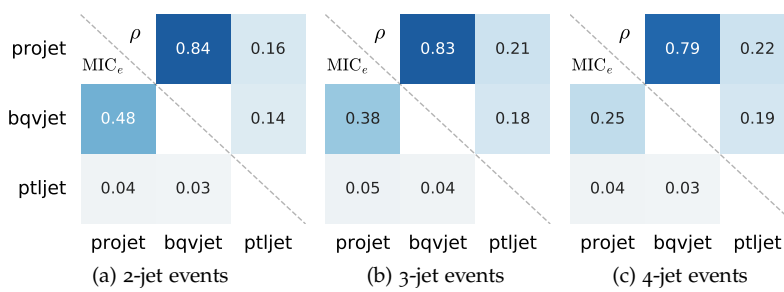


Figure 5.5: Correlation of the three vertex variables for 2-, 3- and 4-jet events. Here the upper diagonal shows the linear correlation  $\rho$  and the lower diagonal the nonlinear correlations  $\text{MIC}_e$ .

### 5.3 Loss and Evaluation Function

In contrary to the housing prices project, the goal in this project is to predict types of jets or events where the *signal* observations<sup>5</sup> are often assigned the label 1 and *background* observations 0. The combination of this being a *classification* problem (compared to a regression problem) along with the fact all the variables are actual measurements from a particle physics accelerator means that the issue of outliers is negligible. This also means that the problem of finding a robust loss function is less important since the in classification loss is already bounded in the  $[0, 1]$ -interval.

*Accuracy*, which is simply the fraction of correct predictions, is often used as the loss function in classification, however, accuracy as a metric suffers a lot when handling *imbalanced* data: when the ratio between the number of instances of each class is not approximately fifty-fifty. The problem is that if the sample contains 90 % background and only 10 % signal, then a simple model which simply predicts everything to be background will have a 90 % accuracy.

To circumvent this issue, the area under the *ROC*<sup>6</sup> curve (*AUC*) is used, where the ROC curve is the the *signal efficiency*  $\varepsilon_{\text{sig}}$  of the ML model plotted as a function of the *background efficiency*  $\varepsilon_{\text{bkg}}$ . The definition of these two measures are:

$$\varepsilon_{\text{sig}} = \frac{S_{\text{sel}}}{S_{\text{tot}}}, \quad \varepsilon_{\text{bkg}} = \frac{B_{\text{sel}}}{B_{\text{tot}}}, \quad (5.1)$$

<sup>5</sup> Often called signal events, however, since a jet can also be signal, the term signal event is only used when the meaning is clear from the context.

<sup>6</sup> Receiver Operating Characteristic.

Strictly speaking it is not a function of the background efficiency, but rather  $\varepsilon_{\text{sig}}$  and  $\varepsilon_{\text{bkg}}$  plotted parametrically as functions of the threshold cut  $\hat{y}_{\text{cut}}$ .

where  $S_{\text{sel}}$  are signal events that were also selected (predicted) as signal by the ML model,  $S_{\text{tot}} = S_{\text{sel}} + S_{\text{rej}}$  is the total number of signal events (the selected and rejected), and likewise for background events  $B$ . Within the machine learning community the signal efficiency is called the true positive rate (TPR) and the background efficiency the false positive rate (FPR). For the rest of this project, the AUC will be the evaluation function  $f_{\text{eval}} = \text{AUC}$ , however, since this metric does not work on single observations it cannot be used as the loss function. Instead we will use the *log-loss* as the loss function<sup>7</sup> which in comparison to the AUC is not only differentiable for single predictions but also takes the certainty of the prediction into account. When using tree-based algorithms or neural networks one can compute not only whether or not a single observation is classified as signal or background but also a prediction score. This is a number in the  $[0, 1]$ -interval and the closer to 1 the score is, the more certain the model is of the prediction being signal. Given the prediction score  $\hat{y}$  and the true label  $y$ , the log-loss  $\ell_{\log}$  is calculated as:

$$\ell_{\log}(\hat{y}, y) = -y \log \hat{y} - (1 - y) \log(1 - \hat{y}). \quad (5.2)$$

This is visualized in Figure 5.6. Here it can be seen how the loss changes as a function of the prediction score. Notice that when  $y = 0$  the loss for  $\hat{y} = 1$  diverges towards  $\infty$  and likewise with  $y = 1$  and  $\hat{y} = 0$  (since  $\log 0$  diverges to  $-\infty$ ).

## 5.4 *b*-Tagging Analysis

The ability to discriminate between the different types of particles produced in a collision is obviously import to understand the results. Today much work go into tagging algorithms, e.g. *b*-tagging in ATLAS and CMS [83]. That *b*-quarks are tagged specifically is both due to *b*-quarks having more unique characteristics compared to e.g. *c*-quarks and are thus easier to tag, but also the fact that *b*-quarks are the second-heaviest of the quarks and are measured to better understand CP-violation<sup>8</sup> at LHC-b, contributes to the choice of tagging *b*-quarks. In ALEPH Proriol et al. [76] started the work of comparing different methods for *b*-tagging already in 1991. They concluded that a neural network had the best performance compared to e.g. a linear (Fisher) discriminant. The neural network used was a 3-layer neural network (NN) trained on nine variables and the outputted the prediction score `nnbjet`. From here on, this pre-trained network will be called NNB.

I split the data into training and test sets in such a way that the individual jets in an event are not split. The events are split in a (80-20)% train-test ratio.

### 5.4.1 *b*-Tagging Hyperparameter Optimization

Compared to the housing prices dataset, the number of observations  $N$  is a lot larger ( $3 \times 10^7 \gg 5 \times 10^5$ ), although the dimensionality

<sup>7</sup> In the context of machine learning this is the same as the *cross entropy*.

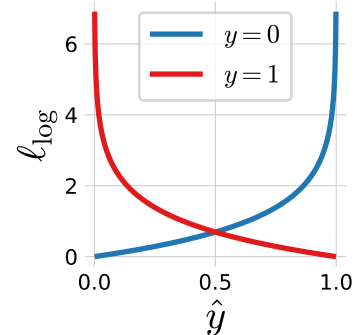
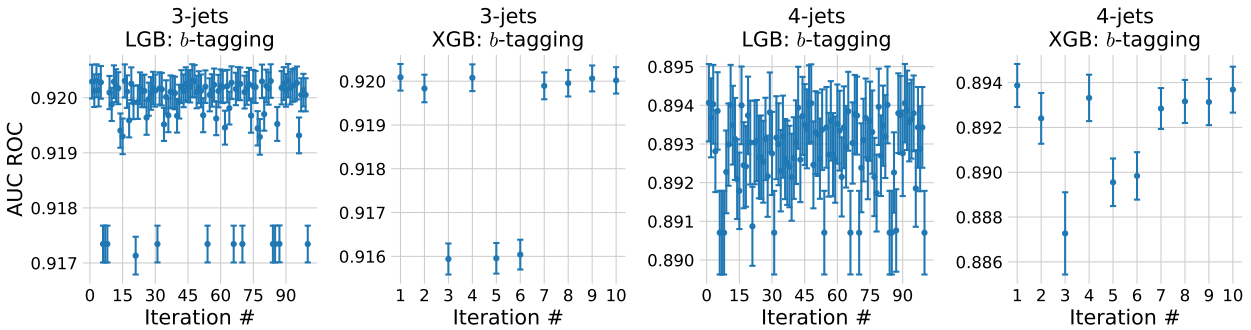


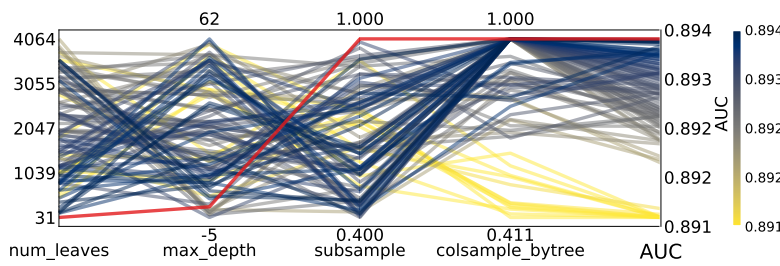
Figure 5.6: Plot of the log-loss  $\ell_{\log}$  for background ( $y = 0$ ) in blue and signal ( $y = 1$ ) in red.

<sup>8</sup> Short for charge-parity.

$M$  is much smaller ( $3 \ll 143$ ). Therefore both XGBoost (XGB) and LightGBM (LGB) were included as models initially since their performances in the housing dataset were very similar. LightGBM was expected to be faster on this dataset due to the large  $N$ . The models were hyperparameter optimized (HPO) using random search (RS) since the Bayesian optimization (BO) did not show any performance gains compared to RS in the housing project. They were both hyperparameter optimized with 5-fold cross validation and early stopping with a patience of 100. The PDFs for the random search for the LightGBM model can be seen in Table 5.4, and the ones for XGBoost in Table B.2. The random search has been run with 100 iterations for LightGBM and only 10 iterations for XGBoost since XGBoost turned out to be very slow<sup>9</sup> at fitting datasets of this size. The results of the HPO for 3-jet and 4-jet events can be seen in Figure 5.7. For 3-jets it can be seen how most of the iterations share about the same performance (within  $1\sigma$ ), however, some iterations show a significant decrease in performance. The same clear pattern is not seen in the 4-jet events.



The relationship between the different hyperparameters in 4-jet events can be seen in the parallel coordinate plot in Figure 5.8. First of all the importance of the column downsampling `colsample_bytree` variable is significant: all of the low-performing hyperparameter sets have a low value of this hyperparameter. Since  $M = 3$  for the vertex variables this makes logical sense; using only  $\text{int}(\sim 0.5 \cdot 3) = 1$  variable<sup>10</sup> the model cannot properly learn the structure in the data. Compared to the column downsampling, the other hyperparameters are less important. The same overall conclusion can be inferred in the 3-jet case, see Figure B.3.



Hyperparameter	Range
<code>subsample</code>	$\mathcal{U}(0.4, 1)$
<code>colsample_bytree</code>	$\mathcal{U}_{\text{trunc}}(0.4, 1, 2)$
<code>max_depth</code>	$\mathcal{U}_{\text{int}}(-5, 63)$
<code>num_leaves</code>	$\mathcal{U}_{\text{int}}(7, 4095)$

Table 5.4: Probability Density Functions for the random search hyperparameter optimization process for the LightGBM model. For an explanation of  $\mathcal{U}_{\text{trunc}}$ , see subsection 5.6.2. All negative values of `max_depth` are interpreted as no max depth by both LGB and XGB.

<sup>9</sup> See page 70 for a discussion of the timings.

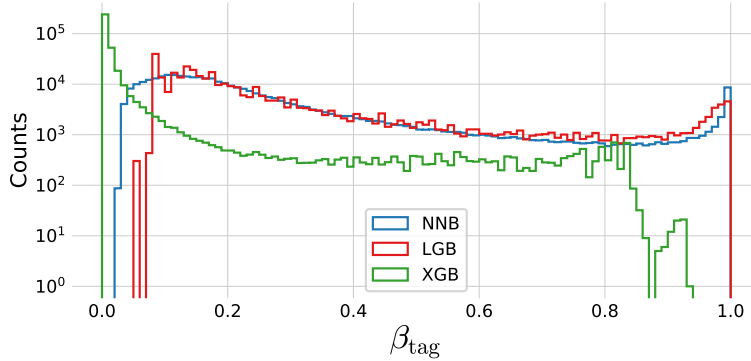
Figure 5.7: Hyperparameter Optimization results of *b*-tagging with random search. From left to right, we have A) 100 iterations of RS with LGB on 3-jets, B) 10 iterations of RS with XGB on 3-jets, C) 100 iterations of RS with LGB on 4-jets, D) 10 iterations of RS with XGB on 4-jets. Notice the different ranges on the y-axes.

<sup>10</sup> See subsection 5.6.2 for a deeper discussion about the `colsample_bytree` hyperparameter.

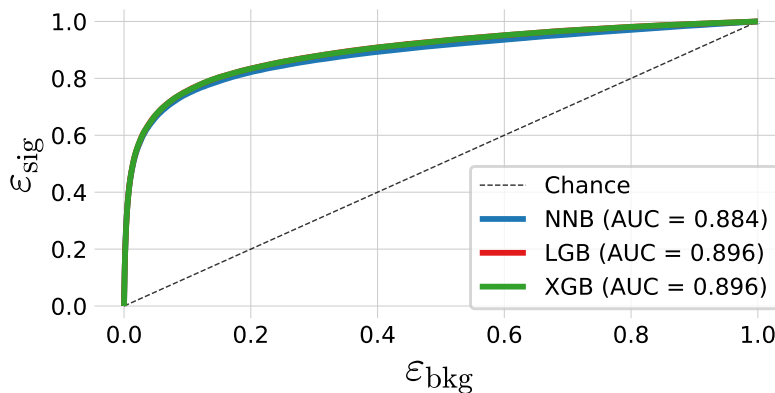
Figure 5.8: Hyperparameter optimization results of *b*-tagging for 4-jet events. The results are shown as parallel coordinates with each hyperparameter along the  $x$ -axis and the value of that parameter on the  $y$ -axis. Each line is an event in the 4-dimensional space colored according to the performance of that hyperparameter as measured by AUC. The single best hyperparameter is shown in red.

### 5.4.2 $b$ -Tagging Results

The prediction score  $\hat{y}$  is usually called the  $b$ -tag for  $b$ -tagging models and will be written as  $\beta_{\text{tag}}$ . The distribution of the  $b$ -tags for the two HPO-optimized models, LGB and XGB, together with the pre-trained neural network, NNB, can be seen in Figure 5.9 for 4-jet events and in B.4 for 3-jet events. Notice the strong match between the NNB and LGB models. The XGB model has almost no high  $b$ -tags ( $\beta_{\text{tag}} > 0.8$ ), but a majority of  $b$ -tags in the very low end. This indicates that the XGBoost has focussed on the background events compared to the signal events, whereas the NNB and LGB models have focused more on the signal events.



Even though the distributions of  $b$ -tags are different between the three models, the real performance plot for classification is the ROC curve seen in Figure 5.10 for 4-jet events. Here the signal efficiency  $\varepsilon_{\text{sig}}$  is plotted as a function of the background efficiency  $\varepsilon_{\text{bkg}}$  with the AUC shown in the bottom right corner. The LGB and XGB models performs similarly well with an AUC = 0.896 compared to the NNB with AUC = 0.884. The differences between the models are even smaller for 3-jet events seen in Figure B.5. In general the LGB and XGB models are so similar that they cannot be distinguished from another in any of the plots and their difference in AUC is on the fourth decimal point.



The LGB model is, however, several times faster than the XGB model. In comparison, 10 iterations of HPO using RS on 3-jet events with XGB took more almost 34 hours on HEP<sup>11</sup> compared to just 23 hours for 100 iterations for LGB. The same performance difference

Figure 5.9: Histogram of  $b$ -tag scores  $\beta_{\text{tag}}$  in 4-jet events for NNB (the neural network pre-trained by ALEPH, also called `nnbjet`) in blue, LGB in red, and XGB in green.

Figure 5.10: ROC curve of the three  $b$ -tag models in 4-jet events for NNB (the pre-trained neural network trained by ALEPH, also called `nnbjet`) in blue, LGB in red, and XGB in green. In the legend the area under curve (AUC) is also shown. Notice that the LGB and XGB models share performance and it is thus due to overplotting that only the green line for XGB can be seen.

<sup>11</sup> The local computing cluster.

was seen in 4-jet events where the timings were 4 hours for XGB compared to 2.5 hours for LGB. Since their performance is similar, XGB is dropped in the subsequent analysis.

The distribution of the  $b$ -tag scores  $\beta_{\text{tag}}$  for signal and background in 4-jet events can be seen in Figure 5.11. The separation between the heavier quarks and light quarks (and gluons) is clear at high values of  $\beta_{\text{tag}}$ , however, a lot of  $c$ -quarks also get a high  $b$ -tag score. The same is seen for 3-jet events in Figure B.6.

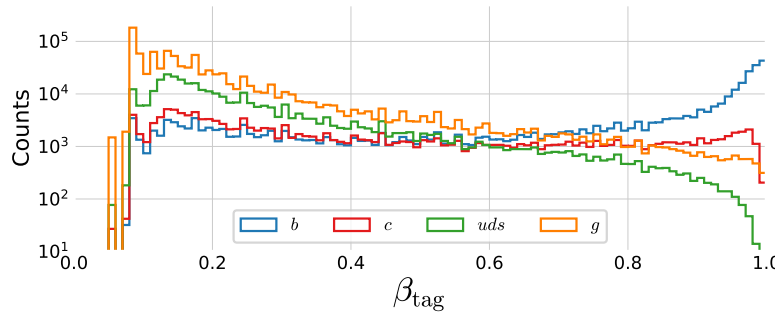


Figure 5.11: Distribution of  $b$ -tags in 4-jet events for  $b$ -jets in blue,  $c$ -jets in red,  $uds$  in green and  $g$  in orange.

#### 5.4.3 $b$ -Tagging Model Inspection

To get a better understanding of the trained LGB model, the global SHAP feature importances are shown in Figure 5.12 for 4-jet events. First of all it is noted that the `projet` has global feature importance of 57.32 %, `bqvjet` 29.16 %, and `ptljet` 13.52 %. For all three variables it is seen how most of the points have many small feature values which has a (small) negative impact on the model output. Especially the `ptljet` has many features with a low value (0 in fact) yet this does not pull the model too much towards background events. Compared this to a jet with a high value of `ptljet` which has a strong, positive impact on the output prediction.

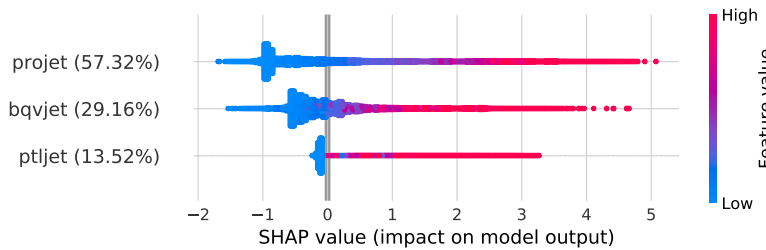


Figure 5.12: Global feature importances for the LGB  $b$ -tagging algorithm on 4-jet events. The normalized feature importance is shown in the parenthesis and each dot is an observation showing the dependance between the SHAP value and the feature value.

In regression, the model output is a continuous prediction  $\hat{y}_{\text{reg}} \in \mathbb{R}$ . In classification what is actually happening under the hood is that the model predicts a value  $\tilde{y} \in \mathbb{R}$  which is transformed to a number in the  $[0, 1]$ -interval via the *expit* function:

$$\text{expit}(\tilde{y}) = \frac{e^{\tilde{y}}}{1 + e^{\tilde{y}}} \equiv p, \quad (5.3)$$

where  $p$  is a number in the  $[0, 1]$ -interval. The expit function is also sometimes known as the logistic function and is visualized in Fig-

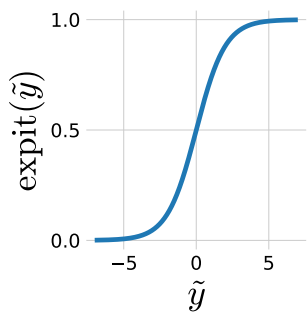


Figure 5.13: The expit function.

ure 5.13. Its inverse is the *logit* function:

$$\text{logit}(p) = \log\left(\frac{p}{1-p}\right) = \tilde{y}, \quad (5.4)$$

which is visualized in Figure 5.14. The fraction in equation (5.4) is called the *odds* and the logit-transformed value of  $p$ ,  $\text{logit}(p) = \tilde{y}$ , is thus sometimes called the *log-odds*. Because LightGBM makes its predictions in this log-odds space, the SHAP values in Figure 5.12 are also in log-odds space<sup>12</sup>.

With this in mind, single predictions of the LGB  $b$ -tagging model can be understood with SHAP which Figure 5.15 is an example of. This plot, which is my own extension to Figure 3.22, shows the logic behind the model's prediction for a particular jet in a particular 3-jet event. That the bias is negative reflects that there is a majority of background jets compared to signal jets<sup>13</sup>. This particular event has `projet` = 1.003, `bqvjet` = 0.529, and `ptljet` = 0. In the plot it is seen how this high value of `projet` has the greatest impact on the model prediction, while the medium value of `bqvjet` also pushes the model prediction towards a signal-prediction. The four red and green bars in the left part of the plot are all in log-odds space and their sum is shown as the blue bar to right, where the right  $y$ -axis shows the value in probability space  $p \in [0, 1]$ . This jet was in fact a  $b$ -jet.

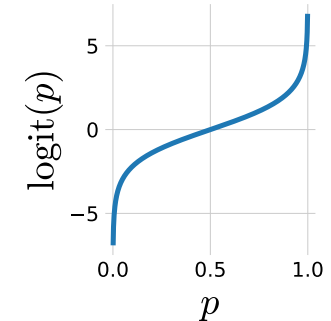
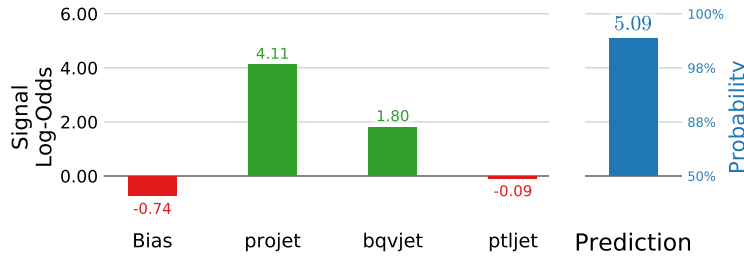


Figure 5.14: The logit function.

<sup>12</sup> The additivity property of SHAP, see section 2.8, is thus also in this log-odds space.

<sup>13</sup> Only around 22 % of all the jets are  $b$ -jets.

Figure 5.15: Model explanation for the 3-jet  $b$ -tagging LGB model for a  $b$ -like jet. The first column is the bias which can be seen as the naive prediction baseline, the rest are the input variables. On the right hand side of the plot is the model prediction shown. The left part of the plot is shown in log-odds space, the right part in probability space. The **negative** log-odd values are shown in red, **positive** ones in green, and the **prediction** value in blue.

## 5.5 $b$ -Tagging Efficiency

Before any further analysis can be done, the efficiency of the  $b$ -tagging model has to be measured. The efficiency  $\varepsilon$  is defined as the number of particles, events, jets, or any other countable measure,  $N_{\text{sel}}$ , that are selected by the algorithm divided by the *true* number,  $N_{\text{truth}}$ :

$$\varepsilon = \frac{N_{\text{sel}}}{N_{\text{truth}}}. \quad (5.5)$$

Of course, the truth is never known in Nature, however, it is for simulated MC events. The efficiency is used to estimate how many particles (e.g.) that were generated even though only a subset of the particles were detected. Imagine a hypothetical experiment where 21 particles were observed and the efficiency of the experiment was  $\varepsilon = 50\%$ . This means that there were created  $21/\varepsilon = 42$  particles in the experiment, yet only 21 of them were observed.

For measuring the  $b$ -tagging efficiency we apply a Tag-Tag-Probe (TTP) method based on the  $b$ -tags. In 3-jet events two of the jets will serve as tags and the last one as probe. The tags are jets where, if they are known, the probe is also known (with high probability). One can then apply the cut to the probe and see if it would have passed the cut or not. This method provides a clean and unbiased sample (the probes) and since (with high probability) the truth of the probe jet is known, the efficiency can be measured in this way [37]. Since the TTP method does not depend on real truth, it can be used on both MC and Data.

To measure the  $b$ -tagging efficiency we use that the  $Z$  decay has the form  $Z \rightarrow q\bar{q}g$ . Quantum field calculations based on the Standard Model predicts that the decay  $Z \rightarrow ggg$  is extremely unlikely with a branching ratio of  $\sim 10^{-6}$  [94]. This decay was actually tested at LEP which did not find any  $ggg$  events and concluded that the branching ratio was  $< 1.6\%$  with an upper limit at 95% confidence level [41]. This number is further reduced today to  $< 1.1\%$  [73].

That the  $Z$  decays to  $q\bar{q}g$  means that if one of the jets get a high  $b$ -tag (and is thus likely to be a  $b$ -jet), and another one of the jets gets a low  $b$ -tag (and is thus likely to be a  $g$ -jet), then it is highly probable that the remaining jet is a  $b$ -jet. To formalize this, sort the jets after their  $b$ -tags values from high to low such that  $\beta_{\text{tag}_1} > \beta_{\text{tag}_2} > \beta_{\text{tag}_3}$  for the jets  $\mathbf{J} = [J_1, J_2, J_3]$  where  $J_i$  has  $b$ -tag  $\beta_{\text{tag}_i}$ . We then define the two tags  $T_b$  and  $T_g$  as  $\mathbf{J} = [T_b, P, T_g]$  where  $P$  is the probe. If the two tags  $T_b$  and  $T_g$  passes the cuts  $\beta_{b\text{-cut}} < \beta_{\text{tag}_1}$  and  $\beta_{\text{tag}_3} < \beta_{g\text{-cut}}$ , then the probe is selected  $P = J_2$ . If the probe is selected, then the last cut  $\beta_{b\text{-cut}} < \beta_{\text{tag}_2}$  is the one that the efficiency is based on.

Based on Figure 5.11 we define the threshold for the  $b$ -jet tag to be  $\beta_{b\text{-cut}} = 0.9$  and for the  $g$ -jet to be  $\beta_{g\text{-cut}} = 0.4$ . The  $b$ -signal region is thus  $0.9 < \beta$  and the  $g$ -signal region  $\beta < 0.4$ . With these cuts, the efficiency, denoted  $\varepsilon_b^{b\text{-sig}}$ , of the  $b$ -jets being tagged as  $b$ -signal is computed. The TTP method is applied to both Data (Data TTP) and MC (MC TTP), along with a measurement of the efficiency when measured using MC truth (MC Truth) and a measurement based on the probes that were actual  $b$ -jets according to truth (MC Truth TTP)<sup>14</sup>. The efficiency is measured as a function of jet energy  $E_{\text{jet}}$  to gauge the energy dependence of the efficiency, i.e. computed in a bin-by-bin basis split according to the jet energy (of the probe).

The efficiencies can be seen in Figure 5.16. The efficiency  $\varepsilon_b^{b\text{-sig}}$  as a function of jet energy  $E_{\text{jet}}$  can be seen on the left  $y$ -axis, whereas the number of probes in each bin  $N_{\text{truth}}$  can be seen on the right  $y$ -axis. The efficiencies increase as a function of energy and reaches a plateau at  $E_{\text{jet}} \sim 30 \text{ GeV}$ : high-energy  $b$ -jets are easier to classify than low-energy ones. Even though the efficiencies of the MC TTP and Data TTP methods are lower than the MC Truth and MC Truth TTP, the important thing to notice is that they follow each other closely, an indicator of the trained  $b$ -tagging model working equally well on both MC and Data (as hoped).

The efficiency of  $g$ -jets in the  $g$ -jet signal region  $\varepsilon_g^{g\text{-sig}}$  based on the

<sup>14</sup> So the probes are selected by the TTP method, however, only true  $b$ -jet probes are kept.

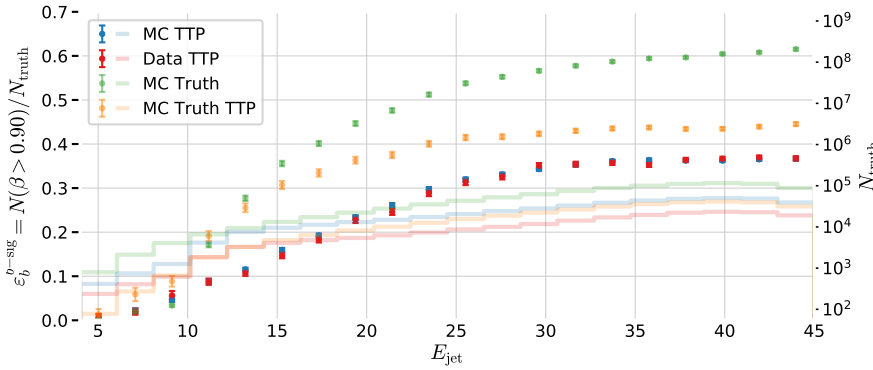


Figure 5.16:  $b$ -tag efficiency for  $b$ -jets in the  $b$ -signal region for 3-jet events,  $\varepsilon_b^{b\text{-sig}}$ , as a function of jet energy  $E_{\text{jet}}$ . In the plot the efficiencies are shown for MC TTP in blue, Data TTP in red, MC Truth TTP in green, and MC Truth in orange. The efficiencies (the errorbars) can be read off on the left  $y$ -axis and the counts (histograms) on the right  $y$ -axis. Notice how both MC TTP and Data TTP follow each other closely.

$b$ -tags can be measured in a similar manner. Again TTP method is used, however, now the two  $b$ -jets are the tags and the  $g$ -jet is the probe. The cuts are the same as before, however, now it is required that  $0.9 < \beta_{\text{tag}_1}$  and  $0.9 < \beta_{\text{tag}_2}$  before the probe is selected  $P = J_3$ . The efficiency is then based on  $\beta_{\text{tag}_3} < 0.4 = \beta_{g\text{-cut}}$ . The efficiency  $\varepsilon_g^{g\text{-sig}}$  is plotted in Figure 5.17. Here the MC TTP and Data TTP also follow each other closely, this time to around  $\sim 25$  GeV.

Both of the efficiencies so far,  $\varepsilon_b^{b\text{-sig}}$  and  $\varepsilon_g^{g\text{-sig}}$ , can be seen as signal efficiencies. Likewise, there are two background efficiencies, one for  $b$ -jets in the  $g$ -signal region  $\varepsilon_b^{g\text{-sig}}$  seen in Figure B.20 and one for  $g$ -jets in the  $b$ -signal region  $\varepsilon_g^{b\text{-sig}}$  seen in Figure B.21.

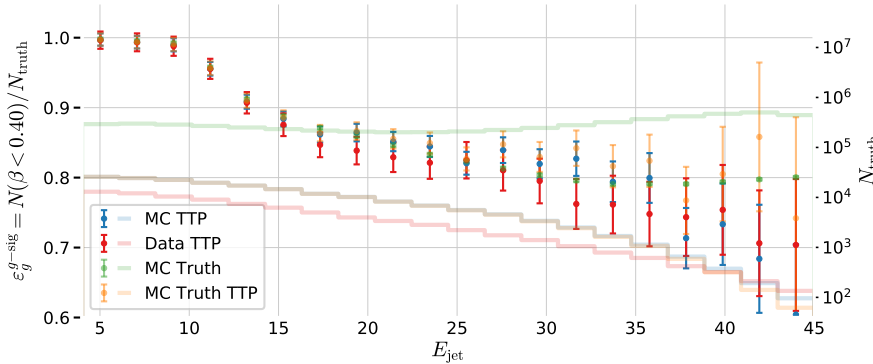


Figure 5.17:  $b$ -tag efficiency for  $g$ -jets in the  $g$ -signal region for 3-jet events,  $\varepsilon_g^{g\text{-sig}}$ , as a function of jet energy  $E_{\text{jet}}$ . In the plot the efficiencies are shown for MC TTP in blue, Data TTP in red, MC Truth TTP in green, and MC Truth in orange. The efficiencies (the errorbars) can be read off on the left  $y$ -axis and the counts (histograms) on the right  $y$ -axis. Notice how both MC TTP and Data TTP follow each other closely until  $\sim 25$  GeV.

This section shows that the  $b$ -tagging efficiencies of the LGB  $b$ -tagging model shows comparable performance on both MC and Data which indicates that the model is un-biased (w.r.t. energy).

## 5.6 $g$ -Tagging Analysis

The  $b$ -tagging model is a jet-based model which provides a  $b$ -tag score  $\beta_{\text{tag}}$  to a jet. This also means that each of the jets in e.g. a 4-jet event can get a  $b$ -tag:  $\beta_{\text{tag}} = [\beta_{\text{tag}_1}, \beta_{\text{tag}_2}, \beta_{\text{tag}_3}, \beta_{\text{tag}_4}]$ . Treating  $\beta_{\text{tag}}$  as an individual observation, one can train a new model on the events based on the events compared to the individual jets. This event-based process will be called  $g$ -tagging and the trained model will return a  $g$ -tag score written as  $\gamma_{\text{tag}}$ .

For this model, signal events are defined to be events which are  $q$ -matched<sup>15</sup> and where the two jets with the highest  $b$ -tags are matched to the two (final) quark jets. Another way to say this, is that the non- $q$ -matched jets are assigned the  $n - 2$  lowest  $b$ -tag scores for  $n$ -jet events. An example of a signal event is  $\beta_{\text{tag}} = [0.95, 0.89, 0.15, 0.07]$  for an event with the four jets  $[b, \bar{b}, g, g]$ . Compared to the  $b$ -tagging model, this model will allow one to extract entire events which contains a clear identification of gluons versus non-gluons.

### 5.6.1 Permutation Invariance

Since the  $b$ -tags are only based on the vertex variables, the goal of the  $g$ -tag is to also be constructed in an un-biased way with respect to the jet energy  $E_{\text{jet}}$ . However, even though  $\beta_{\text{tag}}$  is independent of  $E_{\text{jet}}$  and  $\gamma_{\text{tag}}$  is a function of  $\beta_{\text{tag}}$ , it turned out that  $\gamma_{\text{tag}}$  was not independent of  $E_{\text{jet}}$ . This was because the ordering of the jets within the event was energy-dependent: they are sorted according to their  $E_{\text{jet}}$ .

This meant that the different variables ( $b$ -tags) in  $\beta_{\text{tag}}$  had different feature importances when tested, even though they should be equally important. Instead of defining  $\beta_{\text{tag}}$  as a vector it should instead be seen as a set<sup>16</sup>  $\beta_{\text{tag}} \equiv \{\beta_{\text{tag}_1}, \dots, \beta_{\text{tag}_n}\}$ . The  $g$ -tagging model trained on the events should thus be *permutation invariant*<sup>17</sup> with regards to the input variables. The category of permutation invariant (and equivariant<sup>18</sup>) neural networks has seen an huge development within recent years in the deep learning community. The paper from Zaheer et al. [103] in 2017 was highly influential, however also other examples exists [78, 52]. Yet, the same development cannot be said to have happened within the more classic machine learning field.

Although not being a novel software-technical solution, I circumvent the problem with two simple different approaches: 1) by simply shuffling the inputs variables independently for each observation (row) in the dataset, and 2) training on all possible permutations of the variables in the dataset. The second approach can be seen as a feature augmentation technique where the data is artificially increased with factor of  $n$  factorial:  $N \rightarrow n! \cdot N$  where  $N$  is the number of events and  $n \in \{3, 4\}$  is the number of jets. These two methods were tested along with keeping the original order of the dataset.

### 5.6.2 Truncated Uniform PDF

Initially when plotting the HPO performance as a function of iteration, it was seen how there were some very clear plateaus, where the highest plateau (i.e. the highest AUC value and thus the best score) was only seen in the very first iteration. It was quickly realized that this was due to the very first iteration was being run with the default values of the LGB in my HPO setup. However, what was not understood was why this value was performing so much better than the different sets of hyperparameters in the random search. Of

<sup>15</sup> Remember that  $q$ -matched events are events with one, and only one, jet that is  $q$ -matched to one of the quark-jets, and one, and only one of the jets is  $q$ -matched to the other quark-jet.

<sup>16</sup> Since sets have no inherent order.

<sup>17</sup>  $f(\mathbf{x}) = f(\tau(\mathbf{x}))$  for any permutation  $\tau$  on an input vector  $\mathbf{x}$ .

<sup>18</sup>  $\tau(f(\mathbf{x})) = f(\tau(\mathbf{x}))$  for any permutation  $\tau$  on an input vector  $\mathbf{x}$ .

course LightGBM have chosen their default parameters wisely, however, one would not expect them to outperform other sets of hyperparameters that clearly. During the debugging process the column downsampling `colsample_bytree` was diagnosed to be the culprit. The default value is `colsample_bytree = 1`, however, the probability density function (PDF) used in random search for this parameter was  $\mathcal{U}(0.4, 1)$  which was expected to give the same performance as the default value, at least for values of `colsample_bytree` close to 1. By inspecting the source code of LightGBM, I realized that if the column downsampling is less than 1 the model takes the integer of the column downsampling multiplied with the total number of columns (variables/features) [6]. This means that no matter how close to 1 the column downsampling get, the integer value of the total number of columns get floored to maximally 2 in 3-jet events, compared to when the column downsampling is exactly 1 (which it only is for the default values).

To deal with this problem I developed a new PDF<sup>19</sup> on top of the existing ones in Scipy: the truncated uniform PDF  $\mathcal{U}_{\text{trunc}}(a, b, c)$ . This PDF first generates a random number  $x$  from a uniform distribution between  $a$  and  $c$ . Then, if  $x$  is larger than  $b$  it is floored to  $b$ . In this way, it is possible to both get values of  $x$  in the interval  $[a, b]$  but also values exactly equal to  $b$ . The value of  $c$  controls how often these “overflow” values of  $x$  are generated.

<sup>19</sup> Not strictly a PDF since it is not normalized, but otherwise behaves as one.

### 5.6.3 *g*-Tagging Hyperparameter Optimization

Four LightGBM models<sup>20</sup>, two for 3-jet events and two for 4-jet events, were trained and hyperparameter optimized for both the energy ordered and shuffled data sets with 100 iterations of random search. The same PDFs as for the *b*-tagging were used, see Table 5.4, and 5-fold cross validation and early stopping was applied with a patience of 100.

The results of the HPO can be seen in Figure 5.18. Here the two 3-jets models are seen in the two plots to the left, and the two 4-jets to the right. The very left plot shows the performance as a function of iteration number for the 3-jet energy-ordered method (no permutation or shuffling). This was where the issues mentioned in subsection 5.6.2 were first discovered. There are three very noticeable plateaus in this plot which corresponds to running column subsampling with zero, one, or two variables dropped. The three plateaus are also seen in the 3-jet events that were shuffled, however, with more variation in each plateau (along with a drop in performance). For the 4-jet events the plateaus are not as apparent but it can still be seen how some of the iteration show a significantly lower score than others. The parallel coordinate plots for the four plots can be seen in Figure B.8–B.11.

The global SHAP feature importances  $\phi_{\beta_i}^{\text{tot}}$  are computed for each one of the three methods, energy-ordered, shuffled, or with all permutations, to verify their permutation invariance properties. The

<sup>20</sup> The method with all permutations was trained using the same hyperparameters as the best ones found in the HPO for the shuffled model to reduce time spent on HPO. The time performance is extra important for the method with all permutations as the dataset is 24 times larger the method with the shuffling for 4-jet events.

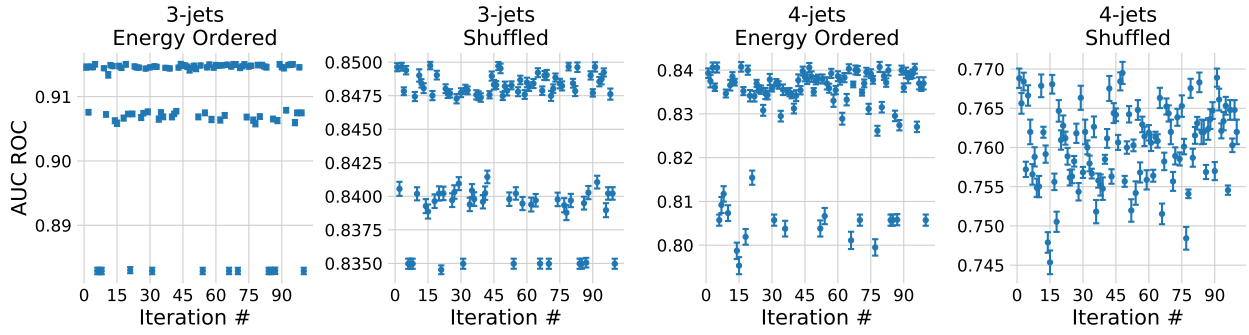


Figure 5.18: Hyperparameter Optimization results of  $g$ -tagging with 100 iterations of random search with LGB. From left to right, we have A) 3-jet events energy-ordered (no permutations), B) 3-jet events row-shuffled, C) 4-jet events energy-ordered, D) 4-jet events row-shuffled. Notice the different ranges on the y-axes.

results are seen in Table 5.5 for 4-jet events and in Table B.3 for 3-jet events. Here it can be seen that the model trained on the energy ordered data learned to attribute the highest weight to the first  $b$ -tag, second highest weight to the second  $b$ -tag, and so on. In contrary, the weights are uniformly distributed between the different  $b$ -tags in both the shuffled and all-permuted datasets (within a few sigma). The same overall pattern is seen for the 3-jet events. Based on the tables, it can be seen that both the shuffling method and all-permuting method are methods for training ML models with permutation invariant properties due to their approximately equal attribution of weight to the different variables ( $b$ -tags).

$\beta_{\text{tag}_i}$	Energy Ordered	Shuffled	All Permutations
$i = 1$	$0.986 \pm 0.008$	$0.474 \pm 0.005$	$0.465 \pm 0.005$
$i = 2$	$0.609 \pm 0.006$	$0.467 \pm 0.005$	$0.464 \pm 0.005$
$i = 3$	$0.424 \pm 0.004$	$0.461 \pm 0.005$	$0.452 \pm 0.005$
$i = 4$	$0.244 \pm 0.002$	$0.481 \pm 0.005$	$0.466 \pm 0.005$

Table 5.5: Global SHAP feature importances  $\phi_{\beta_i}^{\text{tot}}$  for the three  $g$ -tagging models in 4-jet events. Each  $\phi_{\beta_i}^{\text{tot}}$  is shown for the three methods in the columns and the four  $b$ -tags as variables in the rows.

#### 5.6.4 PermNet

In addition to the LGB models, a permutation invariant neural network called PermNet based on the Deep Sets paper [103] implemented in Tensorflow [10] by Faye [47] was also tested. Zaheer et al. [103] showed that  $f(X)$  is permutation invariant if and only if it can be decomposed in the following way:

$$f(X) = \rho \left( \sum_{x \in X} \phi(x) \right). \quad (5.6)$$

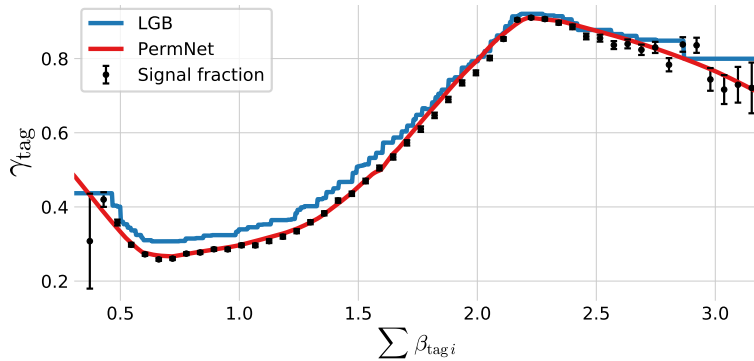
for suitable transformations  $\rho$  and  $\phi$  (which the neural network learns<sup>21</sup>). The PermNet was trained using three layers<sup>22</sup> with leaky ReLU [69] as the activation function and ADAM [62] as the optimizer optimizing the log-loss. The network was trained with early stopping with a patience of 50 epochs and a batch size of 128. A visual overview of the PermNet architecture can be seen in Figure B.12. It took around 6 hours to fit the 3-jet events and 4.5 hours for the 4-jets (due to fewer events) for each of the models.

<sup>21</sup> This is possible since neural networks are universal function approximators [56].

<sup>22</sup> Where the two hidden layers have 128 and 64 neurons in each.

### 5.6.5 1D Comparison of LGB and PermNet

I made a small study to better understand the LGB and (especially) the PermNet models. This comparison was constructed by summing the  $b$ -tag scores in the  $n$ -jet event together  $\sum_i^n \beta_{\text{tag}_i}$ . The  $\beta_{\text{tag}_i}$  are summed together since this turns the problem into a 1D problem that is easy to visualize, the sum of numbers is a permutation invariant function. The sum also corresponds to the simplest functions of  $\rho$  and  $\phi$  in equation (5.6): the identity function. Both 1D models are fit to the training events. After the fits, a linear scan from  $\sum_i^n \beta_{\text{tag}_i} = 0.4$  to 3.1 is made to see how the predicted  $g$ -tags distribute. This is shown in Figure 5.19 for 4-jet events. Here the value of  $\gamma_{\text{tag}}$  is shown for the two models together with the fraction of signal to background in each bin. If the  $g$ -tag score should resemble a true probability it would be expected to follow the signal ratio, e.g. a model should predict  $\gamma_{\text{tag}} = 0.9$  if there is 90 % signal in that bin. In the figure it is seen how the PermNet does a great job at fitting the signal fraction and the LGB model also does a decent job. Remember that none of these models were shown the signal fraction explicitly, only the  $b$ -tag sum and a truth label. The distribution of signal and background<sup>23</sup> together with the distribution of cuts made by the LGB model can be seen in Figure B.13. The similar plots for 3-jet events are plotted in Figure B.14 and B.15.



<sup>23</sup> Which the signal fraction is based on.

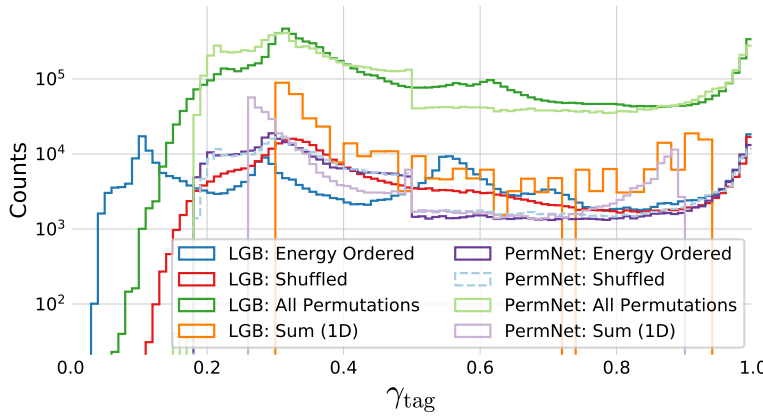
Figure 5.19: Plot of the (1D)  $g$ -tag scores for 4-jet events as a function of  $\sum \beta_i$  for the LGB model in blue and the PermNet model in red. The signal fraction (based on the signal and background histograms in Figure B.13) is plotted as black error bars where the size of the error bars is based on the propagated uncertainties of the signal and background histogram assuming Poissonian statistics.

It can be concluded, at least in 1D, that both LGB and PermNet are able to capture the inherent structure in the 1D

### 5.6.6 $g$ -Tagging Results

The distribution of  $g$ -tag scores in 4-jet (training) events can be seen in Figure 5.20 for the eight combinations of the two models (LGB and PermNet) and the four data sorting methods (energy ordered, (row) shuffled, all permutations, and the 1D sum.). At first the increased number of events (a factor of 24 for 4-jet events) with the all-permutation scheme is seen separating the two light green curves from the rest. The energy ordered LGB model is the combination which utilizes most of the  $\gamma_{\text{tag}}$ -range, while the two 1D sum models have the most limited range, indicating that the models are more uncertain about their predictions. The energy ordered and

shuffled PermNet models can more or less only be distinguished because the latter is plotted with dashed lines. This makes sense, since they are also expected to make the same predictions were they really permutation invariant<sup>24</sup>. When plotted with normalized counts it is seen how the shuffled and all-permuted LGB models also follow each other very closely, which can still be partly seen in this plot by comparing the two distributions. The distribution of  $g$ -tags in 3-jet training events can be seen in Figure B.16.



The ROC curve in Figure 5.21 shows the performance of the different models on 4-jet events with the AUC shown in the legend. First of all it is easy to see that the energy ordered LGB model is significantly higher-performing than the rest of the models, however, this model is also energy-biased (not permutation invariant in the  $b$ -tags) and is only included to see how large a performance drop the permutation invariance criterion causes. The worst performing models are the two 1D sum models since they only have a single dimension to learn from, compared to the four dimensions that the other models have. Overall it can be seen that the rest of the models are performing almost identically, with the LGB model trained on all permutations to be the highest-performing of them all by a small margin. For 3-jet events a similar picture is seen, see Figure B.18, however, here the LGB model trained on the shuffled events performs the best, yet this performance improvement is so small compared to the all-permutations LGB model that it is expected to be due to statistical fluctuations and not a real performance difference.

Based on the AUC scores seen in the ROC curves in Figure 5.21 and B.18, the LGB-model trained on all permutations will be the  $g$ -tagging model choice. To see how this model's predictions of the  $g$ -tags distribute for signal and background events, see Figure 5.22. Here the distribution of  $\gamma_{\text{tag}}$  is shown for 4-jet signal events and background events. Remember that in  $g$ -tagging, the signal events are defined as events where the two jets with the highest  $b$ -tags are also the two  $q$ -matched jets (and the entire event is  $q$ -matched). In the figure it can be seen that at high values of  $\gamma_{\text{tag}}$  primarily  $b\bar{b}gg$  events (signal  $b$ ) are tagged where the jets are sorted according to their  $b$ -tags. Next after signal  $b$  events is  $c\bar{c}gg$  (signal  $c$ ) and  $bg\bar{b}g$ -events<sup>25</sup> (background

<sup>24</sup> It is only because of the stochasticity in the optimization process of the two networks that they did not converge to exactly the same predictions.

Figure 5.20: Distribution of  $g$ -tag scores in 4-jet events shown with a logarithmic  $y$ -scale for LGB: Energy Ordered in blue, LGB: Shuffled in red, LGB: All Permutations in green, LGB: Sum 1D in orange, PermNet: Energy Ordered in purple, PermNet: Shuffled in light-blue, PermNet: All Permutations in light-green, PermNet: Sum 1D in light-purple. Here LGB and PermNet are the two different type of models and “Energy Ordered”, “Shuffled”, “All Permutations”, and “Sum 1D” are the different methods used for making the input data permutation invariant (except energy ordered).

<sup>25</sup> Or any other permutation of  $b, \bar{b}, g, g$  which is not  $b\bar{b}gg$ .

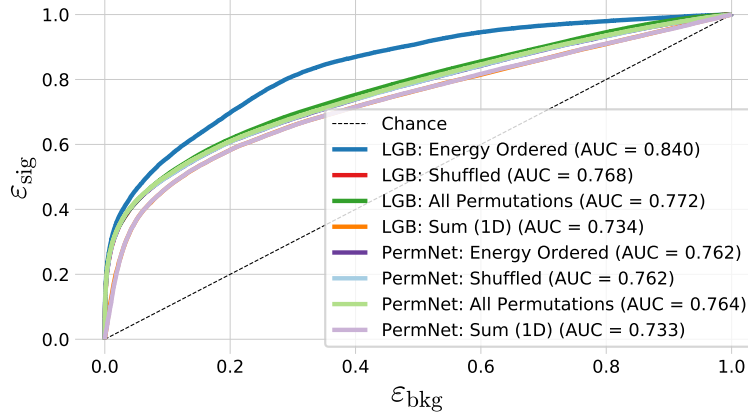


Figure 5.21: ROC curve of the eight g-tag models in 4-jet. First one in dashed black is the ROC curve that you get by random chance. The colors are the same as in Figure 5.20 and in the legend also the Area Under the ROC curve (AUC) is shown.

b). At low values of  $\gamma_{\text{tag}}$  light quarks ( $uds$ ) dominate.

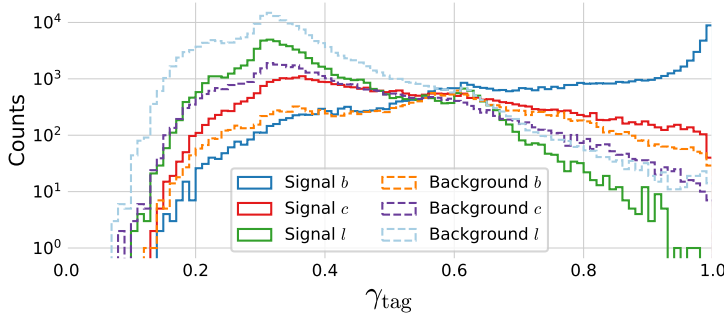


Figure 5.22: Histogram of  $g$ -tag scores from the LGB-model in 4-jet events for  $b$  signal in blue,  $c$  signal in red,  $l$  ( $uds$ ) signal in green,  $b$  background in orange,  $c$  background in purple,  $l$  ( $uds$ ) background in light-blue.

The similar plot for 3-jet events is seen in Figure B.19. This plot has some surprising bumps for mainly  $l$ -quark events. When comparing  $l$ -quark events in the high- $\gamma_{\text{tag}}$  bump with the ones getting a low  $\gamma_{\text{tag}}$ -value, see Figure 5.23, one can see that  $l$ -quark events with high  $\gamma_{\text{tag}}$  has only two jets with high  $b$ -tags, compared to low- $\gamma_{\text{tag}}$   $l$ -quark events which more often has three jets with high  $b$ -tags.

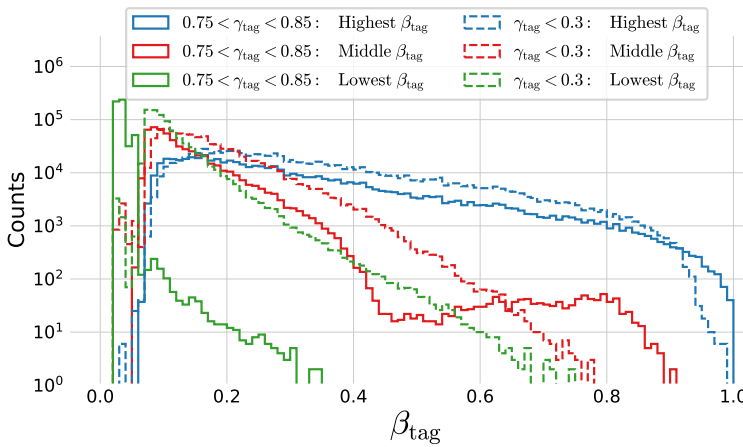
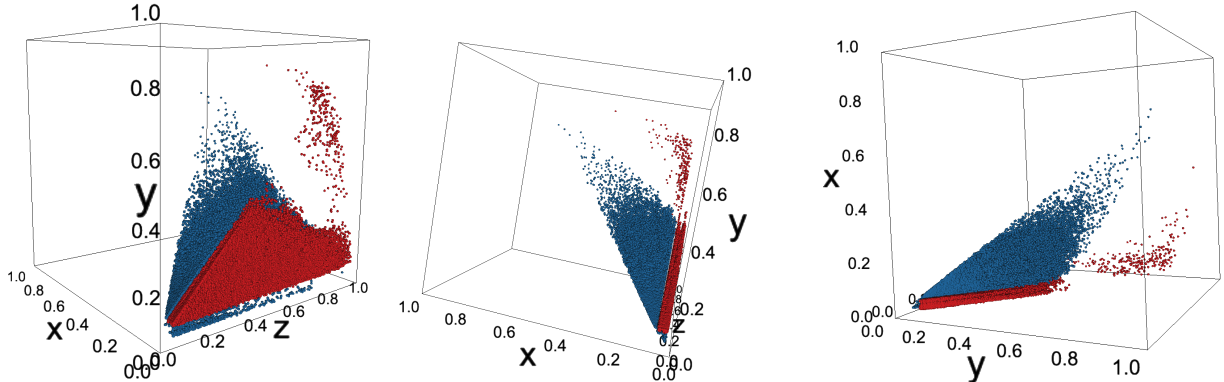


Figure 5.23: Distribution of  $b$ -Tag Scores in 3-Jet  $l$ -Quark Events for low and high  $g$ -tags values. Here  $l$ -quark events with  $0.75 < \gamma_{\text{tag}} < 0.85$ , so the high peak in Figure B.19, are plotted in fully connected lines, and events with  $\gamma_{\text{tag}} < 0.3$  are plotted in dashed lines. For each of these two selection of events the value of the jet with the **highest  $\beta_{\text{tag}}$**  is shown in blue, the jet with the **middle  $\beta_{\text{tag}}$**  in red, and the jet with the **lowest  $\beta_{\text{tag}}$**  in green.

This is even more visible once seen in a 3D scatter plot with the lowest  $\beta_{\text{tag}}$  on the  $x$ -axis, the middle on the  $y$ -axis, and highest on the  $z$ -axis. Three small views from the 3D visualization can be seen in Figure 5.24. Here it is easily seen how the separating variable is the lowest  $b$ -tag: if an event where all three jets have high  $b$ -tags are

used as input to the  $g$ -tagging model it gives it a low  $g$ -tag compared to if only two of the three jets have high  $b$ -tags.



## 5.7 $g$ -Tagging Efficiency

These efficiencies are only possible to measure for MC-generated data as the truth labels are required. The Tag-Tag-Probe (TTP) method in section 5.5 is not possible for whole events as every event is completely independent of the other and thus one event cannot work as a tag for another event. We can, however, construct a pseudo  $g$ -tagging efficiency based on the  $b$ -tagging efficiencies. This efficiency will be computed by looking at 3-jet events with two jets with a high  $b$ -tag and one jet with a low  $b$ -tag, i.e. events where two jets has  $0.9 < \beta_{\text{tag}}$  and one jet has  $\beta_{\text{tag}} < 0.4$ . This indicates a  $b\bar{b}g$  event where all of the jets have been correctly identified by the  $b$ -tagging algorithm. The pseudo efficiency  $\epsilon_{b\bar{b}g}$  is then defined as:

$$\epsilon_{b\bar{b}g} = \epsilon_b^{\text{b-sig}}(b) \cdot \epsilon_b^{\text{b-sig}}(\bar{b}) \cdot \epsilon_g^{\text{g-sig}}(g). \quad (5.7)$$

This is only a pseudo efficiency since this number is based on the jets in the event and not the event itself, however, by plotting it as a function of an event variable and comparing MC to Data, we can gauge the validity of the  $g$ -tagging algorithm. The first of the event variables used is the  $g$ -tag of the event  $\gamma_{\text{tag}}$ , see Figure 5.25. Here the pseudo efficiency is plotted as a function of  $\gamma_{\text{tag}}$  for Data and MC together with the counts in each bin and the ratio between  $\epsilon_{b\bar{b}g}$  for Data and MC is plotted below. At low values of  $\gamma_{\text{tag}}$  the uncertainties dominate due to low statistics, however, at higher  $\gamma_{\text{tag}}$   $\epsilon_{b\bar{b}g}$  plateaus until very high values of  $\gamma_{\text{tag}}$  where it increases again. The important thing to note in this figure is the high agreement between Data and MC which converges to (almost) 1 at high  $\gamma_{\text{tag}}$ -values. This is an important indication of the 3-jet  $g$ -tagging model working.

Another event variable to look at is the mean of the two invariant masses<sup>26</sup>  $m_{bg}$  and  $m_{\bar{b}g}$ . The invariant mass between two quantities<sup>27</sup> is:

$$m_{12} = \sqrt{(E_1 + E_2)^2 - \|\mathbf{p}_1 + \mathbf{p}_2\|^2}, \quad (5.8)$$

Figure 5.24: 3D scatter plot of  $\beta_{\text{tag}}$ -values for high and low  $\gamma_{\text{tag}}$   $l$ -quark events. Here the  $x$ -axis is the lowest  $b$ -tag, the  $y$ -axis the middle, and the  $z$ -axis the highest. Here the **high- $\gamma_{\text{tag}}$   $l$ -quark events** are plotted in red and the **low ones** in blue.

<sup>26</sup> The invariant masses between all three jets  $m_{b\bar{b}g}$ , which otherwise might have been the first intuition to use as the event variable, is non-informative (in this context) since this is just the total event energy which is kept (approximately) constant at  $\sim 91$  GeV.

<sup>27</sup> When measured in natural units.

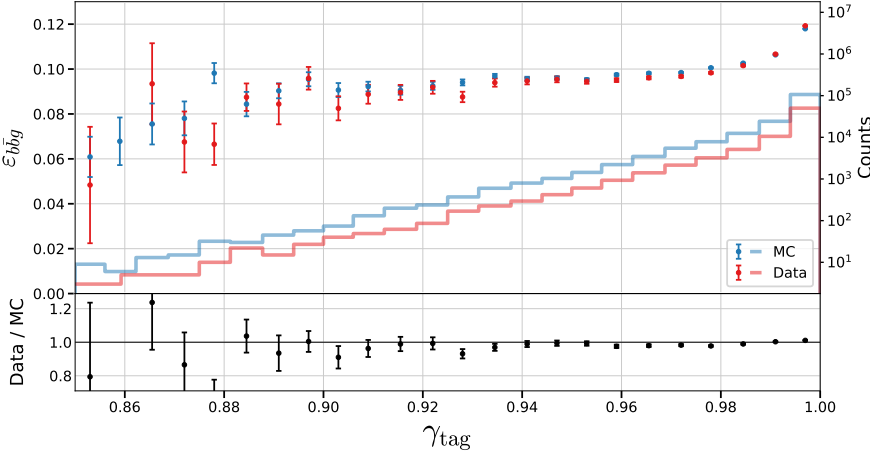


Figure 5.25: Pseudo efficiency of the g-tags for  $b\bar{b}g$  3-jet events as a function of the event's g-tag  $\gamma_{\text{tag}}$ . In the top plot the pseudo efficiency  $\varepsilon_{b\bar{b}g}$  is shown for MC in blue and Data in red where the counts in each bin can be read on right y-axis. In the bottom plot the ratio between Data and MC is shown. The pseudo efficiency is measured by finding  $b\bar{b}g$ -events where  $\beta_b > 0.9$ ,  $\beta_{\bar{b}} > 0.9$ , and  $\beta_g < 0.4$ . and then calculating  $\varepsilon_{b\bar{b}g} = \varepsilon_b^{b\text{-sig}} \cdot \varepsilon_{\bar{b}}^{b\text{-sig}} \cdot \varepsilon_g^{g\text{-sig}}$ .

where  $E_i$  is the energy of the  $i^{\text{th}}$  quantity and  $\mathbf{p}_i$  its momentum. The pseudo efficiency is plotted as a function of the mean of  $m_{bg}$  and  $m_{\bar{b}g}$  in Figure 5.26. Here the overall correspondence between Data and MC is lower than in Figure 5.25, especially for high values of the mean invariant mass. That the ratio is close to 1 for most of the data (from 20 GeV to 50 GeV) is a good sign, whereas the tails indicate the model is biased here which could be corrected for with correction factors, however, this would increase the systematic uncertainties.

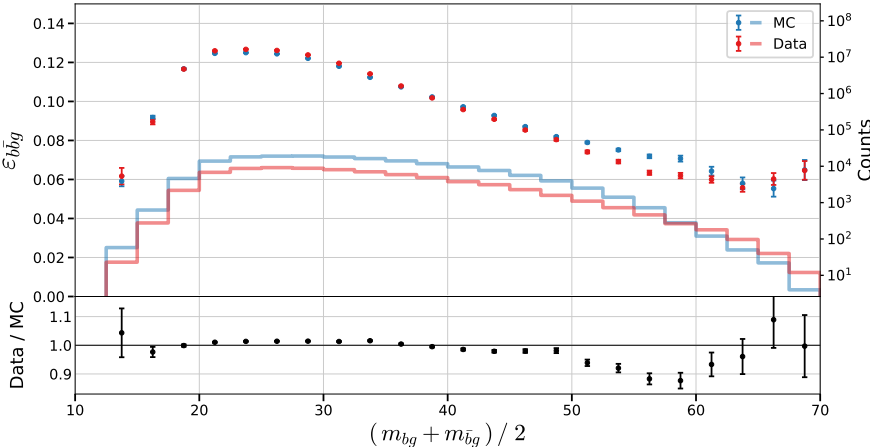


Figure 5.26: Pseudo efficiency of the g-tags for  $b\bar{b}g$  3-jet events as a function of the mean of the two invariant masses  $m_{bg}$  and  $m_{\bar{b}g}$  in the event. In the top plot the pseudo efficiency  $\varepsilon_{b\bar{b}g}$  is shown for MC in blue and Data in red where the counts in each bin can be read on right y-axis. In the bottom plot the ratio between Data and MC is shown.

These two figures strengthens the claim that the trained  $b$ -tagging and  $g$ -tagging models provide un-biased models that not only work in Data but also in MC.

## 5.8 Generalized Angularities in 3-jet events

To measure how gluon jet hadronizes, i.e. their jet distributions, number of tracks, etc., the *generalized angularities* provide an overall framework for doing so. The generalized angularities is a two-parameter family of variables depending on the angular weighting

$\beta \leq 0$  and an energy weighting factor  $\kappa \leq 0$ :

$$\lambda_{\beta}^{\kappa} = \sum_{i \in \text{jet}} z_i^{\kappa} \theta_i^{\beta}, \quad (5.9)$$

where  $z_i \equiv E_i / E_{\text{jet}}$  is the momentum fraction, i.e.  $0 \leq z_i \leq 1$ ,  $\theta_i \equiv \Omega_i / R$  is the normalized angle with respect to the jet axis where  $R$  is the jet radius such that  $0 \leq \theta_i \leq 1$ , and  $i$  runs over all the jet constituents [51, 64]. Different values of  $(\beta, \kappa)$  probe different parts of the (gluon) jet fragmentation phase space. I will limit the analysis to the five sets of  $(\beta, \kappa)$ -values shown in Figure 5.27, where each of the sets of variables are related to the following aspects:

$(\beta, \kappa)$

$(0, 0)$ : Hadron Multiplicity.

$(0, 2)$ : Transverse Momentum Distribution  $p_T^D$ :

$$\lambda_0^2 = \sum z_i^2 \equiv (p_T^D)^2 [38].$$

$(\frac{1}{2}, 1)$ : Les Houches Angularity (LHA) [89].

$(1, 1)$ : Width or broadening [35].

$(2, 1)$ : Mass.

We will look at the generalized angularity distributions for gluons in 3-jet events. We do so by using the  $g$ -tag from the  $g$ -tagging model to select events with a high  $g$ -tag and then select the jet in the event with the lowest of the  $b$ -tags since this jet is expected to be the gluon jet. From the plot in Figure B.19, the  $\gamma_{\text{tag}}$  cut off threshold is set to  $\gamma_{\text{cutoff}} = 0.9$  for 3-jet events. This cut corresponds to selecting 340 476 events in MC as gluon events with a signal efficiency of  $\varepsilon_g^{3\text{-jet}} = 19.68\%$  and a signal purity of  $\rho_g^{3\text{-jet}} = 98.77\%$ . Here a gluon event is defined as an event with a  $0.9 < \gamma_{\text{tag}}$ .

The distribution of  $\lambda_0^2$ , i.e.  $(\beta, \kappa) = (0, 2)$ , related to the transverse momentum distribution, in gluon events is seen in Figure 5.28. Here the distribution of  $\lambda_0^2$  is shown for MC Truth (actual gluons jets using truth-label), MC Selected (gluons jets selected using the  $g$ -tag) and Data (gluons jets selected using the  $g$ -tag). The generalized angularities are computed for both charged jets and neutral clusters, where this figure shows the distribution of  $\lambda_0^2$  for charged jets. The MC Selected has been scaled to Data according to the fraction of the number of events in each:  $w_{\text{MC}} = N_{\text{Data}} / N_{\text{MC}}$ . The MC Truth has been scaled with the same weight multiplied with the gluon efficiency  $w_{\text{MC-Truth}} = w_{\text{MC}} \cdot \varepsilon_g^{3\text{-jet}}$ . The  $\lambda_{\beta}^{\kappa} = 0$  values has been removed before plotting for all sets of values of  $(\beta, \kappa)$ .

In Figure 5.28 it is seen how MC Truth and Data does not match perfectly well which indicates that this is not the perfect method, however, that MC Selected and Data distributions matches each other quite well indicates that the model is equally biased for both MC and Data.

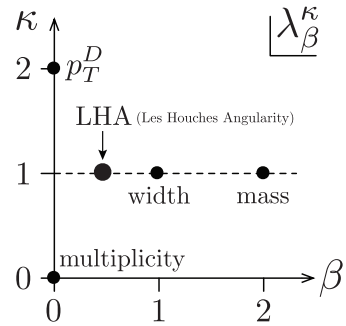


Figure 5.27: Generalized angularities. Adapted from Larkoski et al. [64].

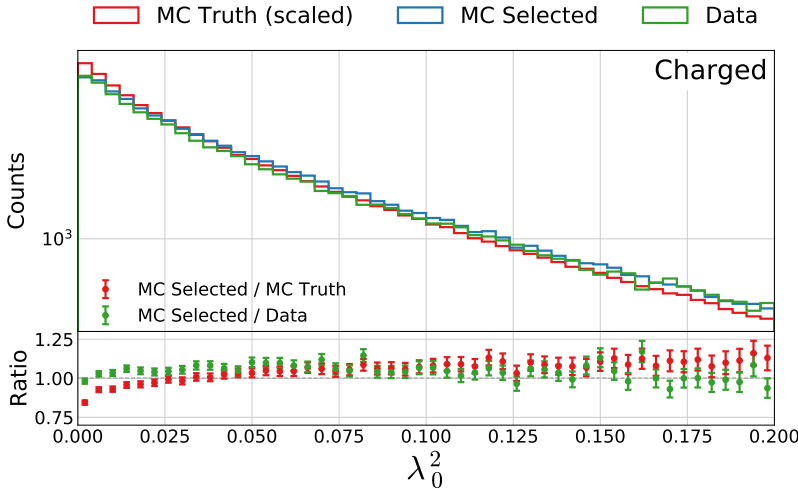


Figure 5.28: Distribution of the generalized angularity  $\lambda_0^2$  for charged gluons jets in 3-jet events:  $\lambda_0^2$ . The distributions for **MC Truth** is shown in red, **MC Selected** in blue, and **Data** in green in the top plot and in the bottom plot the ratio between **MC Selected** and **MC Truth** is shown in red and between **MC Selected** and **Data** in green.

The rest of the plots can be seen in Figure B.22–B.31. For the charged tracks it can be seen that the first few bins generally has ratios just below 1 with a upwards trend until around the middle of the  $\lambda$  range and then it decreases again (and the uncertainties increases with lower and lower statistics). The discrepancy between MC selected and Data is larger for the neutral clusters, which are also less well-defined than the charged jets (at the energies used at LEP), and with the same trend as for the charged jets. In general the figures show a resonable good correspondence between MC selected and Data for the generalized angularities.

## 5.9 Gluon splitting

In addition to measuring how the gluon jets hadronizes, we are also interested in measuring how they split:  $g \rightarrow gg$ . We do so by looking at 4-jet events with high  $g$ -tag values and then identify the two gluon jets (the ones with the lowest  $b$ -tag values). From Figure 5.22, the  $\gamma_{\text{tag}}$  cut off threshold is set to  $\gamma_{\text{cutoff}} = 0.8$  for 4-jet events. This corresponds to selecting 41 117 events in MC as gluon events with a signal efficiency of  $\varepsilon_g^{4\text{-jet}} = 23.30\%$  and a signal purity of  $\rho_g^{4\text{-jet}} = 92.67\%$ .

### 5.9.1 Variables

The variables we use to measure the gluon splitting are each meant to probe different, smaller parts of the phase space. It is difficult to parametrize the basis of this phase space, but in discussion with one of the authors of the MC simulator Pythia [85], Peter Skands, the first dimension of the phase space will be the energy asymmetry. The energy asymmetry describes how the two gluons share their available energy between them; do they share it equally or does one of them get the majority of it? The second dimension is the resolution scale which probes the hardness of the gluons by looking at their invariant mass and the angle between the their jets. The third axis

Note that the number of selected events in the 4-jet case is much lower than in the 3-jet case and that the signal purity is lower as well,  $\rho_g^{3\text{-jet}} = 98.77\%$  vs.  $\rho_g^{4\text{-jet}} = 92.67\%$ , at the selected cut value.

is the azimuthal angle which measures the rotational distribution of the gluons compared to the quarks. In addition to these, some extra variables were proposed by Peter Skands [86]. These “Peter Skands”-variables are aimed at other probing other interesting areas of the phase space.

The gluon splitting variables are variables where current MC generators, such as Pythia, and Data show some discrepancies. Better measurements of these variables might lead to new theoretical insights that can reduce these discrepancies. The gluon splitting variables are:

#### Energy Asymmetry:

$E_{\text{diff}}$ : The relative difference in energy between the gluon jet with the highest and lowest energy:  $E_{\text{diff}} = \frac{E_{\text{max}} - E_{\text{min}}}{E_{\text{max}} + E_{\text{min}}}$ .

$E_{\text{rel}_{\text{min}}}$ : The relative energy of the gluon jet with the lowest energy and the sum:  $E_{\text{rel}_{\text{min}}} = \frac{E_{\text{min}}}{E_{\text{max}} + E_{\text{min}}}$ .

$E_{\text{rel}}$ : The relative energy of the gluon jet with the lowest energy and the highest energy:  $E_{\text{rel}} = \frac{E_{\text{min}}}{E_{\text{max}}}$ .

#### Resolution Scale:

$\Delta_\theta$ : The angle between the two gluon jets.

$m_{gg}$ : The invariant mass of the two gluon jets.

#### Azimuthal Angle

$\phi_{\parallel}$ : The angle between the plane spanned by the two  $b$ -jets and the plane spanned by the two gluon jets. This is the same angle as the angle between the  $b$ -jet cross product  $\mathbf{p}_{b_1} \times \mathbf{p}_{b_2}$  and the gluon-jet cross product  $\mathbf{p}_{g_1} \times \mathbf{p}_{g_2}$  where  $\mathbf{p}$  is the jet momentum.

#### Peter Skands:

$\ln(k_t^2/m_{\text{vis}}^2)$ : Logarithm of the ratio between the  $k_t$  value, see equation (5.12), of the two gluon jets and the visible mass of the event.

$p_{\perp,A}^2$ : The  $p_{\perp,\text{perp}}$  antenna defined as:

$$p_{\perp,A}^2 = \tilde{m}_{12}^2 \cdot \min \left( \frac{\min(\tilde{m}_{b1}^2, \tilde{m}_{b2}^2) - m_b^2}{\tilde{m}_{b12}^2 - m_b^2}, \frac{\min(\tilde{m}_{b1}^2, \tilde{m}_{b2}^2) - m_b^2}{\tilde{m}_{b12}^2 - m_b^2} \right), \quad (5.10)$$

where  $\tilde{m}^2 = m^2 c \dot{m}_Z^2 / m_{\text{vis}}^2$  and  $m_Z$  is the mass of the  $Z$  boson.

The gluon splitting variables will be analyzed in distinct areas defined by the  $k_t$  [34, 45] and Cambridge/Aachen (CA) [43, 102] jet clustering algorithms for  $e^+e^-$  collisions which will first be described. The two algorithms uses the following<sup>28</sup> jet distance measure:

<sup>28</sup> When using  $R = 1$  in eq. (9a) in Ref. [33].

$$d_{ij}^2(p) = \min(E_i^{2p}, E_j^{2p}) \left( \frac{1 - \cos \theta_{ij}}{2} \right), \quad (5.11)$$

where  $E$  is the (pseudo)jet energy and  $\theta_{ij}$  is the angle between (pseudo)jet  $i$  and  $j$  [33]. For  $p = 1$  equation (5.11) is called the  $k_t$  algorithm and the Cambridge/Aachen for  $p = 0$ . Both the  $k_t$  and CA algorithms are newer jet clustering algorithms than JADE, see section 4.4, and their distance measures are also pretty similar to JADE's. The value  $d_{ij}(p = 1)$  is also known as the  $k_t$ :

$$k_t = \sqrt{\min(E_i^2, E_j^2) \left( \frac{1 - \cos \theta_{ij}}{2} \right)}. \quad (5.12)$$

Based on the two algorithms, we define the ratio  $R_{gg}$  between the two gluon jets  $d_{gg}^2$  and the lowest value of  $d_{ij}^2$  not including the two gluon jets:

$$R_{gg}(p) \equiv \frac{d_{gg}^2(p)}{\min_{(i,j) \neq (g,g)} d_{ij}^2(p)}. \quad (5.13)$$

We further define  $R_{gg}^{k_t} \equiv R_{gg}(p = 1)$  and  $R_{gg}^{CA} \equiv R_{gg}(p = 0)$ .

Since the CA algorithm is energy-independent and the  $k_t$  algorithm is not, they describe different parts of the phase space. One example of this is the case of soft wide gluon jets illustrated in Figure 5.29. Here the two gluon jets are low-energy (soft) jets but with a high angle between them (wide). In this case the  $k_t$  algorithm would probably cluster the two gluon jets together but the CA algorithm would not. This means that  $R_{gg}^{k_t}$  would be less than 1 since the distance measure between the two gluon jets would be the smallest of them all, whereas to  $R_{gg}^{CA}$  would be larger than 1 since  $d_{bg} < d_{gg}$ . In addition to the soft, wide angle gluon jets, we have the case of soft, collinear gluon jets which the two algorithms agree to cluster together, see Figure 5.30 or the opposite case where the two algorithms both agree on not to cluster the gluon jets together, see Figure 5.31. These figures are just illustrations of how to better understand the  $R_{gg}$  phase space.

The variables are computed for each event, and their relationship with  $\gamma_{\text{tag}}$  is shown in Figure B.32–B.39. From now on primarily events with “good”  $g$ -tags,  $\gamma_{\text{tag}} > 0.8$ , are used. The efficiency of these signal events are measured in the following subsection.

### 5.9.2 Efficiencies

It is not possible to take advantage of the Tag-Tag-Probe method for whole events as it was for individual jets in the 3-jet case. As such, we are also unable to estimate the  $g$ -tagging efficiency in Data of the gluon splitting variables defined in the previous subsection. However, it is still possible to do so for MC using the truth labels. The efficiency  $\varepsilon_{gg}^{4\text{-jet}}$  for the gluon splitting variable  $E_{\text{diff}}$  is shown in Figure 5.32 for signal and background based on MC Truth. Note that even though the efficiency here is quite low, it is close to constant (as a function of  $E_{\text{diff}}$ ).

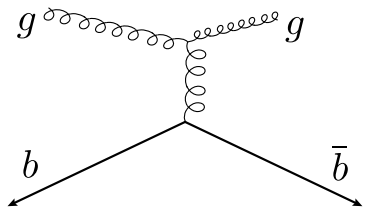


Figure 5.29: Soft, wide angle gluons in 4-jet events.

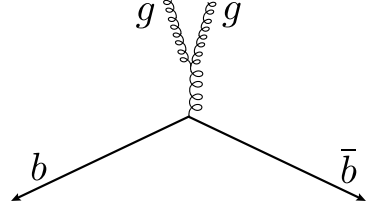


Figure 5.30: Soft, collinear gluons in 4-jet events.

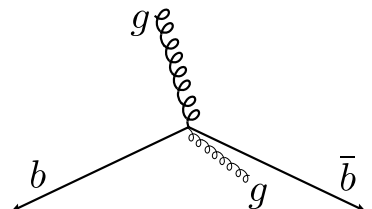
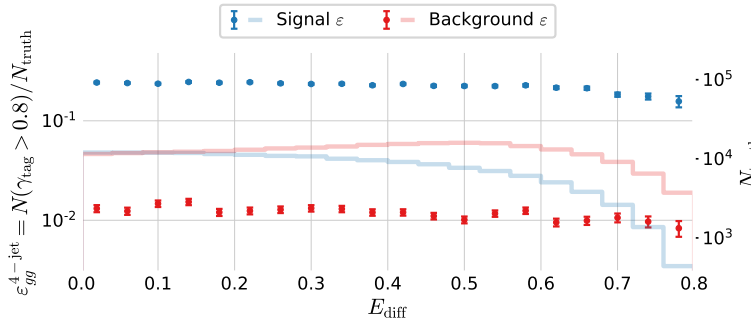


Figure 5.31: Hard, non  $g \rightarrow gg$  gluons in 4-jet events.



The plot for the rest of the  $g$ -tagging efficiencies can be seen in Figure B.40–B.49.

### 5.9.3 Closure Test

I perform a closure test to validate the  $g$ -tagging model for the gluon variables in 4-jet events. Closure tests compare the developed method after corrections<sup>29</sup> to MC Truth. Any discrepancies can then be investigated and finally the closure test can gauge the systematic uncertainties of the analysis.

The closure test is based on the distribution of the gluon splitting variables, see subsection 5.9.1, for events in the signal region or the so-called *sideband region*. The sideband region<sup>30</sup> is a region close to the signal region where the background is expected to behave approximately similar to the background in the signal region (and likewise for the signal). From Figure 5.22, the signal region was defined to be  $0.8 < \gamma_{\text{tag}}$  for 4-jet events. This region is expected to contain primarily signal events. For 4-jet events, we define the sideband region to be  $0.6 < \gamma_{\text{tag}} < 0.8$ .

The aim is to fully reconstruct the true distribution  $\mathcal{P}_{gg}(x)$  of any gluon splitting variable  $x$ . To first order, this is given by  $\mathcal{P}_{gg} \approx \mathcal{P}_{\text{sig}}/\varepsilon_{gg}^{4\text{-jet}}$ , where  $\mathcal{P}_{\text{sig}}(x)$  is the distribution of  $x$  for all events in the signal region. However, this expression completely ignores the background events that are also found in the signal region. To correct for the assumption of no background, we introduce  $\mathcal{P}_{\text{bkg}}(x)$  which is the distribution of  $x$  for background events:

$$\mathcal{P}_{gg} = \frac{\mathcal{P}_{\text{sig}} - \alpha \cdot \mathcal{P}_{\text{bkg}}}{\varepsilon_{gg}^{4\text{-jet}}}. \quad (5.14)$$

Here  $\alpha$  is the fraction of background events in the signal region  $N_{\text{bkg}}^{\text{sig}}$  relative to the background events in the sideband  $N_{\text{bkg}}^{\text{side}}$ . Letting  $f_{gg}^{\text{sig}}$  denote the fraction of signal in the signal region and  $f_{\text{bkg}}^{\text{side}}$  the fraction of background in the sideband region,  $\alpha$  is defined as:

$$\alpha = \frac{N_{\text{bkg}}^{\text{sig}}}{N_{\text{bkg}}^{\text{side}}} = \frac{(1 - f_{gg}^{\text{sig}}) \cdot N_{\text{sig}}}{f_{\text{bkg}}^{\text{side}} \cdot N_{\text{side}}}, \quad (5.15)$$

where  $N_i$  is the number of events in region  $i$  (either signal or sideband). The background distribution  $\mathcal{P}_{\text{bkg}}(x)$  itself can be approxi-

Figure 5.32: Efficiency of the  $g$ -tagging algorithm for 4-jet events as a function of normalized gluon-gluon jet energy difference (asymmetry)  $E_{\text{diff}}$  in MC. The efficiency is measured as the number of events with a  $g$ -tag higher than 0.8 ( $\gamma > 0.8$ ) out of the total number. The efficiency is plotted for **signal events** according to MC Truth in blue and **background events** according to MC Truth in red.

<sup>29</sup> E.g. Applying the efficiencies found in the previous subsection.

<sup>30</sup> Also sometimes known as the control region.

mated to be  $\mathcal{P}_{\text{bkg}} \approx \mathcal{P}_{\text{side}}$  if assuming no signal events in the sideband region, yet this assumption is also not satisfied and is thus corrected for:

$$\mathcal{P}_{\text{bkg}} = \mathcal{P}_{\text{side}} - \beta \cdot \mathcal{P}_{gg} \cdot \varepsilon_{gg}^{4\text{-jet}}, \quad (5.16)$$

where  $\beta$  is the fraction of signal events in the sideband region relative to the signal events in the signal region and is defined as:

$$\beta = \frac{(1 - f_{\text{bkg}}^{\text{side}}) \cdot N_{\text{side}}}{f_{gg}^{\text{sig}} \cdot N_{\text{sig}}}. \quad (5.17)$$

Plugging equation (5.16) into (5.14) and solving for  $\mathcal{P}_{gg}$  yields:

$$\mathcal{P}_{gg} = \frac{\mathcal{P}_{\text{sig}} - \alpha \cdot \mathcal{P}_{\text{side}}}{\varepsilon_{gg}^{4\text{-jet}} \cdot (1 + \alpha\beta)}. \quad (5.18)$$

The advantage of this equation is that only  $\varepsilon_{gg}^{4\text{-jet}}$  and the two constants<sup>31</sup>  $f_{gg}^{\text{sig}}$  and  $f_{\text{bkg}}^{\text{side}}$  depend on MC truth, the rest can be applied to data without any truth label. It should be made clear that the final expression, equation (5.18), is based on the assumption that the signal distribution of  $x$  is (approximately) similar in the signal and sideband regions  $\mathcal{P}_{gg}^{\text{sig}} \approx \mathcal{P}_{gg}^{\text{side}}$  and likewise for the background distributions  $\mathcal{P}_{\text{bkg}}^{\text{sig}} \approx \mathcal{P}_{\text{bkg}}^{\text{side}}$ .

The distribution of  $\mathcal{P}_{gg}$  in MC is shown in Figure 5.33 together with  $\mathcal{P}_{\text{sig}}$ ,  $\mathcal{P}_{\text{side}}$ , and the distribution for MC Truth  $\mathcal{P}_{gg}^{\text{Truth}}$ . In this figure the distributions are shown for the gluon splitting variable  $E_{\text{diff}}$  with histograms shown in the top plot and a ratio plot between  $\mathcal{P}_{gg}$  and  $\mathcal{P}_{gg}^{\text{Truth}}$  in the bottom part. By just looking at the distributions, it can be seen that the distributions in the signal and sideband regions follow each quite closely even though they start to differ at large values of  $E_{\text{diff}}$ . Similarly, also  $\mathcal{P}_{gg}$  and  $\mathcal{P}_{gg}^{\text{Truth}}$  follow each other quite closely, however, by looking at the ratio plot it can be seen that  $\mathcal{P}_{gg}$  generally has fewer counts in each bin than  $\mathcal{P}_{gg}^{\text{Truth}}$ .

<sup>31</sup> Which are found to be:  
 $f_{gg}^{\text{sig}} = \rho_g^{4\text{-jet}} = 92.67\%$   
 $f_{\text{bkg}}^{\text{side}} = 62.5\%$ .

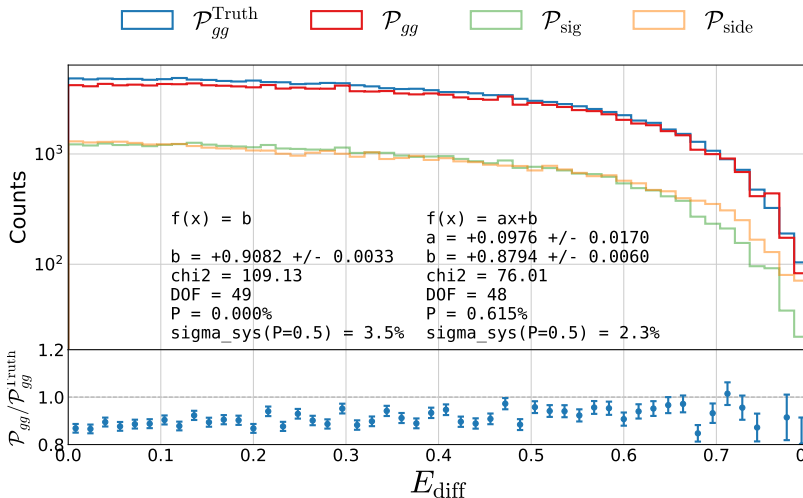


Figure 5.33: Closure plot comparing MC Truth and the efficiency corrected g-tagging model in 4-jet events for the normalized gluon gluon jet energy asymmetry  $E_{\text{diff}}$ . In the top part of the plot  $\mathcal{P}_{gg}^{\text{Truth}}$  based on MC Truth is shown in blue, the  $\mathcal{P}_{gg}$  based on MC but without Truth in red, the distribution in the signal region  $\mathcal{P}_{\text{sig}}$  in light green and the distribution in the sideband region  $\mathcal{P}_{\text{side}}$  in light orange. In the bottom part of the plot the ratio between  $\mathcal{P}_{gg}$  and  $\mathcal{P}_{gg}^{\text{Truth}}$  is shown.

The errorbars in the ratio plot is fitted with both a constant  $f(x) = b$  and a straight line  $f(x) = ax + b$  with the fit results shown as

text in the plot. In the text box `DOF` is the number of degrees of freedom and `P` is the  $\chi^2$ -probability<sup>32</sup>. I compute the systematic error  $\sigma_{\text{sys}}$  that would have to be added in quadrature to the standard deviation,  $\sigma \rightarrow \sqrt{\sigma^2 + \sigma_{\text{sys}}^2}$ , such that the  $\chi^2$ -probability would be 50 %. I do this using Brent's method [27] and the systematic error is written as `sigma_sys` in the figure.

The closure plot for the rest of the gluon splitting variables in Figure B.50–B.57. In general it can be seen that the  $\mathcal{P}_{gg}$  matches  $\mathcal{P}_{gg}^{\text{Truth}}$  pretty well for all the gluon splitting variables, however, with a 10 % offset. This offset is easy to correct for with a constant correction factor. However, we see that for the energy asymmetry variables and  $\Delta_\theta$  there are clear, linear trends in the ratio plots. This is seen e.g. for  $E_{\text{diff}}$  in Figure 5.33 where the  $\chi^2$  value for the constant fit is 109.13 but only 76.01 for the linear fit. This difference in  $\chi^2$  value cannot be attributed to just the linear fit being a more advanced fit in which case the difference would be expected to be  $\Delta\chi^2 \sim 1$  due to difference in the number of fit parameters being 1. For these four variables the systematic uncertainty will thus be based on the linear fit, whereas it will be based on the constant for the rest of the variables.

The  $g$ -tagging algorithm perform well in general where most of the systematic attributed are 2 % to 3 %. The highest systematic uncertainty is for the invariant mass of the two gluons:  $\sigma_{\text{sys}}(m_{gg}) = 3.6$  %. A summary of all the systematic errors from the closure tests can be seen in Table 5.6 for all of the gluon splitting variables.

The closure test shows that the  $g$ -tagging algorithm can also be trusted in the 4-jet case, however, with high systematic uncertainties for the  $m_{gg}$  variable.

#### 5.9.4 4-jet results

The comparison between the gluon splitting distributions will be done in four distinct areas of the  $R_{gg}^{k_t}$ - $R_{gg}^{\text{CA}}$  phase space. These four areas, A, B, C, and D, are defined in Table 5.7. Three of these regions have already been described, that is area A which is the soft, collinear region with an example shown in Figure 5.30, area C which is the soft, wide angle region in Figure 5.29, and the hard non- $g \rightarrow gg$  area D in Figure 5.31. Area B is a region where neither the  $k_t$  algorithm nor the CA algorithm is totally sure whether or not the two gluons should be clustered together. The four areas are visualized in Figure 5.34 for both MC and Data. Here each dot shown in the scatter plot is an event with  $0.8 < \gamma_{\text{tag}}$ , with a total of 41 117 events in the MC sample and 22 473 events in the data sample. The number of events that fall into each of the four areas are shown in the figure. The events are split up into these four areas because they each concern different physical interactions. The number of events in each area were taken into account when creating the ranges in Table 5.7 to minimize the statistical uncertainties.

The distributions for the different gluons splitting variables for area A, the soft, collinear region, is shown in Figure 5.35 for both

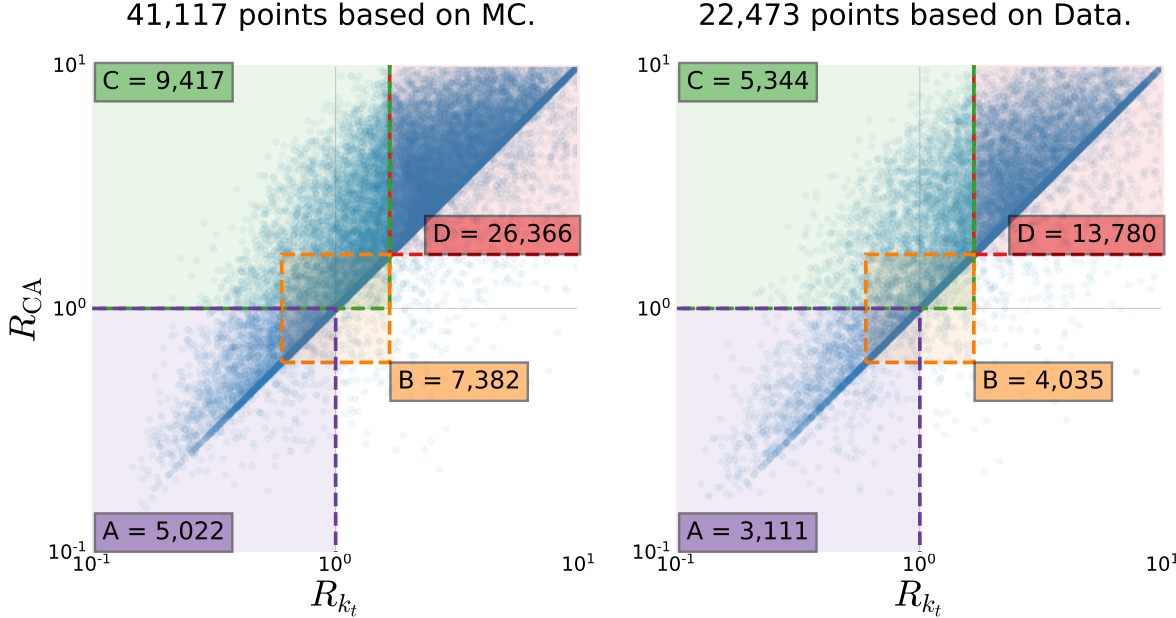
<sup>32</sup>  $P(\chi^2; N_{\text{DOF}}) = \int_{\chi^2}^{\infty} f_{\chi^2}(x; N_{\text{DOF}}) dx$ , where  $f_{\chi^2}(x; N_{\text{DOF}})$  is the  $\chi^2$  distribution with  $N_{\text{DOF}}$  degrees of freedom.

	$\sigma_{\text{sys}}$	$f(x)$
$E_{\text{diff}}$	2.3 %	$ax + b$
$E_{\text{rel,min}}$	2.3 %	$ax + b$
$E_{\text{rel}}$	2.5 %	$ax + b$
$\Delta_\theta$	2.0 %	$ax + b$
$m_{gg}$	3.6 %	$b$
$\phi_{\parallel}$	1.7 %	$b$
$\ln(k_t^2/m_{\text{vis}}^2)$	2.1 %	$b$
$p_{\perp,A}^2$	3.1 %	$b$

Table 5.6: Systematic errors for the gluon splitting variables based on the closure test, see subsection 5.9.3. The last column,  $f(x)$ , denotes which fit the systematic error is based on.

Region	$R_{gg}^{k_t}$	$R_{gg}^{\text{CA}}$
A	$[0, 1]$	$[0, 1]$
B	$[\frac{3}{5}, \frac{5}{3}]$	$[\frac{3}{5}, \frac{5}{3}]$
C	$[0, \frac{5}{3}]$	$[1, \infty]$
D	$[\frac{5}{3}, \infty]$	$[\frac{5}{3}, \infty]$

Table 5.7: Definitions of the four areas in the  $R_{gg}^{k_t}$ - $R_{gg}^{\text{CA}}$  phase space.



MC (scaled to Data) and Data. Area A contains 5022 events in the MC sample and 3111 in the Data sample. Generally the distributions match pretty well between the MC and Data, however, there seems to small discrepancies in the energy asymmetry variables, however, this might just be due to statistical fluctuations (notice the low bin count in each bin). When looking at the other areas, see Figure B.58–B.61, the energy discrepancies seem to disappear. In general there seems to be a reasonably good correspondence between the distributions.

### 5.10 Quark-Gluon Discussion

Here a discussion of this analysis...

Figure 5.34: Overview of the four areas, A, B, C, and D, in the  $R_{gg}^{k_t}$ - $R_{gg}^{CA}$  phase space. The areas are shown as colored rectangles together with a scatter plot showing the 2D-distribution for signal gluon events ( $0.8 < \gamma_{tag}$ ). The left plot shows is for MC and the right one for Data.

Cut region A with 5022 MC events and 3111 data events.

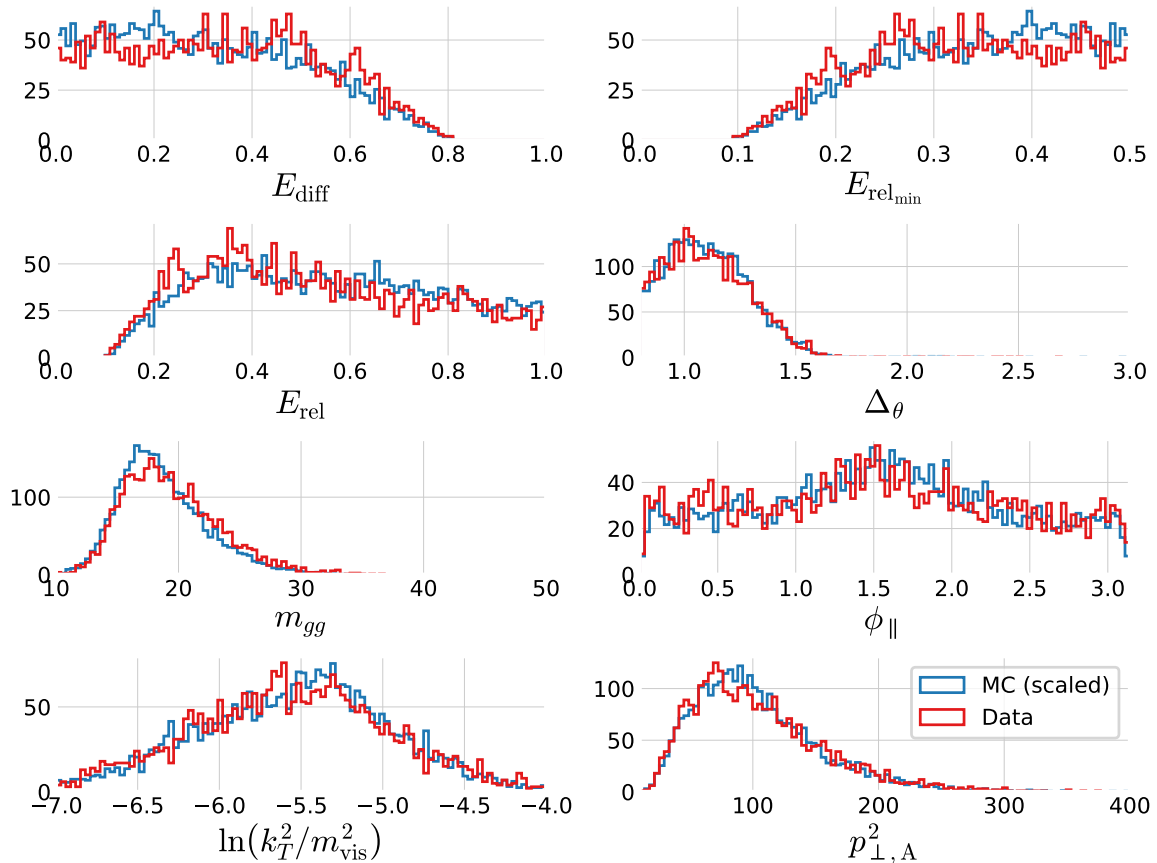


Figure 5.35: Comparison of the gluon splitting distributions in MC and Data for  $R_{gg}^{k_t}$ - $R_{gg}^{CA}$  Phase Space Area A, see Table 5.7. The distribution for MC (scaled to Data) is shown in blue and for Data in red. These eight distributions are for the  $R_{gg}^{k_t}$ - $R_{gg}^{CA}$  Phase Space Area A which has 5022 events in the MC sample and 3111 in the Data sample.



## *Part III*

Part III of this thesis discusses and concludes the two subprojects.



## *B. Quarks vs. Gluons Appendix*

	$b$	$c$	$uds$	$g$	non- $q$ -matched
2	37.2 %	12.9 %	29.1 %	0.0 %	20.7 %
3	22.6 %	8.9 %	19.7 %	31.2 %	17.5 %
4	14.6 %	7.0 %	15.0 %	45.1 %	18.3 %
5	10.0 %	5.7 %	12.2 %	52.5 %	19.6 %
6	7.1 %	4.4 %	8.8 %	54.4 %	25.2 %

Table B.1: Number of different types of jets for MC and MCb written in relative numbers such that each row sum to 100 %. See also Table 5.3.

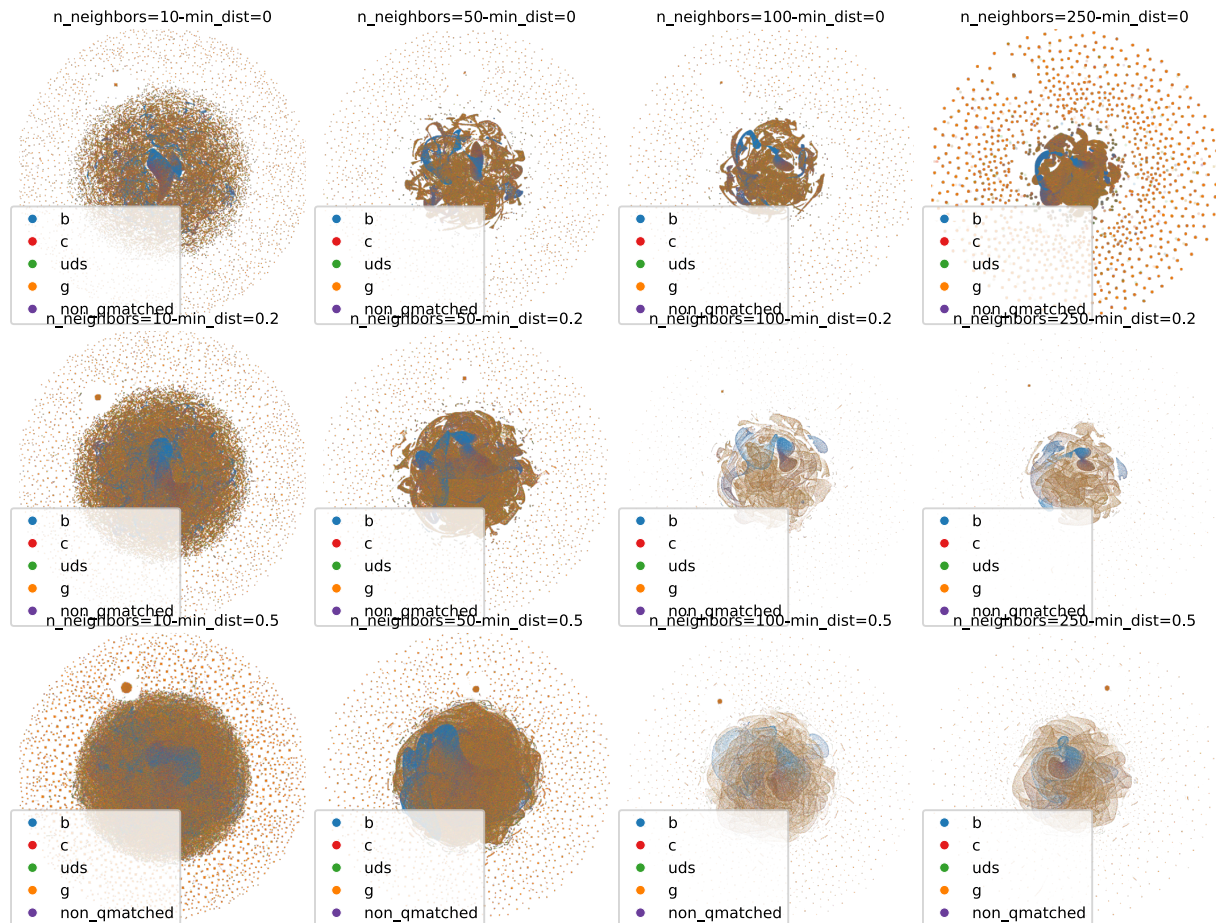


Figure B.1: Grid search of the two parameters `n_neighbors` and `min_dist` for the UMAP algorithm run on 4-jet events. For an explanation of these, see section 5.2.

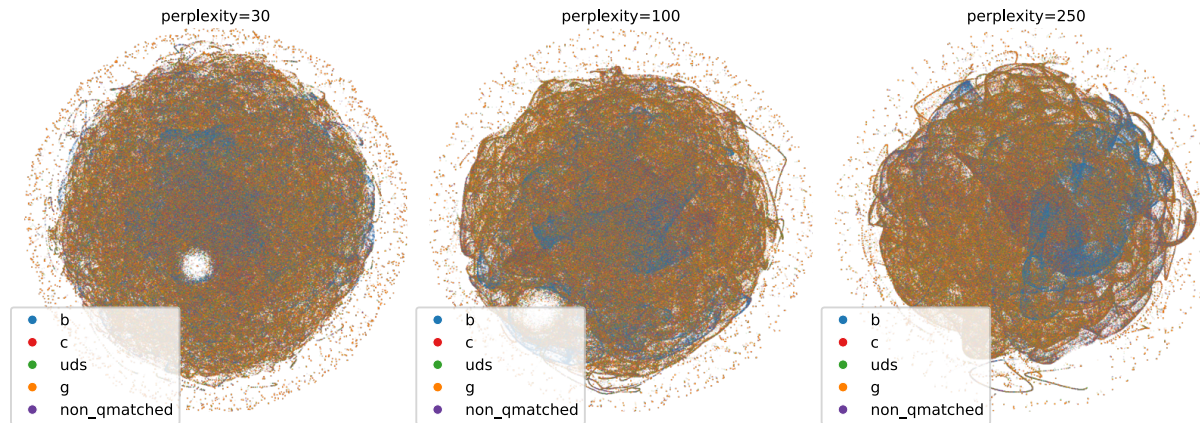


Figure B.2: Visualization of the t-SNE algorithm as a function of the `perplexity` parameters for 4-jet events.

Hyperparameter	Range
subsample	$\mathcal{U}(0.4, 1)$
colsample_bytree	$\mathcal{U}_{\text{trunc}}(0.4, 1, 2)$
max_depth	$\mathcal{U}_{\text{int}}(1, 20)$
min_child_weight	$\mathcal{U}_{\text{int}}(0, 10)$

Table B.2: Probability Density Functions for the random search hyperparameter optimization process for the XGBoost model.

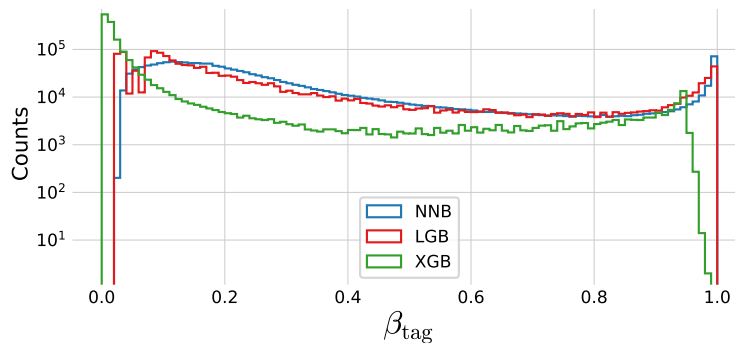
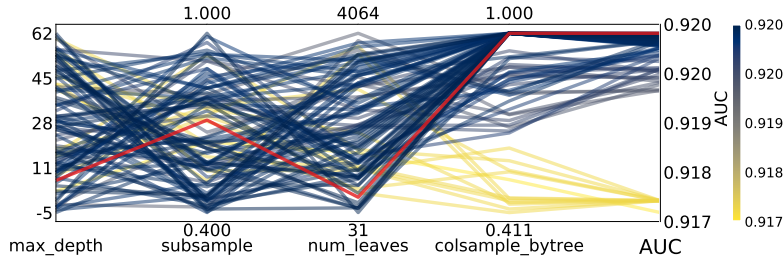


Figure B.3: Hyperparameter optimization results of  $b$ -tagging for 3-jet events. The results are shown as parallel coordinates with each hyperparameter along the  $x$ -axis and the value of that parameter on the  $y$ -axis. Each line is an event in the 4-dimensional space colored according to the performance of that hyperparameter as measured by AUC from highest AUC in dark blue to lowest AUC in yellow. The **single best hyperparameter** is shown in red.

Figure B.4: Histogram of  $b$ -tag scores  $\beta_{\text{tag}}$  in 3-jet events for **NNB** (the neural network pre-trained by ALEPH, also called `nnbjet`) in blue, **LGB** in red, and **XGB** in green.

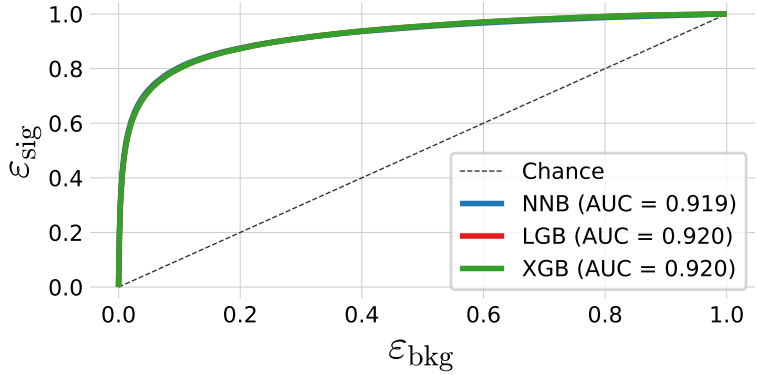


Figure B.5: ROC curve of the three  $b$ -tag models in 3-jet events for **NNB** (the pre-trained neural network trained by ALEPH, also called `nnbjet`) in blue, **LGB** in red, and **XGB** in green. In the legend the area under curve (AUC) is also shown. Notice that the LGB and XGB models share performance and it is thus due to overplotting that only the green line for XGB can be seen. In the machine learning community the background efficiency  $\epsilon_{\text{bkg}}$  is sometimes known as the false positive rate (FPR) and the signal efficiency  $\epsilon_{\text{sig}}$  as the true positive rate (TPR).

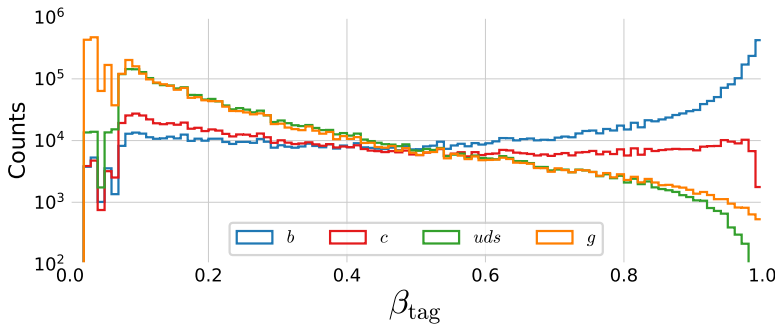


Figure B.6: Distribution of  $b$ -tags in 3-jet events for  **$b$ -jets** in blue,  **$c$ -jets** in red,  **$uds$**  in green and  **$g$**  in orange.

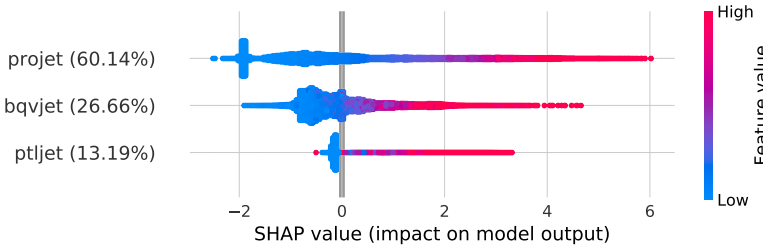


Figure B.7: Global feature importances for the LGB  $b$ -tagging algorithm on 3-jet events. The normalized feature importance is shown in the parenthesis and the each dot is an observation showing the dependence between the SHAP value and the feature's value.

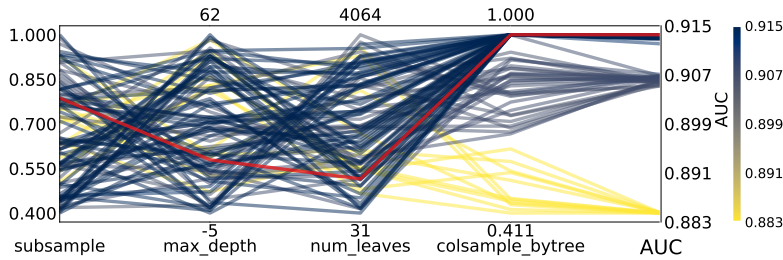


Figure B.8: Hyperparameter optimization results of  $g$ -tagging for 3-jet events for energy ordered jets.

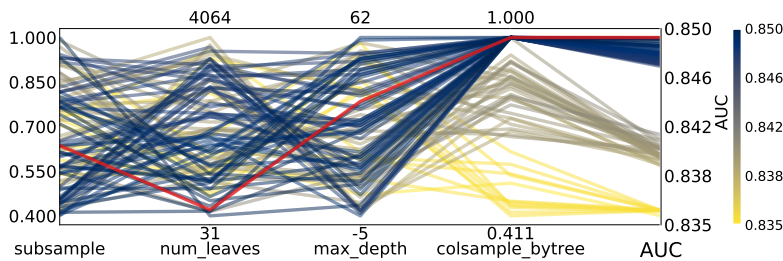


Figure B.9: Hyperparameter optimization results of  $g$ -tagging for 3-jet events for (row) shuffled jets.

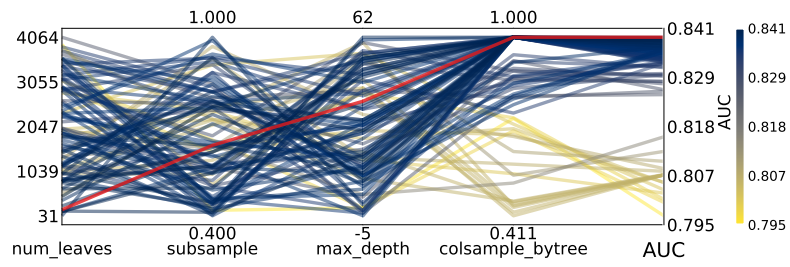


Figure B.10: Hyperparameter optimization results of  $g$ -tagging for 4-jet events for energy ordered jets.

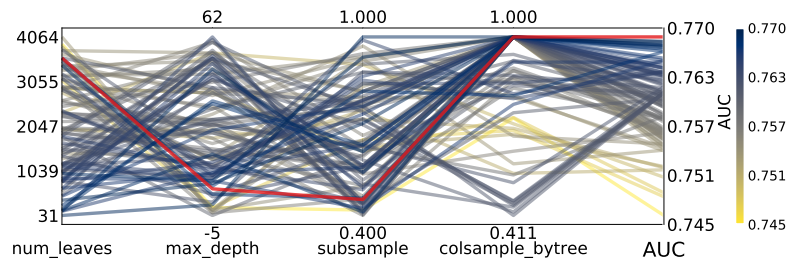


Figure B.11: Hyperparameter optimization results of  $g$ -tagging for 4-jet events for (row) shuffled jets.

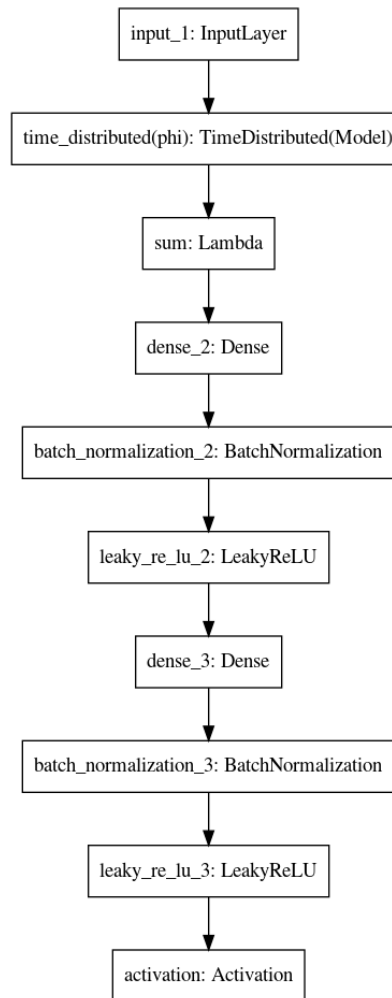


Figure B.12: Architecture of the PermNet neural network.

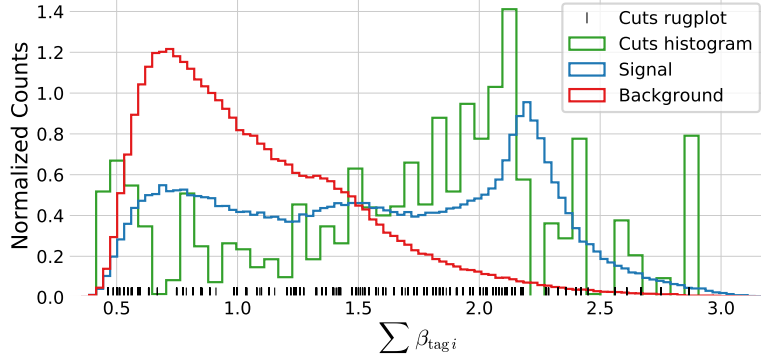


Figure B.13: Histogram of the distribution of [signal](#) in blue and [background](#) in red for the 1-dimensional sum of  $b$ -tags for 4-jet events. A histogram of the [cut values](#) from the LGB model trained on this data is shown in green together with a rug plot of the cut values in black. Notice how most of the cuts match up with the signal peak at around a  $\sum \beta_i \sim 2.1$ .

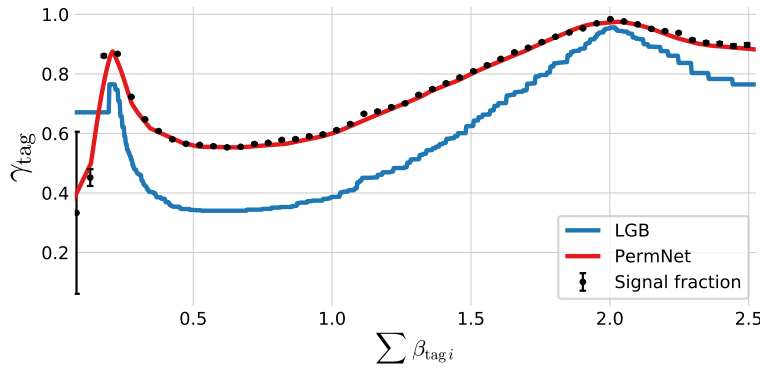


Figure B.14: Plot of the (1D) [g](#)-tag scores for 3-jet events as a function of  $\sum \beta_i$  for the [LGB](#) model in blue and the [PermNet](#) model in red. The signal fraction (based on the signal and background histograms in Figure B.15) is plotted as black error bars where the size of the error bars is based on the propagated uncertainties of the signal and background histogram assuming Poissonian statistics.

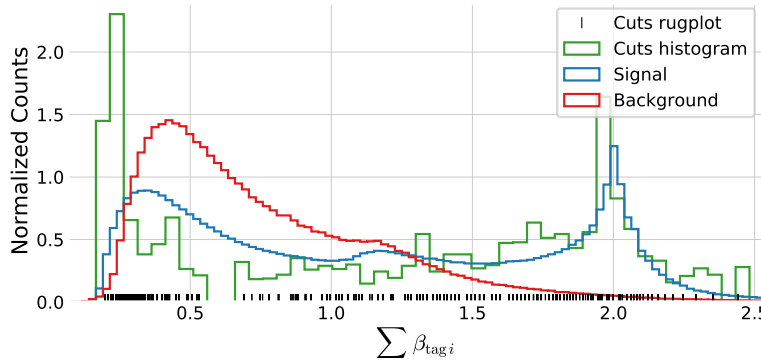


Figure B.15: Histogram of the distribution of [signal](#) in blue and [background](#) in red for the 1-dimensional sum of  $b$ -tags for 3-jet events. A histogram of the [cut values](#) from the LGB model trained on this data is shown in green together with a rug plot of the cut values in black. Notice how most of the cuts match up with the signal peak at around a  $\sum \beta_i \sim 2.1$ .

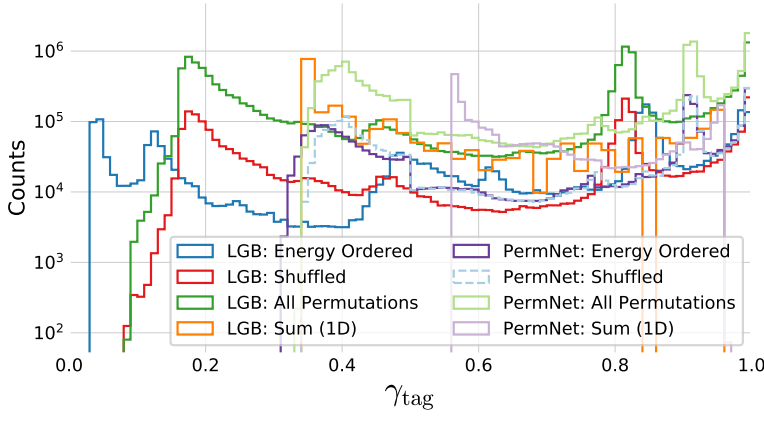


Figure B.16: Distribution of  $g$ -tag scores in 3-jet events shown with a logarithmic  $y$ -scale for LGB: Energy Ordered in blue, LGB: Shuffled in red, LGB: All Permutations in green, LGB: Sum 1D in orange, PermNet: Energy Ordered in purple, PermNet: Shuffled in light-blue, PermNet: All Permutations in light-green, PermNet: Sum 1D in light-purple. Here LGB and PermNet are the two different type of models and “Energy Ordered”, “Shuffled”, “All Permutations”, and “Sum 1D” are the different methods used for making the input data permutation invariant (except energy ordered).

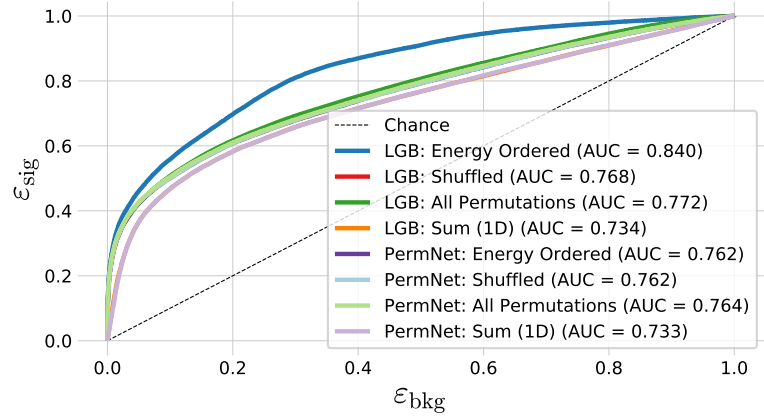


Figure B.17: ROC curve of the eight  $g$ -tag models in 4-jet events. First one in dashed black is the ROC curve that you get by random chance. The colors are the same as in Figure 5.20 and in the legend also the Area Under the ROC curve (AUC) is shown. Notice that the XGB model which uses the energy ordered data produced the best model, however, this model is not permutation invariant. Of the permutation invariant models (the rest), the XGB model trained on all permutations of the b-tags performs highest. The lowest performing models are the two models trained only on the 1-dimensional sum of b-tags, as expected, however, still with a better performance than expected by the author.

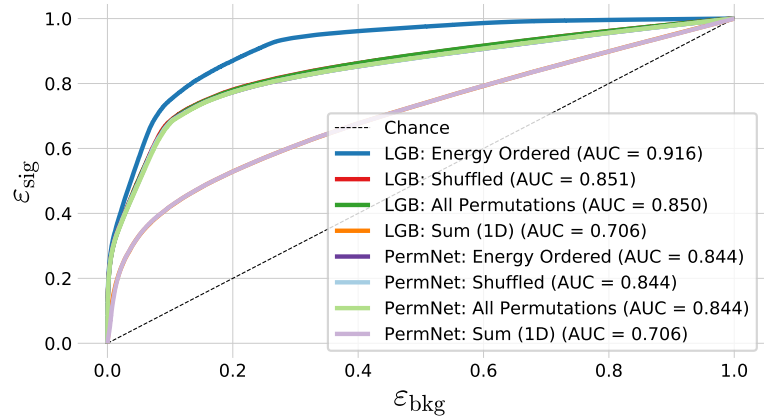


Figure B.18: ROC curve of the eight  $g$ -tag models in 3-jet. First one in dashed black is the ROC curve that you get by random chance. The colors are the same as in Figure 5.20 and in the legend also the Area Under the ROC curve (AUC) is shown.

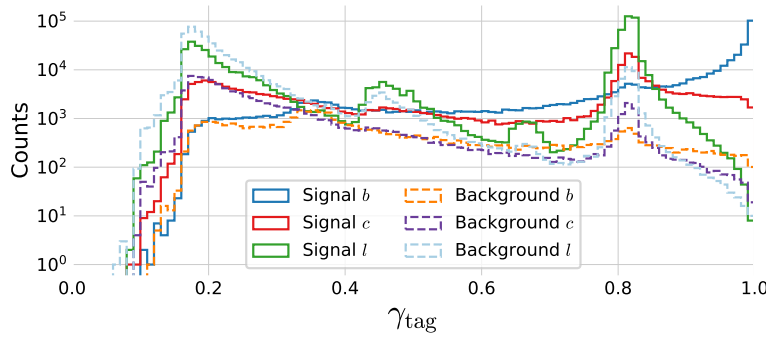


Figure B.19: Histogram of  $g$ -tag scores from the LGB-model in 3-jet events for  $b$  signal in blue,  $c$  signal in red,  $l$  ( $uds$ ) signal in green,  $b$  background in orange,  $c$  background in purple,  $l$  ( $uds$ ) background in light-blue.

$\beta_{\text{tag}_i}$	Energy Ordered	Shuffled	All Permutations
1	$0.827 \pm 0.006$	$0.924 \pm 0.006$	$0.923 \pm 0.006$
2	$0.749 \pm 0.006$	$0.909 \pm 0.006$	$0.918 \pm 0.005$
3	$1.198 \pm 0.006$	$0.878 \pm 0.005$	$0.906 \pm 0.005$

Table B.3: Global SHAP feature importances  $\phi_{\beta_i}^{\text{tot}}$  for the three  $g$ -Tagging Models in 3-Jet Events. Each  $\phi_{\beta_i}^{\text{tot}}$  is shown for the three methods in the columns and the three  $b$ -tags as variables in the rows.

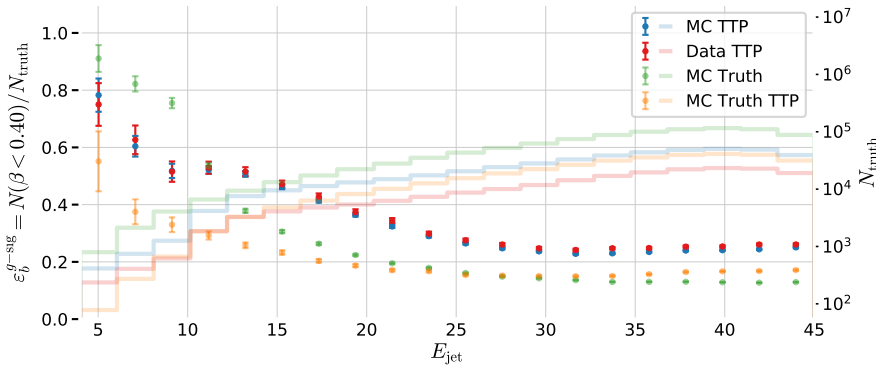


Figure B.20:  $b$ -tag efficiency for  $b$ -jets in the  $g$ -signal region for 3-jet events,  $\epsilon_b^{g\text{-sig}}$ , as a function of jet energy  $E_{\text{jet}}$ . In the plot the efficiencies are shown for MC TTP in blue, Data TTP in red, MC Truth TTP in green, and MC Truth in orange. The efficiencies (the errorbars) can be read off on the left  $y$ -axis and the counts (histograms) on the right  $y$ -axis.

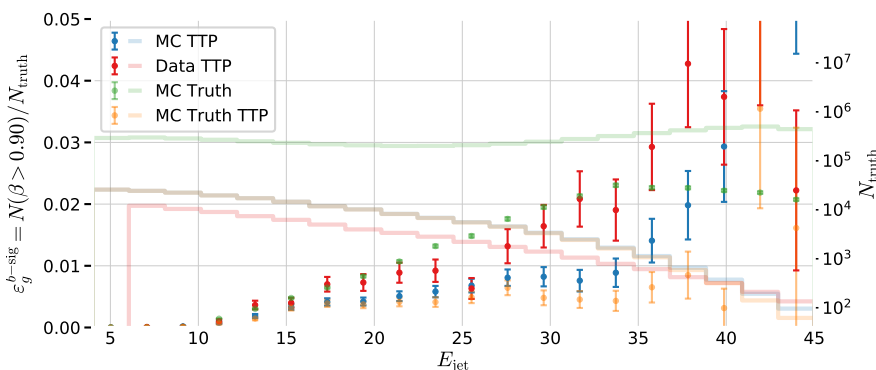


Figure B.21:  $b$ -tag efficiency for  $g$ -jets in the  $b$ -signal region for 3-jet events,  $\epsilon_g^{b\text{-sig}}$ , as a function of jet energy  $E_{\text{jet}}$ . In the plot the efficiencies are shown for MC TTP in blue, Data TTP in red, MC Truth TTP in green, and MC Truth in orange. The efficiencies (the errorbars) can be read off on the left  $y$ -axis and the counts (histograms) on the right  $y$ -axis.

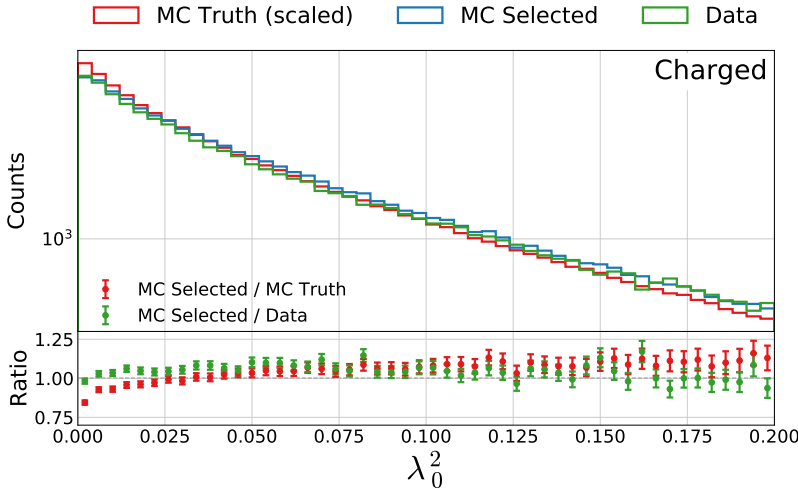


Figure B.22: Distribution of the generalized angularity  $\lambda_0^2$  for charged gluons jets in 3-jet events. The distributions for **MC Truth** is shown in red, **MC Truth** in blue, and **Data** in green in the top plot and in the bottom plot the ratio between **MC Selected** and **MC Truth** is shown in red and between **MC Selected** and **Data** in green.

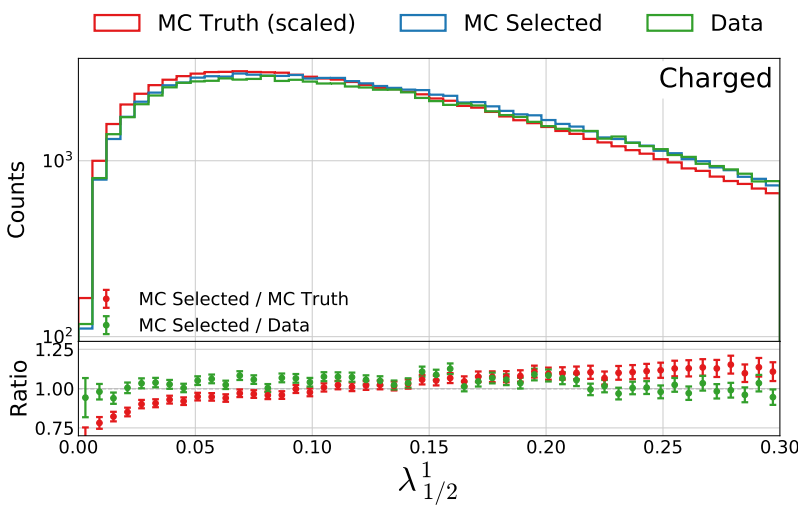


Figure B.23: Distribution of the generalized angularity  $\lambda_1^{1/2}$  for charged gluons jets in 3-jet events. The distributions for **MC Truth** is shown in red, **MC Truth** in blue, and **Data** in green in the top plot and in the bottom plot the ratio between **MC Selected** and **MC Truth** is shown in red and between **MC Selected** and **Data** in green.

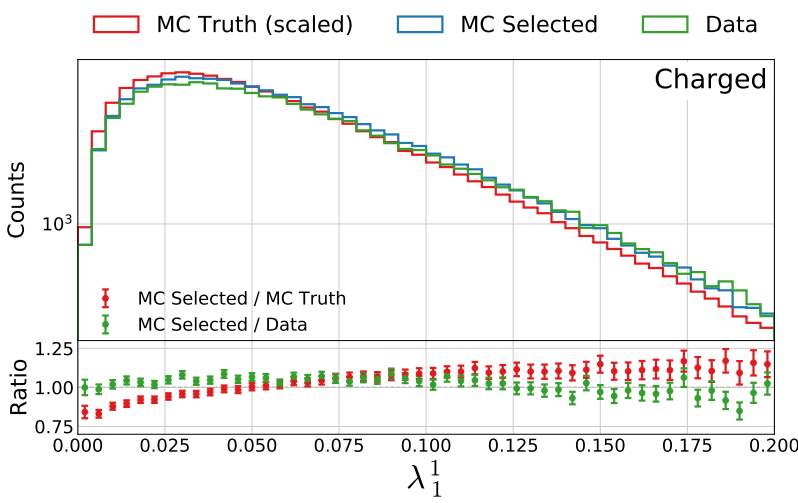
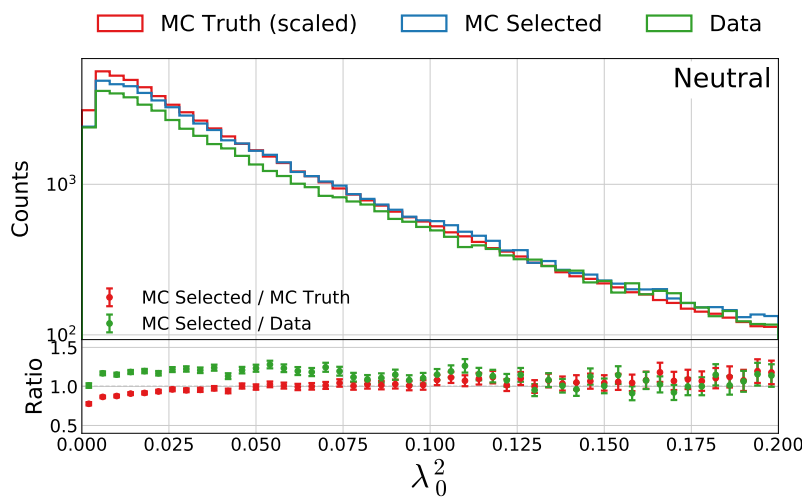
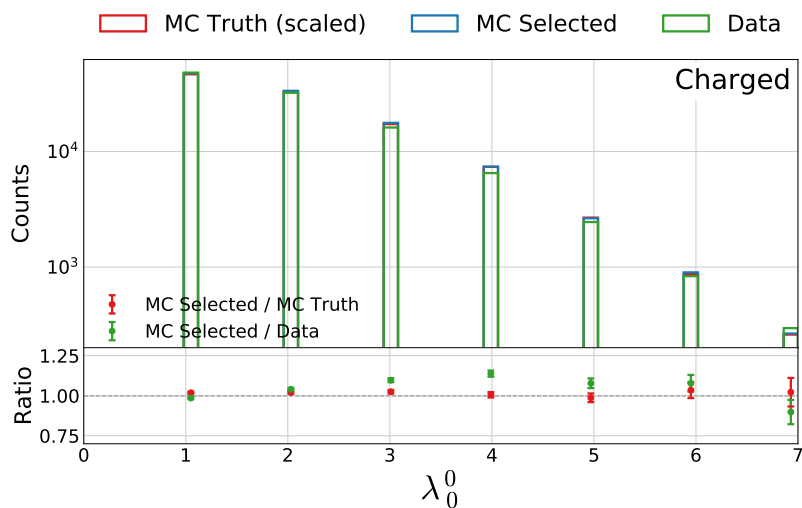
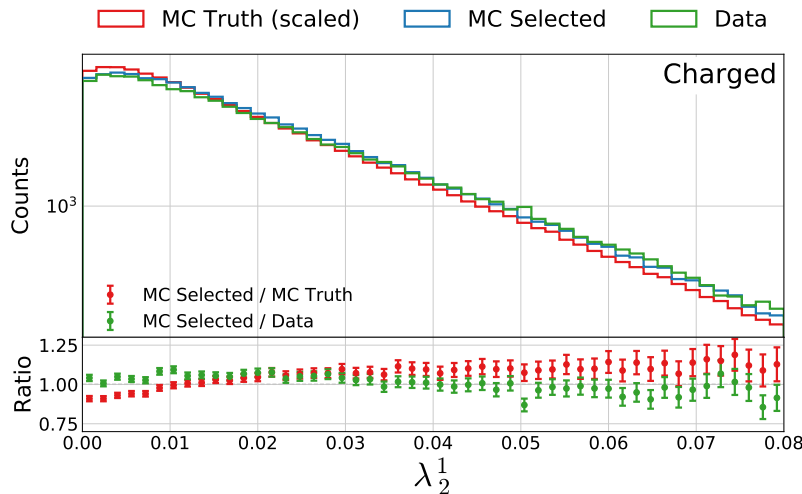


Figure B.24: Distribution of the generalized angularity  $\lambda_1^1$  for charged gluons jets in 3-jet events. The distributions for **MC Truth** is shown in red, **MC Truth** in blue, and **Data** in green in the top plot and in the bottom plot the ratio between **MC Selected** and **MC Truth** is shown in red and between **MC Selected** and **Data** in green.



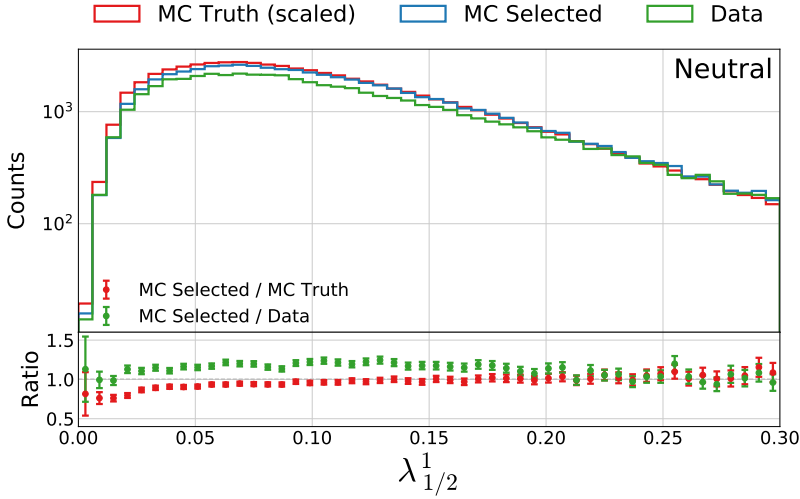


Figure B.28: Distribution of the generalized angularity  $\lambda_1^{1/2}$  for neutral gluons clusters in 3-jet events. The distributions for MC Truth is shown in red, MC Truth in blue, and Data in green in the top plot and in the bottom plot the ratio between MC Selected and MC Truth is shown in red and between MC Selected and Data in green.

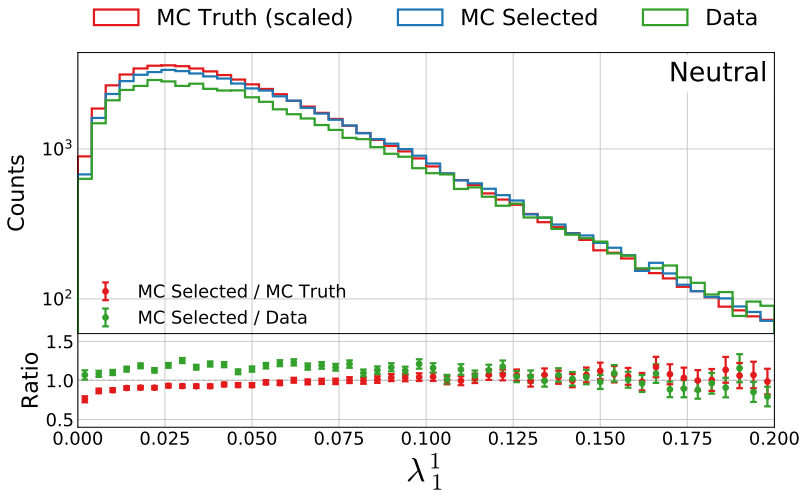


Figure B.29: Distribution of the generalized angularity  $\lambda_1^1$  for neutral gluons clusters in 3-jet events. The distributions for MC Truth is shown in red, MC Truth in blue, and Data in green in the top plot and in the bottom plot the ratio between MC Selected and MC Truth is shown in red and between MC Selected and Data in green.

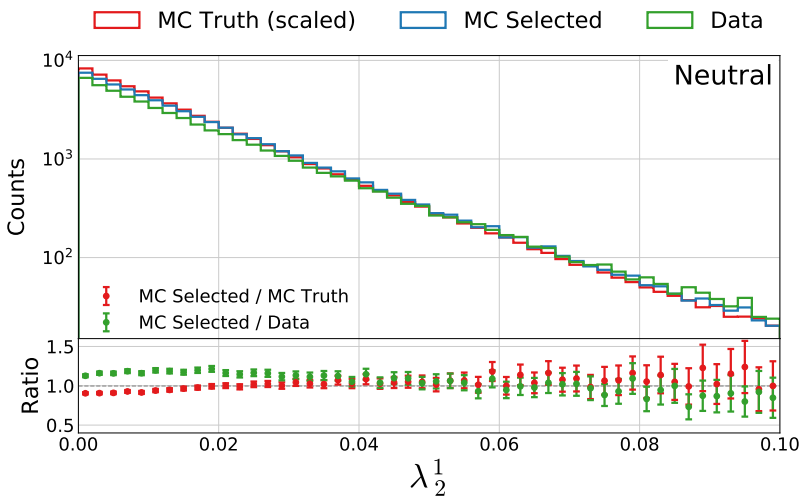


Figure B.30: Distribution of the generalized angularity  $\lambda_2^1$  for neutral gluons clusters in 3-jet events. The distributions for MC Truth is shown in red, MC Truth in blue, and Data in green in the top plot and in the bottom plot the ratio between MC Selected and MC Truth is shown in red and between MC Selected and Data in green.

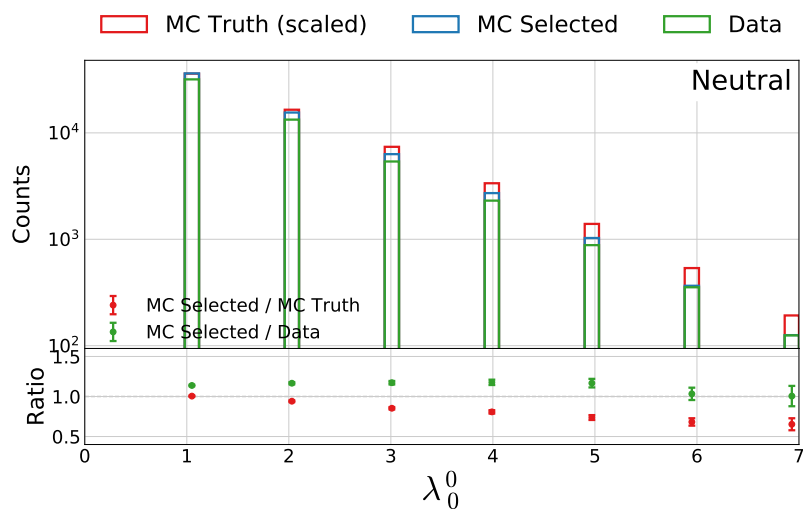


Figure B.31: Distribution of the generalized angularity  $\lambda_0^0$  for neutral gluons clusters in 3-jet events. The distributions for **MC Truth** is shown in red, **MC Selected** in blue, and **Data** in green in the top plot and in the bottom plot the ratio between **MC Selected** and **MC Truth** is shown in red and between **MC Selected** and **Data** in green.

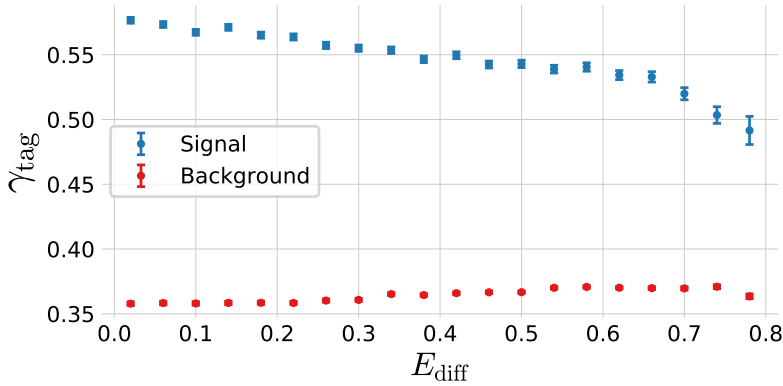


Figure B.32: Relationship between the  $g$ -tag value  $\gamma_{\text{tag}}$  and the gluon splitting variable  $E_{\text{diff}}$ . The **signal events** (according to MC Truth) are plotted in blue and **background events** (according to MC Truth) in red.

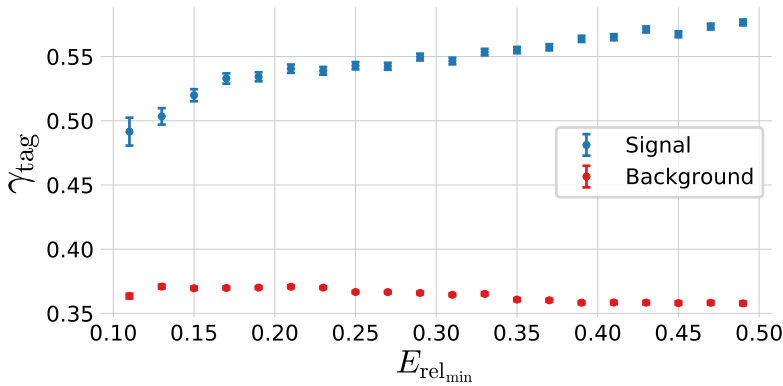


Figure B.33: Relationship between the  $g$ -tag value  $\gamma_{\text{tag}}$  and the gluon splitting variable  $E_{\text{rel},\min}$ . The **signal events** (according to MC Truth) are plotted in blue and **background events** (according to MC Truth) in red.

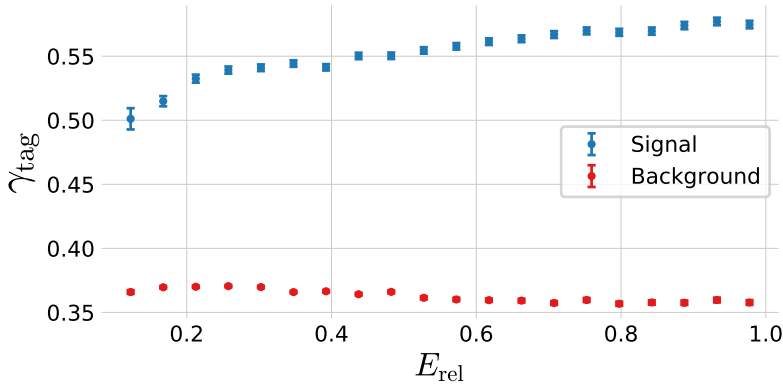


Figure B.34: Relationship between the  $g$ -tag value  $\gamma_{\text{tag}}$  and the gluon splitting variable  $E_{\text{rel}}$ . The **signal events** (according to MC Truth) are plotted in blue and **background events** (according to MC Truth) in red.

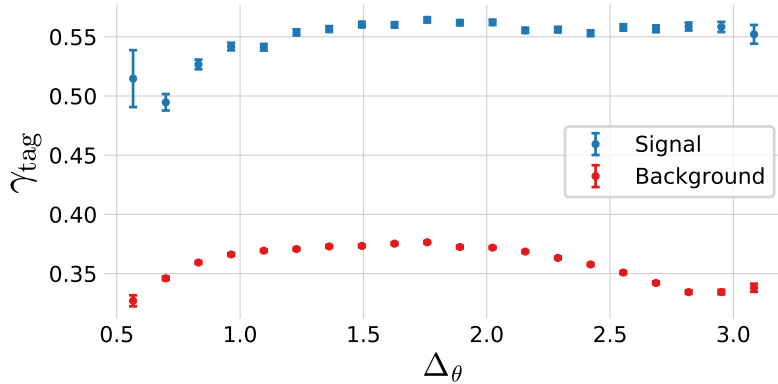


Figure B.35: Relationship between the  $g$ -tag value  $\gamma_{\text{tag}}$  and the gluon splitting variable  $\Delta_\theta$ . The **signal events** (according to MC Truth) are plotted in blue and **background events** (according to MC Truth) in red.

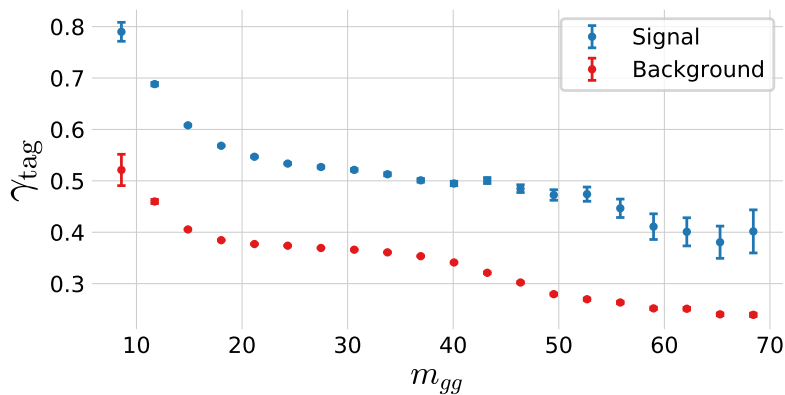


Figure B.36: Relationship between the  $g$ -tag value  $\gamma_{\text{tag}}$  and the gluon splitting variable  $m_{gg}$ . The **signal events** (according to MC Truth) are plotted in blue and **background events** (according to MC Truth) in red.

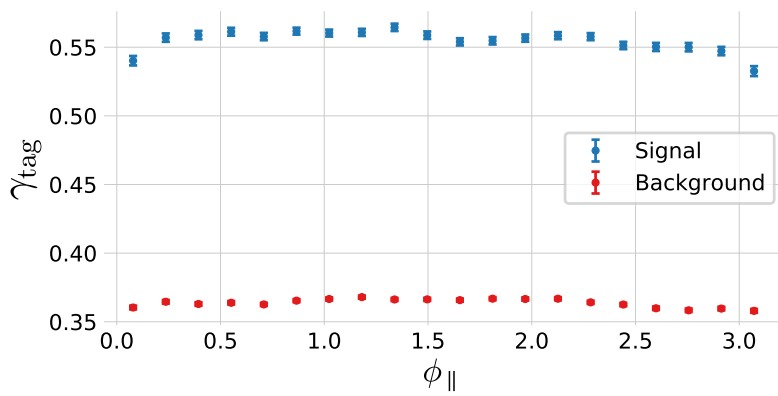


Figure B.37: Relationship between the  $g$ -tag value  $\gamma_{\text{tag}}$  and the gluon splitting variable  $\phi_{\parallel}$ . The **signal events** (according to MC Truth) are plotted in blue and **background events** (according to MC Truth) in red.

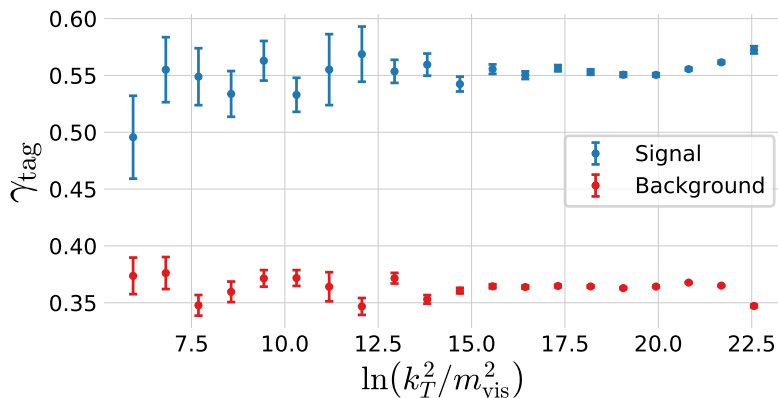


Figure B.38: Relationship between the  $g$ -tag value  $\gamma_{\text{tag}}$  and the gluon splitting variable  $\ln(k_T^2/m_{\text{vis}}^2)$ . The **signal events** (according to MC Truth) are plotted in blue and **background events** (according to MC Truth) in red.

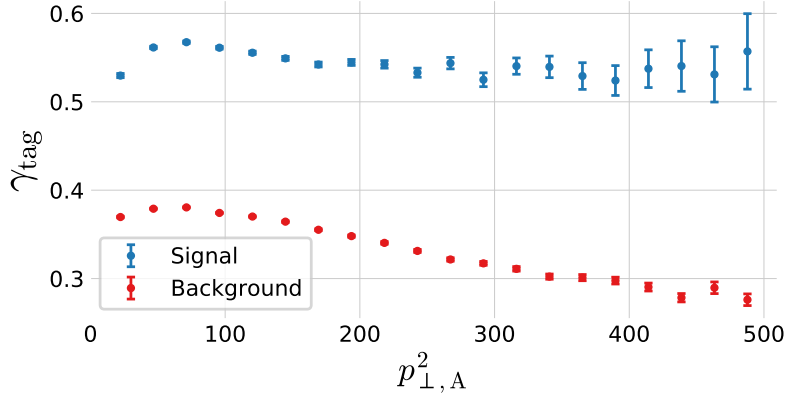


Figure B.39: Relationship between the  $g$ -tag value  $\gamma_{\text{tag}}$  and the gluon splitting variable  $p_{\perp A}^2$ . The **signal events** (according to MC Truth) are plotted in blue and **background events** (according to MC Truth) in red.

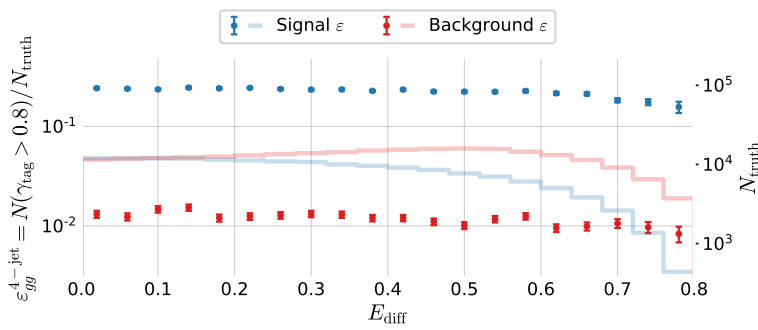


Figure B.40: Efficiency of the  $g$ -tagging algorithm for 4-jet events as a function of normalized gluon-gluon jet energy difference (asymmetry)  $E_{\text{diff}}$  in MC. The efficiency is measured as the number of events with a  $g$ -tag higher than 0.8 ( $\gamma > 0.8$ ) out of the total number. The efficiency is plotted for **signal events** according to MC Truth in blue and **background events** according to MC Truth in red.

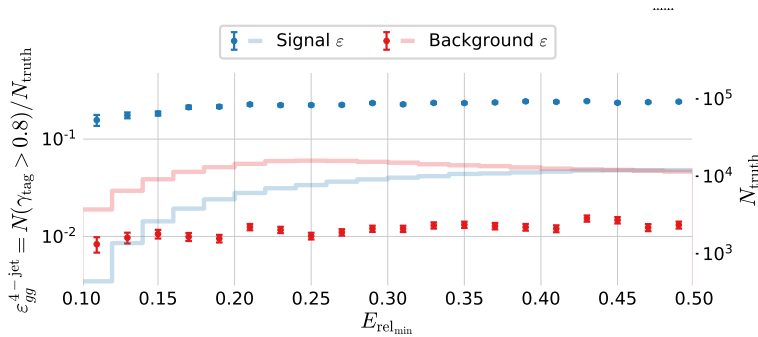
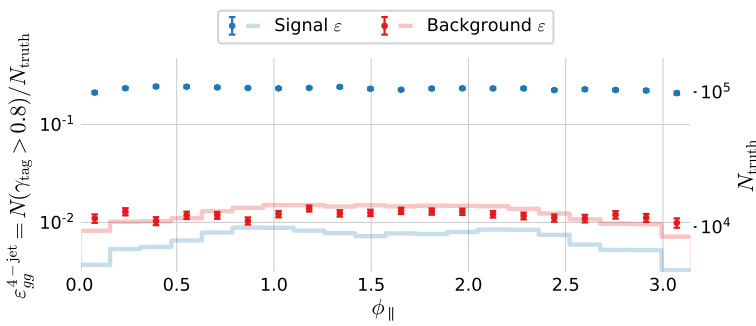
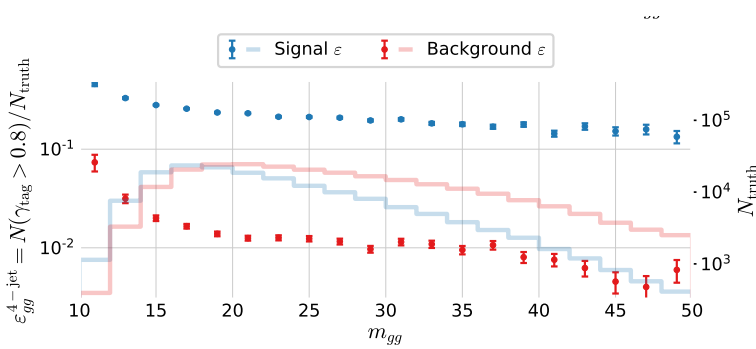
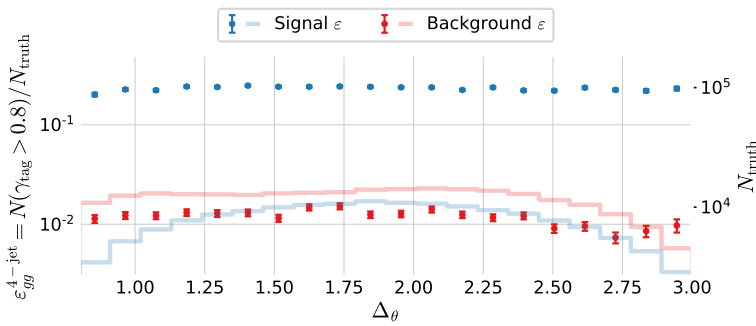
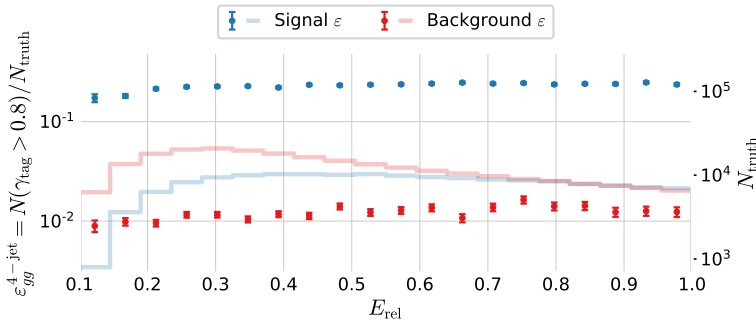


Figure B.41: Efficiency of the  $g$ -tagging algorithm for 4-jet events as a function of  $E_{\text{rel,min}}$  in MC. The efficiency is measured as the number of events with a  $g$ -tag higher than 0.8 ( $\gamma > 0.8$ ) out of the total number. The efficiency is plotted for **signal events** according to MC Truth in blue and **background events** according to MC Truth in red.



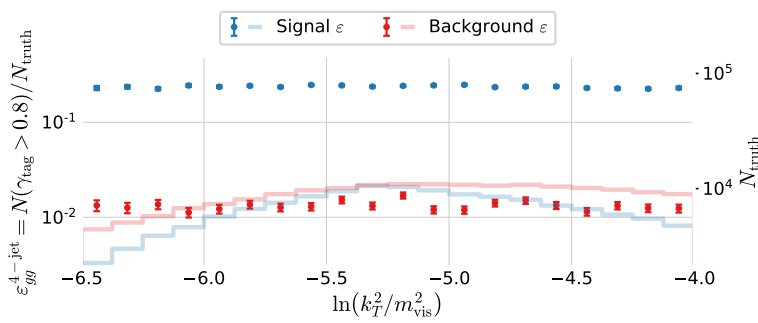


Figure B.46: Efficiency of the  $g$ -tagging algorithm for 4-jet events as a function of  $\ln(k_T^2/m_{\text{vis}}^2)$  in MC. The efficiency is measured as the number of events with a  $g$ -tag higher than 0.8 ( $\gamma > 0.8$ ) out of the total number. The efficiency is plotted for [signal events](#) according to MC Truth in blue and [background events](#) according to MC Truth in red.

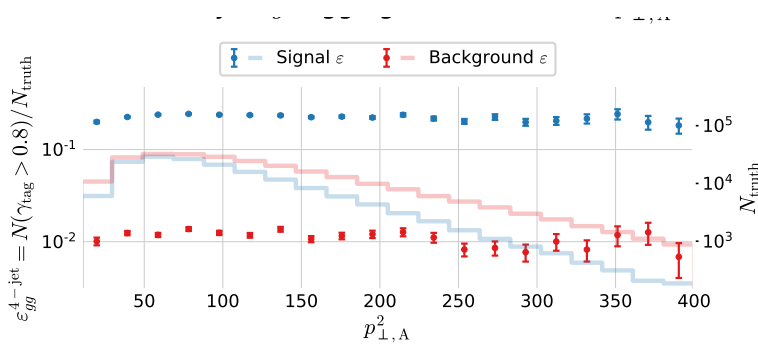


Figure B.47: Efficiency of the  $g$ -tagging algorithm for 4-jet events as a function of  $p_{T,A}^2$  in MC. The efficiency is measured as the number of events with a  $g$ -tag higher than 0.8 ( $\gamma > 0.8$ ) out of the total number. The efficiency is plotted for [signal events](#) according to MC Truth in blue and [background events](#) according to MC Truth in red.

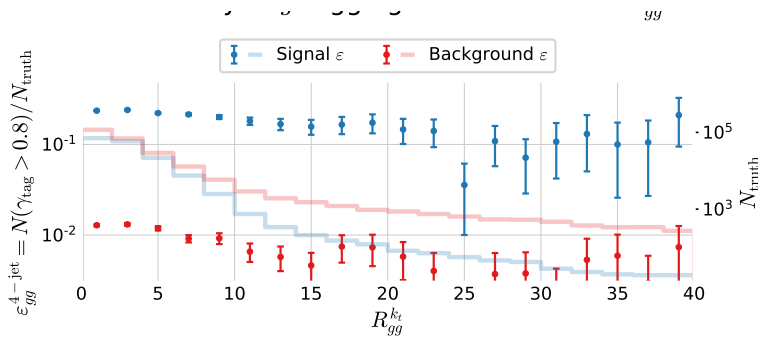


Figure B.48: Efficiency of the  $g$ -tagging algorithm for 4-jet events as a function of  $R_{gg}^{k_t}$  in MC. The efficiency is measured as the number of events with a  $g$ -tag higher than 0.8 ( $\gamma > 0.8$ ) out of the total number. The efficiency is plotted for [signal events](#) according to MC Truth in blue and [background events](#) according to MC Truth in red.

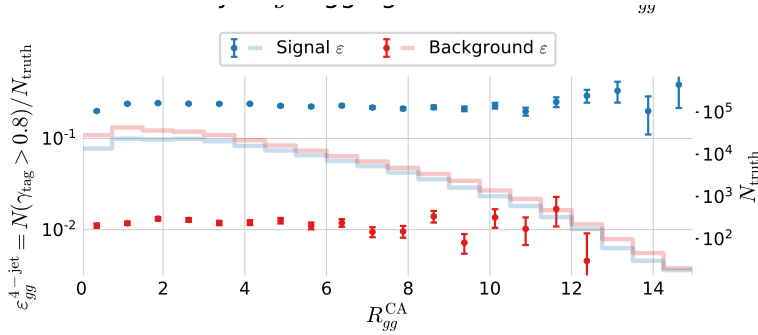
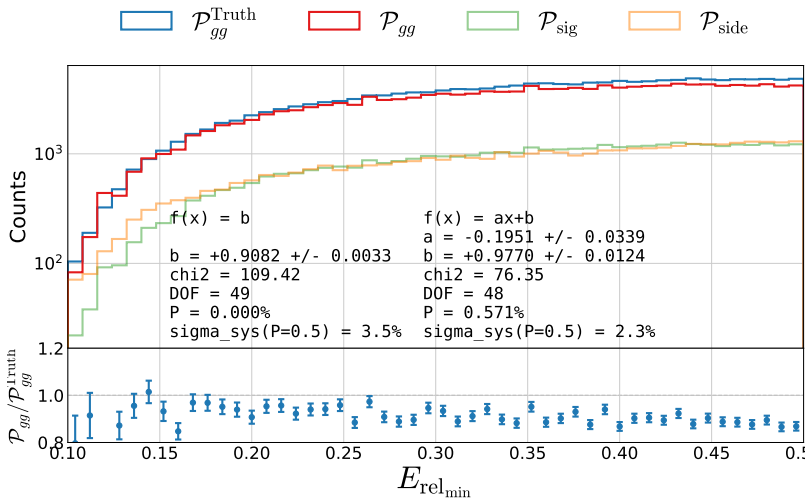
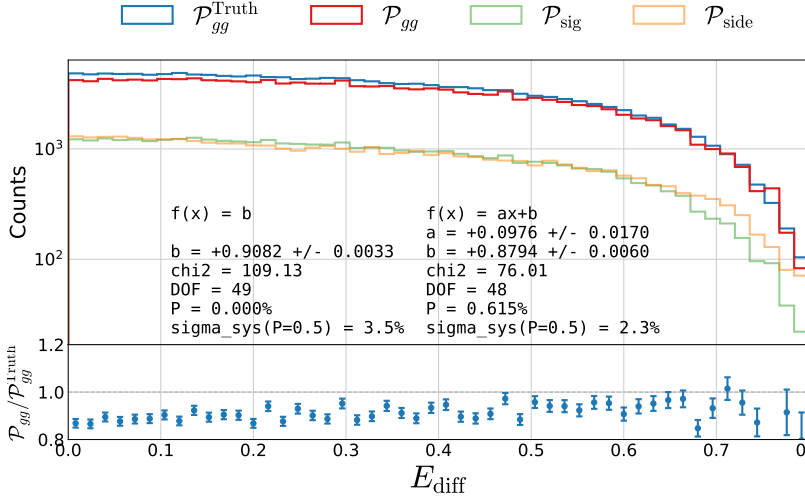


Figure B.49: Efficiency of the  $g$ -tagging algorithm for 4-jet events as a function of  $E$  in MC. The efficiency is measured as the number of events with a  $g$ -tag higher than 0.8 ( $\gamma > 0.8$ ) out of the total number. The efficiency is plotted for [signal events](#) according to MC Truth in blue and [background events](#) according to MC Truth in red.



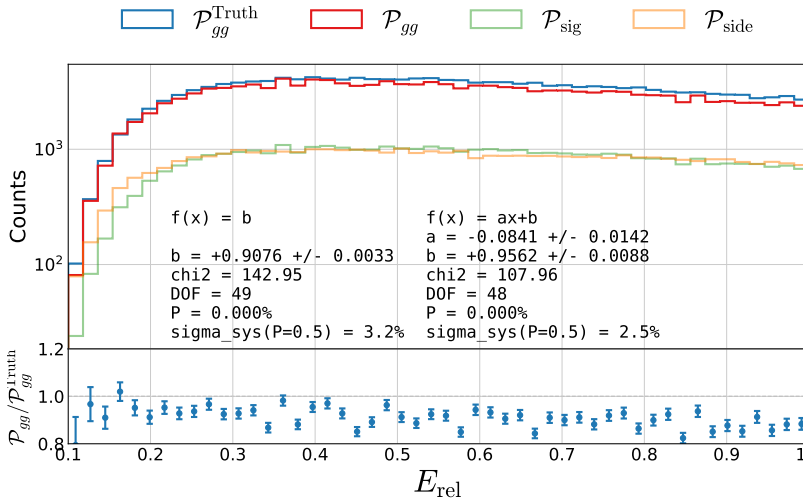


Figure B.52: Closure plot comparing MC Truth and the efficiency corrected  $g$ -tagging model in 4-jet events for  $E_{\text{rel}}$ . In the top part of the plot  $\mathcal{P}_{gg}^{\text{Truth}}$  based on MC Truth is shown in blue, the  $\mathcal{P}_{gg}$  based on MC but without Truth in red, the distribution in the signal region  $\mathcal{P}_{\text{sig}}$  in light green and the distribution in the sideband region  $\mathcal{P}_{\text{side}}$  in light orange. In the bottom part of the plot the ratio between  $\mathcal{P}_{gg}$  and  $\mathcal{P}_{gg}^{\text{Truth}}$  is shown.

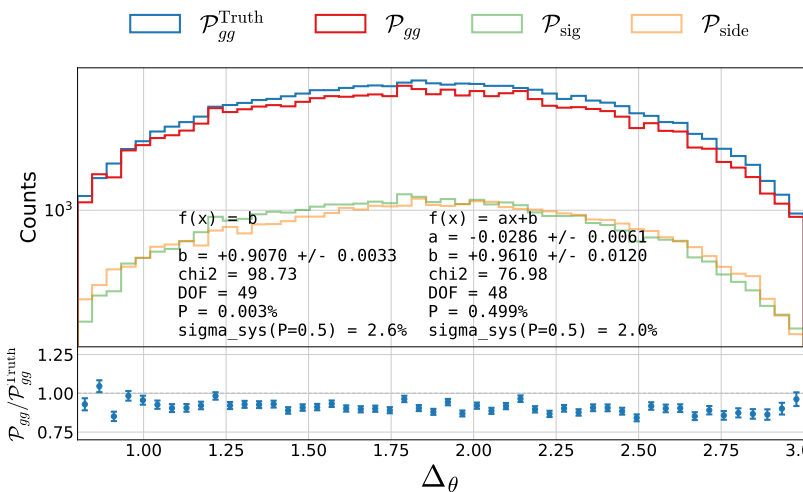


Figure B.53: Closure plot comparing MC Truth and the efficiency corrected  $g$ -tagging model in 4-jet events for  $\Delta_{\theta}$ . In the top part of the plot  $\mathcal{P}_{gg}^{\text{Truth}}$  based on MC Truth is shown in blue, the  $\mathcal{P}_{gg}$  based on MC but without Truth in red, the distribution in the signal region  $\mathcal{P}_{\text{sig}}$  in light green and the distribution in the sideband region  $\mathcal{P}_{\text{side}}$  in light orange. In the bottom part of the plot the ratio between  $\mathcal{P}_{gg}$  and  $\mathcal{P}_{gg}^{\text{Truth}}$  is shown.

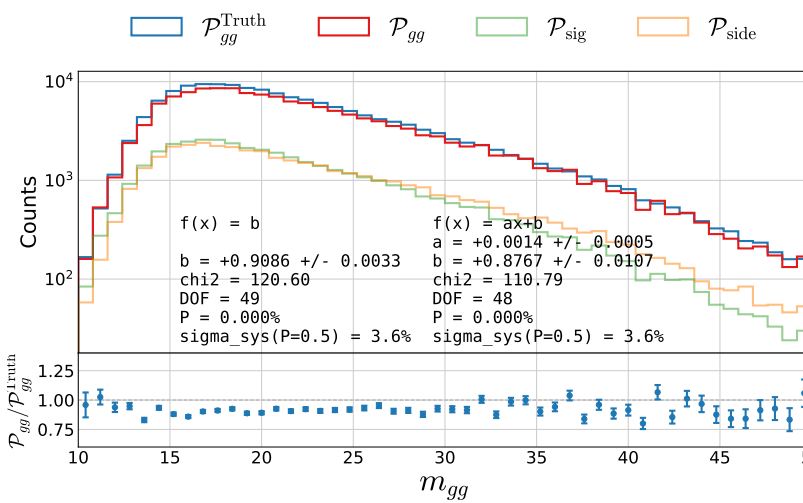


Figure B.54: Closure plot comparing MC Truth and the efficiency corrected  $g$ -tagging model in 4-jet events for  $m_{gg}$ . In the top part of the plot  $\mathcal{P}_{gg}^{\text{Truth}}$  based on MC Truth is shown in blue, the  $\mathcal{P}_{gg}$  based on MC but without Truth in red, the distribution in the signal region  $\mathcal{P}_{\text{sig}}$  in light green and the distribution in the sideband region  $\mathcal{P}_{\text{side}}$  in light orange. In the bottom part of the plot the ratio between  $\mathcal{P}_{gg}$  and  $\mathcal{P}_{gg}^{\text{Truth}}$  is shown.

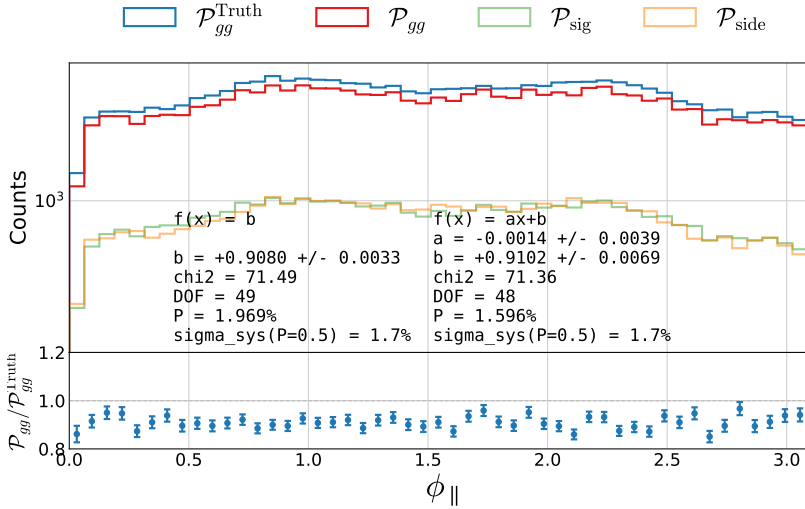


Figure B.55: Closure plot comparing MC Truth and the efficiency corrected  $g$ -tagging model in 4-jet events for  $\phi_{\parallel}$ . In the top part of the plot  $\mathcal{P}_{gg}^{\text{Truth}}$  based on MC Truth is shown in blue, the  $\mathcal{P}_{gg}$  based on MC but without Truth in red, the distribution in the signal region  $\mathcal{P}_{\text{sig}}$  in light green and the distribution in the sideband region  $\mathcal{P}_{\text{side}}$  in light orange. In the bottom part of the plot the ratio between  $\mathcal{P}_{gg}$  and  $\mathcal{P}_{gg}^{\text{Truth}}$  is shown.

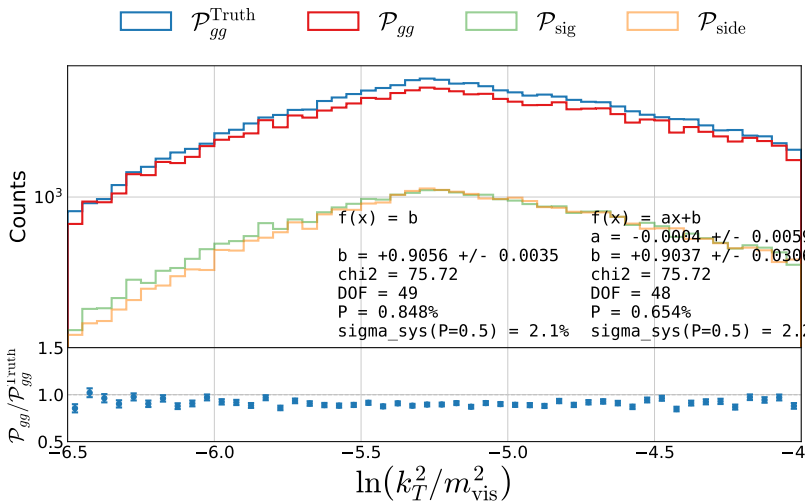


Figure B.56: Closure plot comparing MC Truth and the efficiency corrected  $g$ -tagging model in 4-jet events for  $\ln(k_T^2/m_{\text{vis}}^2)$ . In the top part of the plot  $\mathcal{P}_{gg}^{\text{Truth}}$  based on MC Truth is shown in blue, the  $\mathcal{P}_{gg}$  based on MC but without Truth in red, the distribution in the signal region  $\mathcal{P}_{\text{sig}}$  in light green and the distribution in the sideband region  $\mathcal{P}_{\text{side}}$  in light orange. In the bottom part of the plot the ratio between  $\mathcal{P}_{gg}$  and  $\mathcal{P}_{gg}^{\text{Truth}}$  is shown.

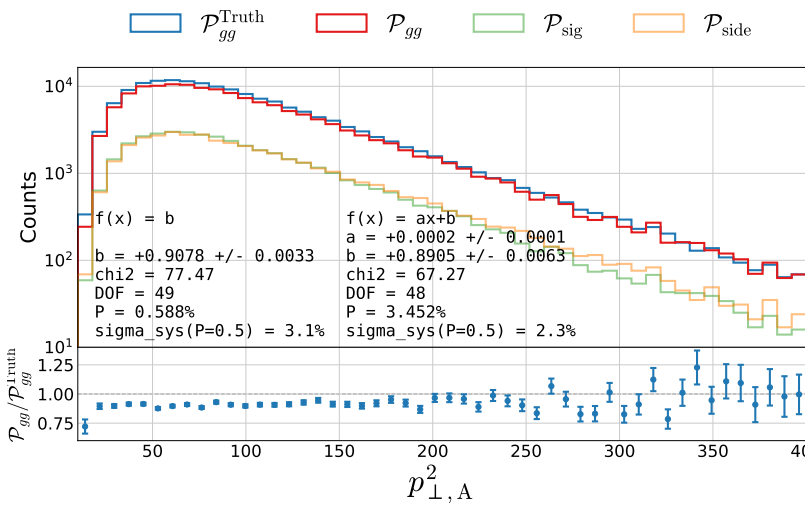


Figure B.57: Closure plot comparing MC Truth and the efficiency corrected  $g$ -tagging model in 4-jet events for  $p_{\perp,A}^2$ . In the top part of the plot  $\mathcal{P}_{gg}^{\text{Truth}}$  based on MC Truth is shown in blue, the  $\mathcal{P}_{gg}$  based on MC but without Truth in red, the distribution in the signal region  $\mathcal{P}_{\text{sig}}$  in light green and the distribution in the sideband region  $\mathcal{P}_{\text{side}}$  in light orange. In the bottom part of the plot the ratio between  $\mathcal{P}_{gg}$  and  $\mathcal{P}_{gg}^{\text{Truth}}$  is shown.

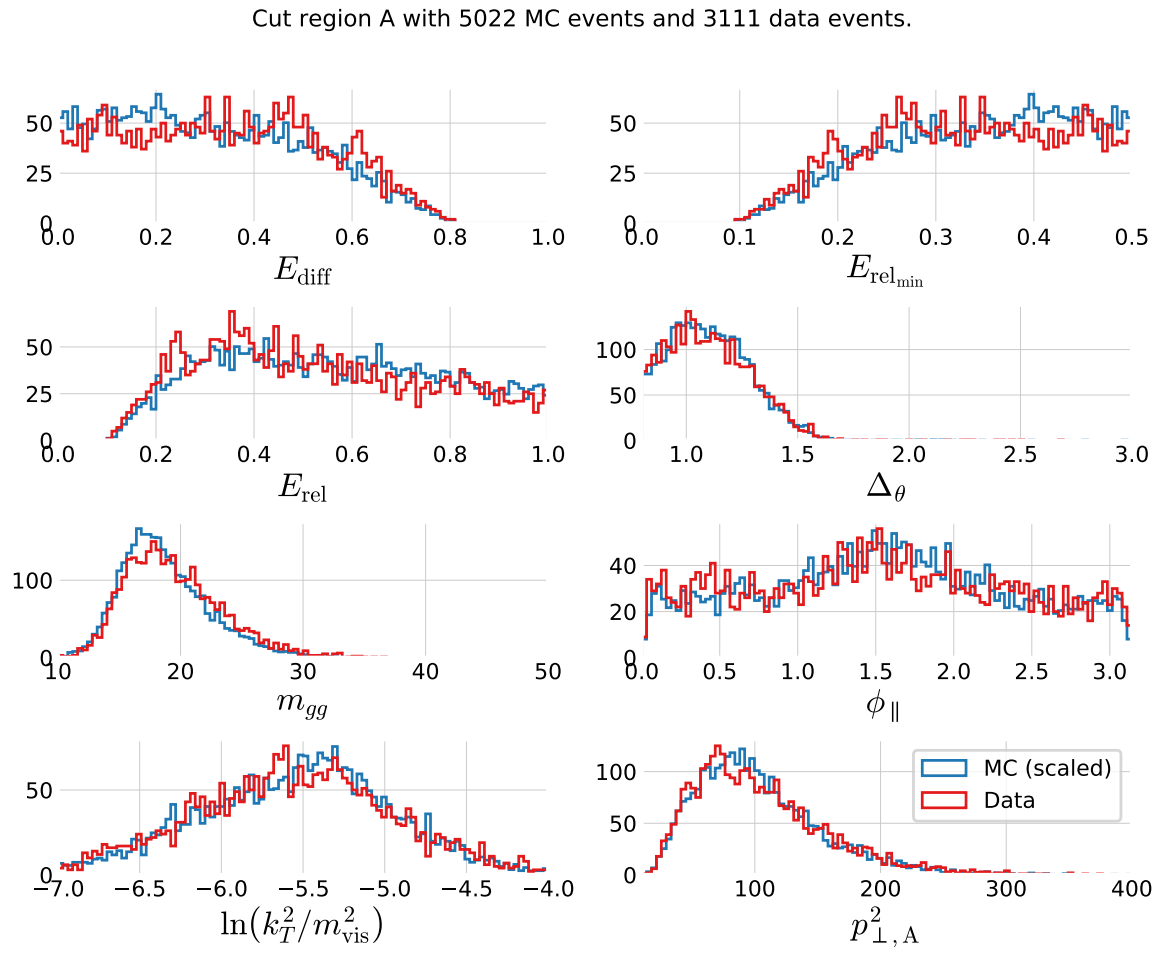


Figure B.58: Comparison of the gluon splitting distributions in MC and Data for  $R_{gg}^{k_t}$ - $R_{gg}^{\text{CA}}$  Phase Space Area A, see Table 5.7. The distribution for MC (scaled to Data) is shown in blue and for Data in red. These eight distributions are for the  $R_{gg}^{k_t}$ - $R_{gg}^{\text{CA}}$  Phase Space Area A which has 5022 events in the MC sample and 3111 in the Data sample.

Cut region B with 7382 MC events and 4035 data events.

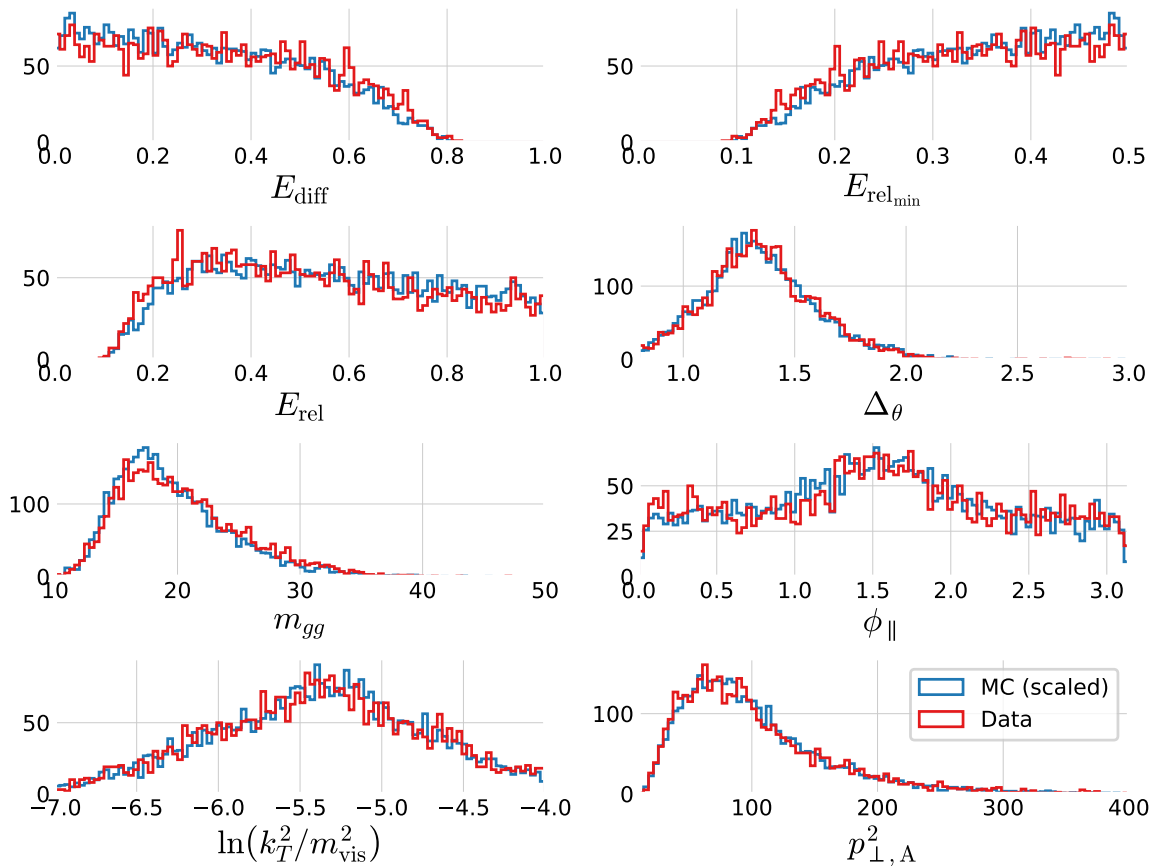


Figure B.59: Comparison of the gluon splitting distributions in MC and Data for  $R_{gg}^k - R_{gg}^{\text{CA}}$  Phase Space Area B, see Table 5.7. The distribution for MC (scaled to Data) is shown in blue and for Data in red. These eight distributions are for the  $R_{gg}^k - R_{gg}^{\text{CA}}$  Phase Space Area B which has 7382 events in the MC sample and 4035 in the Data sample.

Cut region C with 9417 MC events and 5344 data events.

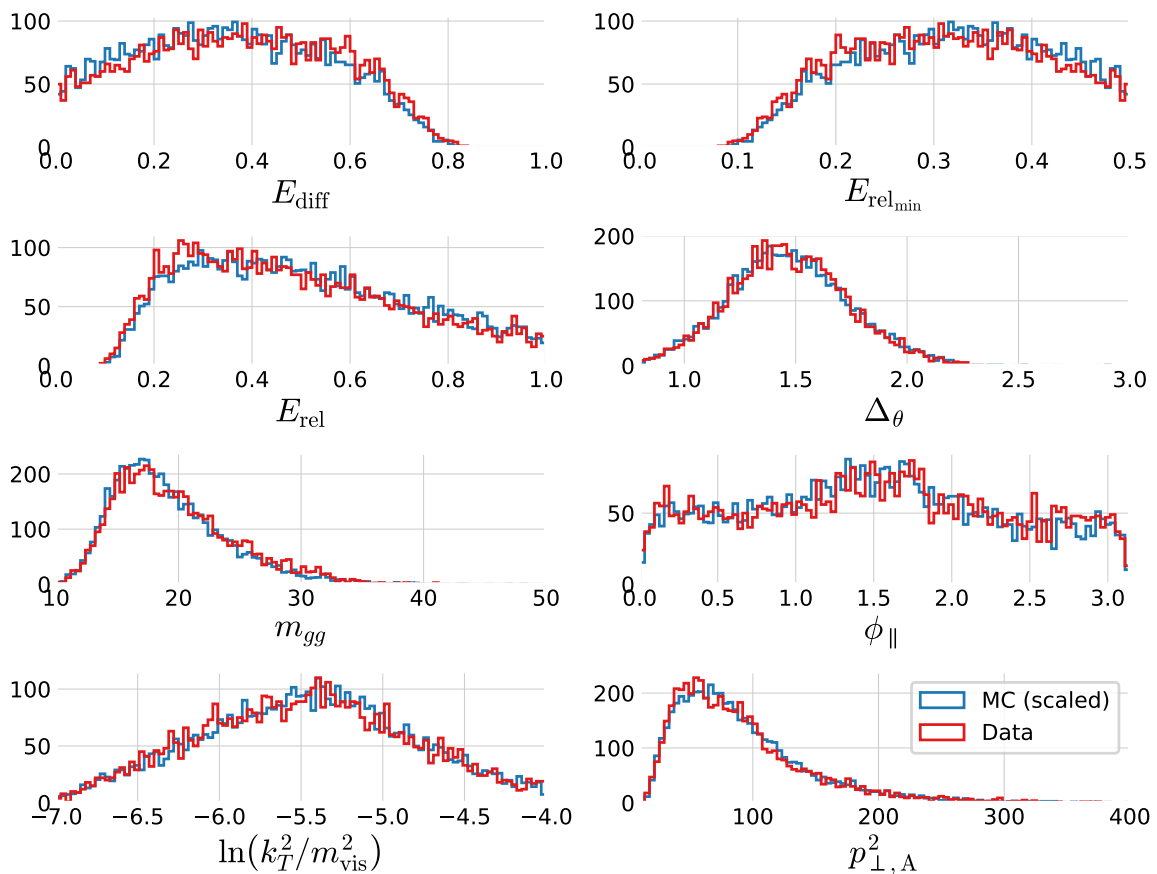


Figure B.6o: Comparison of the gluon splitting distributions in MC and Data for  $R_{gg}^{k_t}$ - $R_{gg}^{\text{CA}}$  Phase Space Area C, see Table 5.7. The distribution for MC (scaled to Data) is shown in blue and for Data in red. These eight distributions are for the  $R_{gg}^{k_t}$ - $R_{gg}^{\text{CA}}$  Phase Space Area C which has 9417 events in the MC sample and 5344 in the Data sample.

Cut region D with 26366 MC events and 13780 data events.

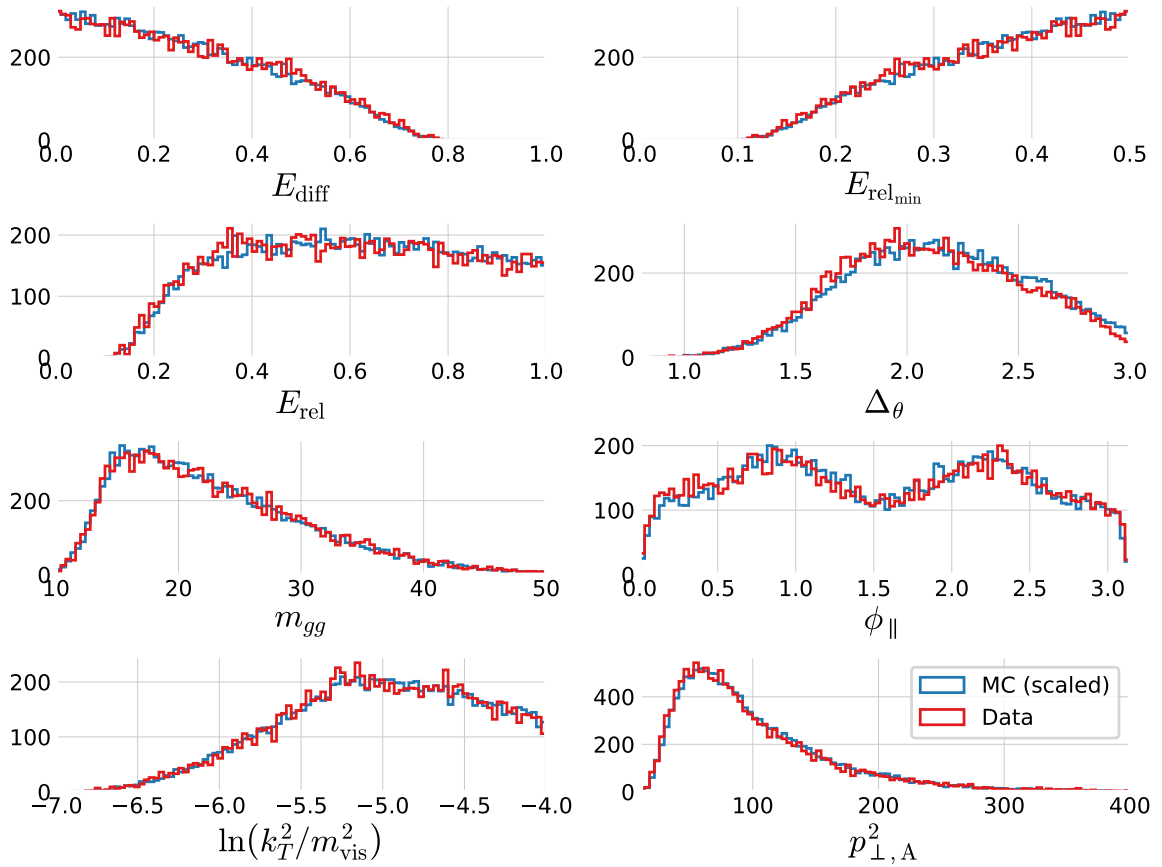


Figure B.61: Comparison of the gluon splitting distributions in MC and Data for  $R_{gg}^{k_t}$ - $R_{gg}^{CA}$  Phase Space Area D, see Table 5.7. The distribution for MC (scaled to Data) is shown in blue and for Data in red. These eight distributions are for the  $R_{gg}^{k_t}$ - $R_{gg}^{CA}$  Phase Space Area D which has 26366 events in the MC sample and 13780 in the Data sample.



# *List of Figures*

2.1	The learning problem.	6
2.2	Approximation-Estimation Tradeoff	10
2.3	Regularization Strength	11
2.4	Regularization Effect of $L_2$	12
2.5	Regularization Effect of $L_1$	12
2.6	$k$ -Fold Cross Validation	13
2.7	$k$ -Fold Cross Validation for Time Series Data	13
2.8	Objective Functions.	15
2.9	Objective Functions Zoom In.	15
2.10	Decision Tree Cuts In Feature Space	16
2.11	Decision Tree	16
2.12	Grid Search	20
2.13	Random Search	20
2.14	Bayesian Optimization	21
3.1	Danish Housing Price Index	27
3.2	Distributions for the housing price dataset	28
3.3	Distributions for the housing price dataset	29
3.4	Histogram of prices of houses and apartments sold in Denmark	30
3.5	Linear correlation between variables and price	31
3.6	Comparison of the Linear Correlation $\rho$ and the Non-Linear MIC.	31
3.7	Non-linear correlation between variables and price	32
3.8	Validity of input features	32
3.9	Validity Dendrogram	33
3.10	Prophet Forecast for apartments	34
3.11	Prophet Trends	35
3.12	XXX	36
3.13	Parallel Coordinate Plot of the Initial Hyperparameter Optimization for Apartments	37
3.14	Initial HPO Results for the Weight Half-life $T_{\frac{1}{2}}$	38
3.15	Initial HPO Results for the Loss Function	38
3.16	XXX	39
3.17	Hyperparameter optimization: random search results	39
3.18	Early Stopping results	40
3.19	Performance of XGB-model on apartment prices	41
3.20	Standard Deviation and MAD of the Static and Dynamic XGB Forecasts	41
3.21	Market Index based on the Static and Dynamic XGB Forecasts	42

3.22 SHAP Prediction Explanation for apartment	44
3.23 Feature importance of apartments prices using XGB	44
3.24 Feature importance of apartments prices using XGB XXX	45
3.25 Performance Comparison of Multiple Models	46
3.26 SHAP plot villa TFIDF XXX	48
4.1 The Standard Model	54
4.2 Feynman diagram for the jet production at LEP	55
4.3 Quark splitting	55
4.4 Hadronization process	56
4.5 The ALEPH detector	57
4.6 Polar angle	57
4.7 Azimuthal angle	57
4.8 Track Significance	59
5.1 Histograms of the vertex variables	65
5.2 UMAP visualization of vertex variables for 4-jet events	66
5.3 UMAP visualization of vertex variables for 3-jet events	66
5.4 UMAP visualization of vertex variables for 2-jet events	66
5.5 Correlation of Vertex Variables	67
5.6 Plot of the log-loss $\ell_{\log}$	68
5.7 Hyperparameter Optimization of $b$ -tagging	69
5.8 Parallel Plot of HPO Results for 4-Jet $b$ -Tagging	69
5.9 $b$ -Tag Scores in 4-Jet Events	70
5.10 ROC curve for 4-jet $b$ -tagging	70
5.11 Distribution of $b$ -Tags in 4-Jet Events	71
5.12 Global Feature Importances for the LGB $b$ -Tagging Algorithm on 4-Jet Events	71
5.13 The expit Function	71
5.14 The logit Function	72
5.15 SHAP 3-Jet Model Explanation for $b$ -like Jet	72
5.16 $b$ -Tagging Efficiency $\varepsilon_b^{b\text{-sig}}$ as a Function of Jet Energy	74
5.17 $b$ -Tagging Efficiency $\varepsilon_g^{g\text{-sig}}$ as a Function of Jet Energy	74
5.18 Hyperparameter Optimization of $g$ -tagging	77
5.19 1D Sum Models Predictions and Signal Fraction for 4-jets events	78
5.20 $g$ -Tag Scores in 4-Jet Events	79
5.21 ROC Curve for $g$ -Tag in 4-Jet Events	80
5.22 Distribution of $g$ -Tag Scores in 4-Jet Events for Signal and Back- ground	80
5.23 Distribution of $b$ -Tag Scores in 3-Jet $l$ -Quark Events for Low and High $g$ -Tag Values	80
5.24 3D Scatter Plot of $\beta_{\text{tag}}$ -Values for High and Low $\gamma_{\text{tag}}$ $l$ -Quark Events	81
5.25 $g$ -Tagging Pseudo Efficiency for $b\bar{b}g$ -Events as a Function of $g$ -Tag	82
5.26 $g$ -Tagging Pseudo Efficiency for $b\bar{b}g$ -Events as a Function of The Mean Invariant Mass	82
5.27 Generalized Angularities	83
5.28 Generalized Angularities for Charged Gluons Jets in 3-Jet Events: $\lambda_0^2$	84

5.29 Soft Wide Angle Gluons in 4-Jet Events	86
5.30 Soft Collinear Gluons in 4-Jet Events	86
5.31 Hard Non $g \rightarrow gg$ Gluons in 4-Jet Events	86
5.32 $g$ -Tagging Efficiency for 4-Jet Events in MC as a Function of the Normalized Gluon-Gluon Jet Energy Difference Asymmetry $E_{\text{diff}}$	87
5.33 Closure Plot Comparing MC Truth and the Efficiency Corrected $g$ -Tagging Model in 4-Jet Events for the Normalized Gluon Gluon Jet Energy Asymmetry	88
5.34 Overview of the Four Areas in the $R_{gg}^{k_t}$ - $R_{gg}^{\text{CA}}$ Phase Space	90
5.35 Gluon Splitting Distribution Comparison in MC and Data for $R_{gg}^{k_t}$ - $R_{gg}^{\text{CA}}$ Phase Space Area A	91
A.1 Validity Heatmap	97
A.2 Distributions for the housing price dataset	98
A.3 Distributions for the housing price dataset	99
A.4 Distributions for the housing price dataset	100
A.5 Distributions for the housing price dataset	101
A.6 Distributions for the housing price dataset	102
A.7 Distributions for the housing price dataset	103
A.8 Distributions for the housing price dataset	104
A.9 Distributions for the housing price dataset	105
A.10 Distributions for the housing price dataset	106
A.11 Distributions for the housing price dataset	107
A.12 Distributions for the housing price dataset	108
A.13 Distributions for the housing price dataset	109
A.14 Distributions for the housing price dataset	110
A.15 Distributions for the housing price dataset	111
A.16 Linear Correlations	113
A.17 MIC non-linear correlation	114
A.18 Prophet Forecast for apartments	115
A.19 Prophet Trends	115
A.20 Overview of initial hyperparameter optimization of the housing model for houses	119
A.21 XXX	120
A.22 XXX	120
A.23 XXX	120
A.24 XXX	121
A.25 XXX	121
A.26 XXX	121
A.27 Performance of XGB-model on apartment prices	122
B.1 UMAP Parameter Grid Search	127
B.2 Visualization of the t-SNE algorithm	127
B.3 Parallel Plot of HPO results for 3-jet $b$ -Tagging	128
B.4 $b$ -tag scores in 3-jet events	128
B.5 ROC curve for 3-jet $b$ -tagging	129
B.6 Distribution of $b$ -Tags in 3-Jet Events	129

B.7 Global Feature Importances for the LGB <i>b</i> -Tagging Algorithm on 3-Jet Events	129
B.8 Parallel Plot of HPO Results for 3-Jet <i>g</i> -Tagging for Energy Ordered Jets	129
B.9 Parallel Plot of HPO Results for 3-Jet <i>g</i> -Tagging for Shuffled Jets	129
B.10 Parallel Plot of HPO Results for 4-Jet <i>g</i> -Tagging for Energy Ordered Jets	130
B.11 Parallel Plot of HPO Results for 4-Jet <i>g</i> -Tagging for Shuffled Jets	130
B.12 PermNet Architecture	130
B.13 1D LGB Model Cuts for 4-jets events	131
B.14 1D Sum Models Predictions and Signal Fraction for 3-jets events	131
B.15 1D LGB Model Cuts for 3-jets events	131
B.16 <i>g</i> -Tag Scores in 3-Jet Events	132
B.17 ROC curve for <i>g</i> -tag in 4-jet events	132
B.18 ROC Curve for <i>g</i> -Tag in 3-Jet Events	132
B.19 Distribution of <i>g</i> -Tag Scores in 3-Jet Events for Signal and Background	133
B.20 <i>b</i> -Tagging Efficiency $\varepsilon_b^{g\text{-sig}}$ as a Function of Jet Energy	133
B.21 <i>b</i> -Tagging Efficiency $\varepsilon_g^{b\text{-sig}}$ as a Function of Jet Energy	133
B.22 Generalized Angularities for Charged Gluons Jets in 3-Jet Events: $\lambda_0^2$	134
B.23 Generalized Angularities for Charged Gluons Jets in 3-Jet Events: $\lambda_{\frac{1}{2}}^1$	134
B.24 Generalized Angularities for Charged Gluons Jets in 3-Jet Events: $\lambda_1^1$	134
B.25 Generalized Angularities for Charged Gluons Jets in 3-Jet Events: $\lambda_1^2$	135
B.26 Generalized Angularities for Charged Gluons Jets in 3-Jet Events: $\lambda_0^0$	135
B.27 Generalized Angularities for Neutral Gluons Jets in 3-Jet Events: $\lambda_0^2$	135
B.28 Generalized Angularities for Neutral Gluons Jets in 3-Jet Events: $\lambda_{\frac{1}{2}}^1$	136
B.29 Generalized Angularities for Neutral Gluons Jets in 3-Jet Events: $\lambda_1^1$	136
B.30 Generalized Angularities for Neutral Gluons Jets in 3-Jet Events: $\lambda_1^2$	136
B.31 Generalized Angularities for Neutral Gluons Jets in 3-Jet Events: $\lambda_0^0$	137
B.32 Relationship Between the <i>g</i> -Tag Value $\gamma_{\text{tag}}$ and the Gluon Splitting Variable $E_{\text{diff}}$	138
B.33 Relationship Between the <i>g</i> -Tag Value $\gamma_{\text{tag}}$ and the Gluon Splitting Variable $E_{\text{rel}_{\min}}$	138
B.34 Relationship Between the <i>g</i> -Tag Value $\gamma_{\text{tag}}$ and the Gluon Splitting Variable $E_{\text{rel}}$	138

- B.35 Relationship Between the  $g$ -Tag Value  $\gamma_{\text{tag}}$  and the Gluon Splitting Variable  $\Delta_\theta$  139  
B.36 Relationship Between the  $g$ -Tag Value  $\gamma_{\text{tag}}$  and the Gluon Splitting Variable  $m_{gg}$  139  
B.37 Relationship Between the  $g$ -Tag Value  $\gamma_{\text{tag}}$  and the Gluon Splitting Variable  $\phi_{\parallel}$  139  
B.38 Relationship Between the  $g$ -Tag Value  $\gamma_{\text{tag}}$  and the Gluon Splitting Variable  $\ln(k_t^2/m_{\text{vis}}^2)$  139  
B.39 Relationship Between the  $g$ -Tag Value  $\gamma_{\text{tag}}$  and the Gluon Splitting Variable  $p_{\perp,A}^2$  140  
B.40  $g$ -Tagging Efficiency for 4-Jet Events in MC as a Function of  $E_{\text{diff}}$  140  
B.41  $g$ -Tagging Efficiency for 4-Jet Events in MC as a Function of  $E_{\text{rel,min}}$  140  
B.42  $g$ -Tagging Efficiency for 4-Jet Events in MC as a Function of  $E_{\text{rel}}$  141  
B.43  $g$ -Tagging Efficiency for 4-Jet Events in MC as a Function of  $\Delta_\theta$  141  
B.44  $g$ -Tagging Efficiency for 4-Jet Events in MC as a Function of  $m_{gg}$  141  
B.45  $g$ -Tagging Efficiency for 4-Jet Events in MC as a Function of  $\phi_{\parallel}$  141  
B.46  $g$ -Tagging Efficiency for 4-Jet Events in MC as a Function of  $\ln(k_t^2/m_{\text{vis}}^2)$  142  
B.47  $g$ -Tagging Efficiency for 4-Jet Events in MC as a Function of  $p_{\perp,A}^2$  142  
B.48  $g$ -Tagging Efficiency for 4-Jet Events in MC as a Function of  $R_{gg}^{k_t}$  142  
B.49  $g$ -Tagging Efficiency for 4-Jet Events in MC as a Function of  $R_{gg}^{\text{CA}}$  142  
B.50 Closure Plot Comparing MC Truth and the Efficiency Corrected  $g$ -Tagging Model in 4-Jet Events for  $E_{\text{diff}}$  143  
B.51 Closure Plot Comparing MC Truth and the Efficiency Corrected  $g$ -Tagging Model in 4-Jet Events for  $E_{\text{rel,min}}$  143  
B.52 Closure Plot Comparing MC Truth and the Efficiency Corrected  $g$ -Tagging Model in 4-Jet Events for  $E_{\text{rel}}$  144  
B.53 Closure Plot Comparing MC Truth and the Efficiency Corrected  $g$ -Tagging Model in 4-Jet Events for  $\Delta_\theta$  144  
B.54 Closure Plot Comparing MC Truth and the Efficiency Corrected  $g$ -Tagging Model in 4-Jet Events for  $m_{gg}$  144  
B.55 Closure Plot Comparing MC Truth and the Efficiency Corrected  $g$ -Tagging Model in 4-Jet Events for  $\phi_{\parallel}$  145  
B.56 Closure Plot Comparing MC Truth and the Efficiency Corrected  $g$ -Tagging Model in 4-Jet Events for  $\ln(k_t^2/m_{\text{vis}}^2)$  145  
B.57 Closure Plot Comparing MC Truth and the Efficiency Corrected  $g$ -Tagging Model in 4-Jet Events for  $p_{\perp,A}^2$  145  
B.58 Gluon Splitting Distribution Comparison in MC and Data for  $R_{gg}^{k_t}$ - $R_{gg}^{\text{CA}}$  Phase Space Area A 146

- B.59 Gluon Splitting Distribution Comparison in MC and Data for  
 $R_{gg}^{k_t}$ - $R_{gg}^{\text{CA}}$  Phase Space Area B 147
- B.60 Gluon Splitting Distribution Comparison in MC and Data for  
 $R_{gg}^{k_t}$ - $R_{gg}^{\text{CA}}$  Phase Space Area C 148
- B.61 Gluon Splitting Distribution Comparison in MC and Data for  
 $R_{gg}^{k_t}$ - $R_{gg}^{\text{CA}}$  Phase Space Area D 149

# List of Tables

3.1	Mapping between the code in <code>SagTypeNr</code> and the type of residence. The two important types of residences are villa (one-family houses) and ejerlejliged (owner-occupied apartments).	29
3.2	Basic Cuts	33
3.3	Side Door Mapping.	33
3.4	Street Mapping	33
3.5	Number of Observations in the Housing Dataset	36
3.6	Number of Observations in the Housing Dataset for the Tight Selection	36
3.7	Results of the initial hyperparameter optimization for apartments for the best loss function $\ell_{\text{Cauchy}}$ .	37
3.8	Results of the initial hyperparameter optimization for houses for the best loss function $\ell_{\text{Cauchy}}$ .	37
3.9	PDFs Used in the Random Search	39
3.10	Realtors' MAD	41
3.11	Performance Metrics for the Housing Model on Apartments	43
3.12	Performance Metrics for the Housing Model on Houses	43
5.1	Dimensions of dataset for Data	64
5.2	Dimensions of dataset for MC and MCb	64
5.3	Number of different types of jets for MC and MCb for $n$ -jet events. See also Table B.1 for relative numbers.	65
5.4	Random Search PDFs for LGB	69
5.5	Global SHAP Feature Importances for the $g$ -Tagging Models in 4-Jet Events	77
5.6	Gluon Splitting Systemic Errors	89
5.7	Area Definition in the $R_{gg}^{k_t} R_{gg}^{\text{CA}}$ Phase Space	89
A.1	XXX <b>TODO!</b>	112
A.2	Energy Rating Mapping	114
A.3	Rmse-ejerlejliged-appendix.	116
A.4	Logcosh-ejerlejliged-appendix.	116
A.5	Cauchy-ejerlejliged-appendix.	116
A.6	Welsch-ejerlejliged-appendix.	117
A.7	Fair-ejerlejliged-appendix.	117
A.8	Rmse-villa-appendix.	117
A.9	Logcosh-villa-appendix.	117
A.10	Cauchy-villa-appendix.	118
A.11	Welsch-villa-appendix.	118

- A.12 Fair-villa appendix. 118
- A.13 XXX ejer tight 123
- A.14 XXX villa tight 123
  
- B.1 Number of different types of jets for MC and MCb written in relative numbers such that each row sum to 100 %. See also Table 5.3. 126
- B.2 Random Search PDFs for XGB 128
- B.3 Global SHAP Feature Importances for the  $g$ -Tagging Models in 3-Jet Events 133

# Bibliography

- [1] Advanced Topics in Machine Learning (ATML). URL <https://kurser.ku.dk/course/ndak15014u>.
- [2] Allstate Claims Severity - Fair Loss. URL <https://kaggle.com/c/allstate-claims-severity>.
- [3] Dmlc/xgboost. URL <https://github.com/dmlc/xgboost>.
- [4] HEP meets ML award | The Higgs Machine Learning Challenge. URL <https://higgsml.lal.in2p3.fr/prizes-and-award/award/>.
- [5] The Large Electron-Positron Collider | CERN. URL <https://home.cern/science/accelerators/large-electron-positron-collider>.
- [6] Microsoft/LightGBM. URL [https://github.com/microsoft/LightGBM/blob/b397555d7023fd05f8e56326905fe7b185109de/src/treelearner/serial\\_tree\\_learner.cpp#L282](https://github.com/microsoft/LightGBM/blob/b397555d7023fd05f8e56326905fe7b185109de/src/treelearner/serial_tree_learner.cpp#L282).
- [7] Scikit-hep/uproot. URL <https://github.com/scikit-hep/uproot>.
- [8] Datashader: Revealing the Structure of Genuinely Big Data. URL <https://github.com/holoviz/datashader>.
- [9] O . Wwww.OIS.dk - Din genvej til ejendomsdata. URL <https://www.ois.dk/>.
- [10] M. Abadi et al. TensorFlow: Large-scale machine learning on heterogeneous systems. URL <http://tensorflow.org/>.
- [11] Y. S. Abu-Mostafa, M. Magdon-Ismail, and H.-T. Lin. *Learning From Data*. AMLBook. ISBN 978-1-60049-006-4.
- [12] D. Albanese, S. Riccadonna, C. Donati, and P. Franceschi. A practical tool for maximal information coefficient analysis. 7. ISSN 2047-217X. doi: 10.1093/gigascience/giy032. URL <https://doi.org/10.1093/gigascience/giy032>.
- [13] H. Albrecht, H. Ehrlichmann, T. Hamacher, R. P. Hofmann, T. Kirchhoff, A. Nau, S. Nowak, H. Schröder, H. D. Schulz, M. Walter, R. Wurth, C. Hast, H. Kolanoski, A. Kosche,

- A. Lange, A. Lindner, R. Mankel, M. Schieber, T. Siegmund, B. Spaan, H. Thurn, D. Töpfer, D. Wegener, M. Bittrner, P. Eckstein, M. Paulini, K. Reim, H. Wegener, R. Eckmann, R. Mundt, T. Oest, R. Reiner, W. Schmidt-Parzefall, W. Funk, J. Stiewe, S. Werner, K. Ehret, W. Hofmann, A. Hüpper, S. Khan, K. T. Knöpfle, M. Seeger, J. Spengler, D. I. Britton, C. E. K. Charlesworth, K. W. Edwards, E. R. F. Hyatt, H. Kapitza, P. Krieger, D. B. MacFarlane, P. M. Patel, J. D. Prentice, P. R. B. Saull, K. Tzamariudaki, R. G. Van de Water, T. S. Yoon, D. Reßing, M. Schmidtler, M. Schneider, K. R. Schubert, K. Strahl, R. Waldi, S. Weseler, G. Kernel, P. Križnič, T. Podobnik, T. Živko, V. Balagura, I. Belyaev, S. Chechelnitsky, M. Danilov, A. Droutskoy, Y. Gershtein, A. Golutvin, G. Kostina, D. Litvintsev, V. Lubimov, P. Pakhlov, F. Ratnikov, S. Semenov, A. Snizhko, V. Soloshenko, I. Tichomirov, and Y. Zaitsev. A model-independent determination of the inclusive semileptonic decay fraction of B mesons. 318(2): 397–404. ISSN 0370-2693. doi: 10.1016/0370-2693(93)90146-9. URL <http://www.sciencedirect.com/science/article/pii/0370269393901469>.
- [14] E. Anderson. The Species Problem in Iris. 23(3):457–509. ISSN 00266493. doi: 10.2307/2394164. URL [www.jstor.org/stable/2394164](http://www.jstor.org/stable/2394164).
  - [15] B. Andersson, G. Gustafson, G. Ingelman, and T. Sjöstrand. Parton fragmentation and string dynamics. 97(2): 31–145. ISSN 0370-1573. doi: 10.1016/0370-1573(83)90080-7. URL <http://www.sciencedirect.com/science/article/pii/0370157383900807>.
  - [16] S. R. Armstrong. A Search for the standard model Higgs boson in four jet final states at center-of-mass energies near 183-GeV with the ALEPH detector at LEP. URL <http://wwwlib.umi.com/dissertations/fullcit?p9910371>.
  - [17] M. Awad and R. Khanna. Support Vector Regression. In M. Awad and R. Khanna, editors, *Efficient Learning Machines: Theories, Concepts, and Applications for Engineers and System Designers*, pages 67–80. Apress. ISBN 978-1-4302-5990-9. doi: 10.1007/978-1-4302-5990-9\_4. URL [https://doi.org/10.1007/978-1-4302-5990-9\\_4](https://doi.org/10.1007/978-1-4302-5990-9_4).
  - [18] R. J. Barlow. *Statistics: A Guide to the Use of Statistical Methods in the Physical Sciences (Manchester Physics Series)*. WileyBlackwell, reprint edition. ISBN 0-471-92295-1. URL <http://www.amazon.co.uk/Statistics-Statistical-Physical-Sciences-Manchester/dp/0471922951%3FSubscriptionId%3D13CT5CVB80YFWJEPWS02%26tag%3Dws%26linkCode%3Dxm%26camp%3D2025%26creative%3D165953%26creativeASIN%3D0471922951>.

- [19] J. T. Barron. A General and Adaptive Robust Loss Function. URL <http://arxiv.org/abs/1701.03077>.
- [20] W. Bartel et al. Experimental study of jets in electron-positron annihilation. 101(1):129–134. ISSN 0370-2693. doi: 10.1016/0370-2693(81)90505-0. URL <http://www.sciencedirect.com/science/article/pii/0370269381905050>.
- [21] E. Becht, C.-A. Dutertre, I. W. H. Kwok, L. G. Ng, F. Ginhoux, and E. W. Newell. Evaluation of UMAP as an alternative to t-SNE for single-cell data. page 298430, . doi: 10.1101/298430. URL <https://www.biorxiv.org/content/10.1101/298430v1>.
- [22] E. Becht, L. McInnes, J. Healy, C.-A. Dutertre, I. W. H. Kwok, L. G. Ng, F. Ginhoux, and E. W. Newell. Dimensionality reduction for visualizing single-cell data using UMAP. 37(1):38–44, . ISSN 1546-1696. doi: 10.1038/nbt.4314. URL <https://www.nature.com/articles/nbt.4314>.
- [23] J. Bergstra and Y. Bengio. Random Search for Hyper-parameter Optimization. 13:281–305. ISSN 1532-4435. URL <http://dl.acm.org/citation.cfm?id=2188385.2188395>.
- [24] C. Bierlich. Rope hadronization, geometry and particle production in pp and pA Collisions. URL <https://lup.lub.lu.se/search/ws/files/18474576/thesis.pdf>.
- [25] Bolighed. Bolighed - usikkerhed i data-vurderingen. URL <https://bolighed.dk/om-bolighed/spoergsmaal-og-svar/#boligvaerdi>.
- [26] L. Breiman. Random Forests. 45(1):5–32. ISSN 1573-0565. doi: 10.1023/A:1010933404324. URL <https://doi.org/10.1023/A:1010933404324>.
- [27] R. P. Brent. *Algorithms for Minimization without Derivatives*. Prentice-Hall Series in Automatic Computation. Prentice-Hall. URL <https://cds.cern.ch/record/113464>.
- [28] E. Brochu, V. M. Cora, and N. de Freitas. A Tutorial on Bayesian Optimization of Expensive Cost Functions, with Application to Active User Modeling and Hierarchical Reinforcement Learning. URL <http://arxiv.org/abs/1012.2599>.
- [29] R. Brun and F. Rademakers. ROOT — An object oriented data analysis framework. 389(1):81–86. ISSN 0168-9002. doi: 10.1016/S0168-9002(97)00048-X. URL <http://www.sciencedirect.com/science/article/pii/S016890029700048X>.
- [30] A. Buckley, J. Butterworth, S. Gieseke, D. Grellscheid, S. Hoche, H. Hoeth, F. Krauss, L. Lonnblad, E. Nurse, P. Richardson, S. Schumann, M. H. Seymour, T. Sjostrand,

- P. Skands, and B. Webber. General-purpose event generators for LHC physics. 504(5):145–233. ISSN 03701573. doi: 10.1016/j.physrep.2011.03.005. URL <http://arxiv.org/abs/1101.2599>.
- [31] C. Burgard. Standard model of physics | TikZ example. URL <http://www.texample.net/tikz/examples/model-physics/>.
  - [32] D. Buskulic et al. An investigation of B<sub>d0</sub> and B<sub>s0</sub> oscillation. 322(4):441–458. ISSN 0370-2693. doi: 10.1016/0370-2693(94)91177-0. URL <http://www.sciencedirect.com/science/article/pii/0370269394911770>.
  - [33] M. Cacciari, G. P. Salam, and G. Soyez. FastJet user manual. 72(3):1896. ISSN 1434-6044, 1434-6052. doi: 10.1140/epjc/s10052-012-1896-2. URL <http://arxiv.org/abs/1111.6097>.
  - [34] S. Catani, Y. L. Dokshitzer, M. H. Seymour, and B. R. Webber. Longitudinally-invariant kt-clustering algorithms for hadron-hadron collisions. 406(1):187–224, . ISSN 0550-3213. doi: 10.1016/0550-3213(93)90166-M. URL <http://www.sciencedirect.com/science/article/pii/055032139390166M>.
  - [35] S. Catani, G. Turnock, and B. R. Webber. Jet broadening measures in e+ e- annihilation. B295:269–276, . doi: 10.1016/0370-2693(92)91565-Q.
  - [36] T. Chen and C. Guestrin. XGBoost: A Scalable Tree Boosting System. pages 785–794. doi: 10.1145/2939672.2939785. URL <http://arxiv.org/abs/1603.02754>.
  - [37] A. Collaboration. Electron efficiency measurements with the ATLAS detector using 2012 LHC proton-proton collision data. 77(3):195, . ISSN 1434-6044, 1434-6052. doi: 10.1140/epjc/s10052-017-4756-2. URL <http://arxiv.org/abs/1612.01456>.
  - [38] C. Collaboration. Search for a Higgs boson in the decay channel H to ZZ(\*) to q qbar l-l+ in pp collisions at sqrt(s) = 7 TeV. 2012(4):36, . ISSN 1029-8479. doi: 10.1007/JHEP04(2012)036. URL <http://arxiv.org/abs/1202.1416>.
  - [39] T. A. Collaboration. Observation of a new particle in the search for the Standard Model Higgs boson with the ATLAS detector at the LHC. 716(1):1–29, . ISSN 03702693. doi: 10.1016/j.physletb.2012.08.020. URL <http://arxiv.org/abs/1207.7214>.
  - [40] T. C. Collaboration. Observation of a new boson at a mass of 125 GeV with the CMS experiment at the LHC. 716(1):30–61, . ISSN 03702693. doi: 10.1016/j.physletb.2012.08.021. URL <http://arxiv.org/abs/1207.7235>.
  - [41] M. Dam. An upper limit for Br(Z->ggg) from symmetric 3-jet zo hadronic decays. 389(2):405–415. ISSN 0370-2693. doi: 10.1016/S0370-2693(96)01450-5.

- [42] A. Diaz-Papkovich, L. Anderson-Trocmé, C. Ben-Eghan, and S. Gravel. UMAP reveals cryptic population structure and phenotype heterogeneity in large genomic cohorts. 15(11). ISSN 1553-7390. doi: 10.1371/journal.pgen.1008432. URL <https://www.ncbi.nlm.nih.gov/pmc/articles/PMC6853336/>.
- [43] Y. L. Dokshitzer, G. D. Leder, S. Moretti, and B. R. Webber. Better Jet Clustering Algorithms. 1997(08):001–001. ISSN 1029-8479. doi: 10.1088/1126-6708/1997/08/001. URL <http://arxiv.org/abs/hep-ph/9707323>.
- [44] S. D. DST. Price Index (EJ14) - Statistics Denmark. URL <https://www.dst.dk/en/Statistik/emner/priser-og-forbrug/ejendomme>.
- [45] S. D. Ellis and D. E. Soper. Successive combination jet algorithm for hadron collisions. 48(7):3160–3166. doi: 10.1103/PhysRevD.48.3160. URL <https://link.aps.org/doi/10.1103/PhysRevD.48.3160>.
- [46] D. et al. Buskulic. A precise measurement of hadrons. 313(3):535–548. ISSN 0370-2693. doi: 10.1016/0370-2693(93)90028-G. URL <http://www.sciencedirect.com/science/article/pii/037026939390028G>.
- [47] F. Faye. Frederik Faye / deepcalo. URL <https://gitlab.com/ffaye/deepcalo>.
- [48] R. A. Fisher. The Use of Multiple Measurements in Taxonomic Problems. 7(2):179–188. ISSN 2050-1439. doi: 10.1111/j.1469-1809.1936.tb02137.x. URL <https://onlinelibrary.wiley.com/doi/abs/10.1111/j.1469-1809.1936.tb02137.x>.
- [49] Y. Freund and R. E. Schapire. A desicion-theoretic generalization of on-line learning and an application to boosting. In P. Vitányi, editor, *Computational Learning Theory*, pages 23–37. Springer Berlin Heidelberg. ISBN 978-3-540-49195-8. Adaboost.
- [50] S. L. Glashow. Partial-symmetries of weak interactions. 22(4):579–588. ISSN 0029-5582. doi: 10.1016/0029-5582(61)90469-2. URL <http://www.sciencedirect.com/science/article/pii/0029558261904692>.
- [51] P. Gras, S. Höche, D. Kar, A. Larkoski, L. Lönnblad, S. Plätzer, A. Siódmok, P. Skands, G. Soyez, and J. Thaler. Systematics of quark/gluon tagging. 2017(7):91. ISSN 1029-8479. doi: 10.1007/JHEP07(2017)091. URL <http://arxiv.org/abs/1704.03878>.
- [52] N. Guttenberg, N. Virgo, O. Witkowski, H. Aoki, and R. Kanai. Permutation-equivariant neural networks applied to dynamics prediction. URL <http://arxiv.org/abs/1612.04530>.

- [53] A. E. Harvey and S. Peters. Estimation Procedures for Structural Time Series Models. doi: [10.1002/for.3980090203](https://doi.org/10.1002/for.3980090203).
- [54] T. Hastie and R. Tibshirani. Generalized Additive Models: Some Applications. 82(398):371–386. ISSN 01621459. doi: [10.2307/2289439](https://doi.org/10.2307/2289439). URL [www.jstor.org/stable/2289439](http://www.jstor.org/stable/2289439).
- [55] T. Hastie, R. Tibshirani, and J. Friedman. *The Elements of Statistical Learning: Data Mining, Inference, and Prediction, Second Edition*. Springer Series in Statistics. Springer-Verlag, 2 edition. ISBN 978-0-387-84857-0. URL [//www.springer.com/la/book/9780387848570](http://www.springer.com/la/book/9780387848570).
- [56] K. Hornik. Approximation capabilities of multilayer feedforward networks. 4(2):251–257. ISSN 0893-6080. doi: [10.1016/0893-6080\(91\)90009-T](https://doi.org/10.1016/0893-6080(91)90009-T). URL <http://www.sciencedirect.com/science/article/pii/089360809190009T>.
- [57] P. Huber and E. Ronchetti. *Robust Statistics*. Wiley Series in Probability and Statistics. Wiley. ISBN 978-1-118-21033-8. URL [https://books.google.dk/books?id=j10hquR\\_j88C](https://books.google.dk/books?id=j10hquR_j88C).
- [58] S. Hviid, Juul. Working Paper: A regional model of the Danish housing market. URL <http://www.nationalbanken.dk/en/publications/Pages/2017/11/Working-Paper-A-regional-model-of-the-Danish-housing-market.aspx>.
- [59] F. James and M. Roos. Minuit – a system for function minimization and analysis of the parameter errors and correlations. 10:343–367. doi: [10.1016/0010-4655\(75\)90039-9](https://doi.org/10.1016/0010-4655(75)90039-9).
- [60] R. E. Kalman. A new approach to linear filtering and prediction problems. 82:35–45.
- [61] G. Ke, Q. Meng, T. Finley, T. Wang, W. Chen, W. Ma, Q. Ye, and T.-Y. Liu. LightGBM: A Highly Efficient Gradient Boosting Decision Tree. In I. Guyon, U. V. Luxburg, S. Bengio, H. Wallach, R. Fergus, S. Vishwanathan, and R. Garnett, editors, *Advances in Neural Information Processing Systems 30*, pages 3146–3154. Curran Associates, Inc. URL <http://papers.nips.cc/paper/6907-lightgbm-a-highly-efficient-gradient-boosting-decision-tree.pdf>.
- [62] D. P. Kingma and J. Ba. Adam: A Method for Stochastic Optimization. URL <http://arxiv.org/abs/1412.6980>.
- [63] G. Klambauer, T. Unterthiner, A. Mayr, and S. Hochreiter. Self-Normalizing Neural Networks. URL <http://arxiv.org/abs/1706.02515>.
- [64] A. J. Larkoski, J. Thaler, and W. J. Waalewijn. Gaining (Mutual) Information about Quark/Gluon Discrimination. 2014 (11). ISSN 1029-8479. doi: [10.1007/JHEP11\(2014\)129](https://doi.org/10.1007/JHEP11(2014)129). URL <http://arxiv.org/abs/1408.3122>.

- [65] C. Leys, C. Ley, O. Klein, P. Bernard, and L. Licata. Detecting outliers: Do not use standard deviation around the mean, use absolute deviation around the median. 49(4):764–766. ISSN 0022-1031. doi: 10.1016/j.jesp.2013.03.013. URL <http://www.sciencedirect.com/science/article/pii/S0022103113000668>.
- [66] S. M. Lundberg and S.-I. Lee. A unified approach to interpreting model predictions. In *Proceedings of the 31st International Conference on Neural Information Processing Systems*, NIPS’17, pages 4768–4777. Curran Associates Inc. ISBN 978-1-5108-6096-4. URL <http://dl.acm.org/citation.cfm?id=3295222.3295230>.
- [67] S. M. Lundberg, G. G. Erion, and S.-I. Lee. Consistent Individualized Feature Attribution for Tree Ensembles - SHAP. . URL <http://arxiv.org/abs/1802.03888>.
- [68] S. M. Lundberg, G. G. Erion, and S.-I. Lee. Consistent Individualized Feature Attribution for Tree Ensembles. . URL <http://arxiv.org/abs/1802.03888>.
- [69] A. L. Maas. Rectifier nonlinearities improve neural network acoustic models.
- [70] L. McInnes and J. Healy. UMAP: Uniform Manifold Approximation and Projection for Dimension Reduction. URL <http://arxiv.org/abs/1802.03426>.
- [71] T. C. Mills. *Time Series Techniques for Economists / Terence c. Mills*. Cambridge University Press Cambridge [England] ; New York. ISBN 0-521-34339-9 0-521-40574-2. URL <http://www.loc.gov/catdir/toc/cam031/89007187.html>.
- [72] I. Mulalic, H. Rasmussen, J. Rouwendal, and H. H. Woltmann. The Financial Crisis and Diverging House Prices: Evidence from the Copenhagen Metropolitan Area. ISSN 1556-5068. doi: 10.2139/ssrn.3041272. URL <https://www.ssrn.com/abstract=3041272>.
- [73] Particle Data Group et al. Review of Particle Physics. 98(3):030001. doi: 10.1103/PhysRevD.98.030001. URL <https://link.aps.org/doi/10.1103/PhysRevD.98.030001>.
- [74] F. Pedregosa, G. Varoquaux, A. Gramfort, V. Michel, B. Thirion, O. Grisel, M. Blondel, P. Prettenhofer, R. Weiss, V. Dubourg, J. Vanderplas, A. Passos, D. Cournapeau, M. Brucher, M. Perrot, and E. Duchesnay. Scikit-learn: Machine learning in Python. 12:2825–2830.
- [75] E. Polley and M. van der Laan. Super Learner In Prediction. URL <https://biostats.bepress.com/ucbbiostat/paper266>.

- [76] J. Proriol, J. Jousset, C. Guicheney, A. Falvard, P. Henrard, D. Pallin, P. Perret, and B. Brandl. TAGGING B QUARK EVENTS IN ALEPH WITH NEURAL NETWORKS (comparison of different methods : Neural Networks and Discriminant Analysis). page 27.
- [77] A. Purcell. Go on a particle quest at the first CERN webfest. URL <https://cds.cern.ch/record/1473657>.
- [78] S. Ravanbakhsh, J. Schneider, and B. Poczos. Deep Learning with Sets and Point Clouds. URL <http://arxiv.org/abs/1611.04500>.
- [79] D. N. Reshef, Y. A. Reshef, H. K. Finucane, S. R. Grossman, G. McVean, P. J. Turnbaugh, E. S. Lander, M. Mitzenmacher, and P. C. Sabeti. Detecting Novel Associations in Large Data Sets. 334(6062):1518–1524. ISSN 0036-8075, 1095-9203. doi: 10.1126/science.1205438. URL <http://science.sciencemag.org/content/334/6062/1518>.
- [80] J. W. Rohlf. *Modern Physics from A to Z*. John Wiley and Sons. ISBN 978-0-471-57270-1.
- [81] P. J. Rousseeuw and C. Croux. Alternatives to the Median Absolute Deviation. 88(424):1273–1283. ISSN 0162-1459. doi: 10.1080/01621459.1993.10476408. URL <https://www.tandfonline.com/doi/abs/10.1080/01621459.1993.10476408>.
- [82] A. Salam. Weak and electromagnetic interactions. In *Selected Papers of Abdus Salam*, volume Volume 5 of *World Scientific Series in 20th Century Physics*, pages 244–254. WORLD SCIENTIFIC. ISBN 978-981-02-1662-7. doi: 10.1142/9789812795915\_0034. URL [https://www.worldscientific.com/doi/abs/10.1142/9789812795915\\_0034](https://www.worldscientific.com/doi/abs/10.1142/9789812795915_0034).
- [83] L. Scodellaro. B tagging in ATLAS and CMS. URL <http://arxiv.org/abs/1709.01290>.
- [84] L. Shapley. A value for n-person games. In *The Shapley Value*, volume 28 of *Annals of Math Studies*, pages 307–317. doi: 10.1017/CBO9780511528446.003.
- [85] T. Sjöstrand, S. Ask, J. R. Christiansen, R. Corke, N. De-sai, P. Ilten, S. Mrenna, S. Prestel, C. O. Rasmussen, and P. Z. Skands. An Introduction to PYTHIA 8.2. 191:159–177. ISSN 00104655. doi: 10.1016/j.cpc.2015.01.024. URL <http://arxiv.org/abs/1410.3012>.
- [86] P. Skands. Peter Skands.
- [87] S. J. Taylor and B. Letham. Forecasting at scale. doi: 10.7287/peerj.preprints.3190v2. URL <https://peerj.com/preprints/3190>.

- [88] i. team. Iminuit – A python interface to minuit. URL <https://github.com/scikit-hep/iminuit>.
- [89] J. Thaler. Report of the Les Houches Quark/Gluon Subgroup. (1):28.
- [90] R. Tibshirani. Regression Shrinkage and Selection via the Lasso. 58(1):267–288. ISSN 0035-9246. URL [www.jstor.org/stable/2346178](http://www.jstor.org/stable/2346178).
- [91] A. Tikhonov. *On the Stability of Inverse Problems*, volume vol. 39 of *Doklady Akademii Nauk SSSR*.
- [92] S. Toghi Eshghi, A. Au-Yeung, C. Takahashi, C. R. Bolen, M. N. Nyachienga, S. P. Lear, C. Green, W. R. Mathews, and W. E. O’Gorman. Quantitative Comparison of Conventional and t-SNE-guided Gating Analyses. 10. ISSN 1664-3224. doi: 10.3389/fimmu.2019.01194. URL <https://www.frontiersin.org/articles/10.3389/fimmu.2019.01194/full>.
- [93] d. L. M. J. van, E. C. Polley, and A. E. Hubbard. Super Learner. 6(1). ISSN 1544-6115. doi: 10.2202/1544-6115.1309. URL <https://www.degruyter.com/view/j/sagmb.2007.6.issue-1/sagmb.2007.6.1.1309/sagmb.2007.6.1.1309.xml>.
- [94] J. J. van der Bij and E. W. N. Glover. Z boson production and decay via gluons. 313(2):237–257. ISSN 0550-3213. doi: 10.1016/0550-3213(89)90317-9. URL <http://www.sciencedirect.com/science/article/pii/0550321389903179>.
- [95] L. van der Maaten and G. Hinton. Visualizing Data using t-SNE. 9:2579–2605. ISSN ISSN 1533-7928. URL <http://www.jmlr.org/papers/v9/vandermaaten08a.html>.
- [96] F. van Veen. The Neural Network Zoo. URL <http://www.asimovinstitute.org/neural-network-zoo/>.
- [97] V. Vapnik. Principles of Risk Minimization for Learning Theory. In *Proceedings of the 4th International Conference on Neural Information Processing Systems*, NIPS’91, pages 831–838. Morgan Kaufmann Publishers Inc. ISBN 978-1-55860-222-9. URL <http://dl.acm.org/citation.cfm?id=2986916.2987018>.
- [98] P. Virtanen, R. Gommers, T. E. Oliphant, M. Haberland, T. Reddy, D. Cournapeau, E. Burovski, P. Peterson, W. Weckesser, J. Bright, S. J. van der Walt, M. Brett, J. Wilson, K. Jarrod Millman, N. Mayorov, A. R. J. Nelson, E. Jones, R. Kern, E. Larson, C. J. Carey, I. Polat, Y. Feng, E. W. Moore, J. VanderPlas, D. Laxalde, J. Perktold, R. Cimrman, I. Henriksen, E. A. Quintero, C. R. Harris, A. M. Archibald, A. H. Ribeiro, F. Pedregosa, P. van Mulbregt, and S. . . Contributors. SciPy 1.0—Fundamental Algorithms for Scientific Computing in Python. page arXiv:1907.10121. URL <https://ui.adsabs.harvard.edu/abs/2019arXiv190710121V/abstract>.

- [99] I. Wallach and R. Lilien. The protein–small-molecule database, a non-redundant structural resource for the analysis of protein-ligand binding. 25(5):615–620. ISSN 1367-4803. doi: 10.1093/bioinformatics/btp035. URL <https://academic.oup.com/bioinformatics/article/25/5/615/183421>.
- [100] S. Weinberg. A Model of Leptons. 19(21):1264–1266. doi: 10.1103/PhysRevLett.19.1264. URL <https://link.aps.org/doi/10.1103/PhysRevLett.19.1264>.
- [101] H. Wickham. Tidy data. 59(10):1–23. ISSN 1548-7660. doi: 10.18637/jss.v059.i10. URL <https://www.jstatsoft.org/v059/i10>.
- [102] M. Wobisch and T. Wengler. Hadronization Corrections to Jet Cross Sections in Deep-Inelastic Scattering. URL <http://arxiv.org/abs/hep-ph/9907280>.
- [103] M. Zaheer, S. Kottur, S. Ravanbakhsh, B. Poczos, R. Salakhutdinov, and A. Smola. Deep Sets. URL <http://arxiv.org/abs/1703.06114>.